A Microcontroller Based Fuzzy Logic Controller Development for the Float Current Analysis of Batteries

TESI DI LAUREA MAGISTRALE IN
ENERGY ENGINEERING-INGEGNERIA ENERGETICA

Author: **Kioomars Afkari**

Student ID:	927152
Advisor:	Prof. Andrea Casalegno
Co-advisor:	Prof. Claudio Rabissi
Supervisors at RWTH Aachen University:	Prof. Dirk Uwe Sauer
	M.Sc. Morian Sonnet
	M.Sc. Gereon Stahl
Academic Year:	2022-23

Acknowledgements

First and foremost, I would like to extend my sincere appreciation to Prof. Dirk Uwe Sauer and M.Sc. Morian Sonnet for granting me this invaluable opportunity to carry out my master thesis under their expert guidance at Institute for Power Electronics and Electrical Drives (ISEA) of RWTH Aachen University. Their unwavering support, invaluable advice, constant guidance, and the chance to gain a holistic and professional understanding of engineering problems at each phase of the project were instrumental in its success.

I would also like to express my gratitude to Prof. Andrea Casalegno and Prof. Claudio Rabissi at Politecnico di Milano for showing a keen interest in my work and supporting me throughout the project. Their guidance has been critical to the completion of my work. I, moreover, wholeheartedly offer my appreciation to M.Sc. Gereon Stahl at ISEA for helping and supporting me in each and every phase of the project, particularly the experimental tests.

I would also like to extend my deep appreciation to my dear family and my dear friends who stood by me during the ups and downs of my academic journey. Their invaluable love, encouragement, patience, and understanding have inspired and motivated me. They made my journey far more meaningful and enjoyable. I will be forever in debt to their love.

Abstract

Lithium-ion battery has gained significant popularity and widespread use in various instruments, devices, and stationary storage systems due to its inherent advantages, including its high volumetric energy density, ease of portability, among others [1]. Lithium-ion batteries represent complex systems, the ageing processes of which are even more complicated. A promising approach to conducting calendaric ageing tests is the float current analysis. This method involves the examination of the steady-state self-discharge current, known as the float current, after a transient phase is accomplished [2]. For fast predicting their lifetime, it is essential to minimize the duration of ageing tests. In order to shorten the test duration, the ISEA institute has already developed measurement electronics that enable the measurement of float current while keeping the voltage constant. The Floater (i.e., the measurements test device) utilized a manually tuned conventional PI controller with a reference point voltage input which should be manually set by the operator prior to the test.

The scope of this project includes the design and implementation of a control algorithm for float current analysis of different Lithium-ion batteries without the need for manual efforts for parameter optimization and tuning. The new algorithm is based on a PI controller integrated with a fuzzy logic interface which tunes the controller gains. In addition, shortening the test time was of great importance; therefore, the manual measurement and setting of the voltage reference point were eliminated as it immensely affected the test duration. Experimental tests were conducted with the new fuzzy logic-based PI controller, and the results were compared with the tests performed using the conventional PI controller with manual tuning in terms of controller performance and test duration. The tests were conducted under the same conditions (temperature, etc.) to have more valid comparisons.

Key-words: lithium-ion battery, calendric ageing, float current, PID controller, fuzzy logic

Abstract in lingua italiana

La batteria agli ioni di litio ha guadagnato una significativa popolarità e diffuso uso in vari strumenti, dispositivi e sistemi di immagazzinamento stazionari, grazie ai suoi vantaggi intrinseci, tra cui l'alta densità energetica volumetrica, la facilità di trasporto, tra gli altri [1]. Le batterie al litio-ion rappresentano sistemi complessi, i cui processi di invecchiamento sono ancora più complicati. Un approccio promettente per condurre test di invecchiamento calendarico è l'analisi della corrente di flottazione. Questo metodo prevede l'esame della corrente di auto-scarica allo stato stazionario, nota come corrente di flottazione, dopo che una fase transitoria è stata completata [2]. Per prevedere velocemente la loro durata, è essenziale minimizzare la durata dei test di invecchiamento. Al fine di accorciare la durata del test, l'istituto ISEA ha già sviluppato elettronica di misura che consentono la misura della corrente di flottazione mantenendo costante la tensione. Il Floater (cioè il dispositivo di test di misura) utilizza un controllore PI convenzionale regolato manualmente con un'ingresso di tensione del punto di riferimento che deve essere impostato manualmente dall'operatore prima del test.

Lo scopo di questo progetto include la progettazione e l'implementazione di un algoritmo di controllo per l'analisi della corrente di flottazione di diverse batterie al litio-ion senza la necessità di sforzi manuali per l'ottimizzazione e l'aggiustamento dei parametri. Il nuovo algoritmo si basa su un controller PI integrato con un'interfaccia di logica fuzzy che accorda i guadagni del controller. Inoltre, la riduzione del tempo di test è stata di grande importanza; pertanto, la misura manuale e l'impostazione del punto di riferimento di tensione sono stati eliminati in quanto influivano enormemente sulla durata del test. Sono stati condotti test sperimentali con il nuovo controller PI basato sulla logica fuzzy, e i risultati sono stati confrontati con i test eseguiti utilizzando il tradizionale controller PI con aggiustamento manuale in termini di prestazioni del controller e durata del test. I test sono stati condotti nelle stesse condizioni (temperatura, ecc.) per avere confronti più validi.

Parole chiave: batteria al litio-ionico, invecchiamento calendrico, corrente fluttuante, controllore PID, logica fuzzy

Contents

1. Introduction

Nowadays, batteries have become an integral part of our daily life, spanning from portable electronics such as smartphones, to electric vehicles. A battery stores energy electrochemically, distinguishing it from alternative energy storage technologies. Notably, batteries exhibit some features such as more modularity, location independence, quick response time, and having no mechanical parts, which make them suitable for a diverse range of applications. In conjunction with other favorable attributes, batteries represent an appealing option for the storage of electrical energy. Alessandro Volta is usually credited as the inventor of the first battery circa 1800. Figure 1-1 and Figure 1-2 show Alessandro Volta and his electric battery prototype, respectively. Subsequently, a variety of battery types with distinctive characteristics have emerged [3]. Among these, the lithium-ion battery is considered to be one of the most promising types in terms of high-energy density, good performance, and no memory effect [4].

Figure 1-1: Alessandro Volta [5]

Figure 1-2: Volta battery, at the Tempio Voltiano museum, Como [6]

Over the lifetime of a battery, its operational capabilities deteriorate. In battery terminology, it undergoes ageing or health deterioration. A comprehensive

understanding of the ageing processes in batteries is essential. Among the principal factors that contribute to battery ageing, storage systems engineers usually measure capacity fade and power fade. Battery ageing is typically classified into two categories, namely calendaric ageing and cyclic ageing [3]. The float current analysis is a convenient technique for executing calendaric ageing tests. The method involves analyzing the float current, which is the self-discharge current in a steady-state after a transient phase has concluded [2]. The principal aim of this investigation is to develop and implement a new control algorithm to measure the float currents of various lithium-ion battery (LIB) types and to shorten the duration of the tests.

1.1   Project Background

The project has been outlined at the ISEA institute of RWTH Aachen University. The ISEA institute consists of three chairs and several departments. The research group chairs are composed of (1) Chair for Power Electronics and Electrical Drives, (2) Chair for Electrochemical Energy Conversion, and (3) Chair for Ageing Processes and Lifetime Prediction of Batteries. The project was conducted under the supervision of Prof. Dirk Uwe Saur, holding the Chair for Electrochemical Energy Conversion [7].

Figure 1-3: ISEA Institute, RWTH Aachen University, Aachen [7]

This project was part of a study focused on investigating the calendaric ageing of lithium-ion batteries utilizing an electronic test device, referred to as the Floater (Figure 1-4). This device is used to measure the float currents of the batteries under

examination. To account for the self-discharge nature of the float current, the test device operates by compensating for the self-discharge through charging of the battery by a controller to maintain the voltage constant. Throughout the test, the data on charging current is logged. The proportional–integral–derivative (PID) type controller used in the study was tuned manually for each battery, and the controller input was an error value, calculated as the difference between a desired setpoint voltage and the measured battery voltage. Additionally, the voltage setpoint was manually adjusted based on the battery voltage measured before the test. The test usually ran for several hours or even up to a couple of days, to balance out the transient phase and record a satisfactory sequence of the data stream on the charging current in the steady-state region.
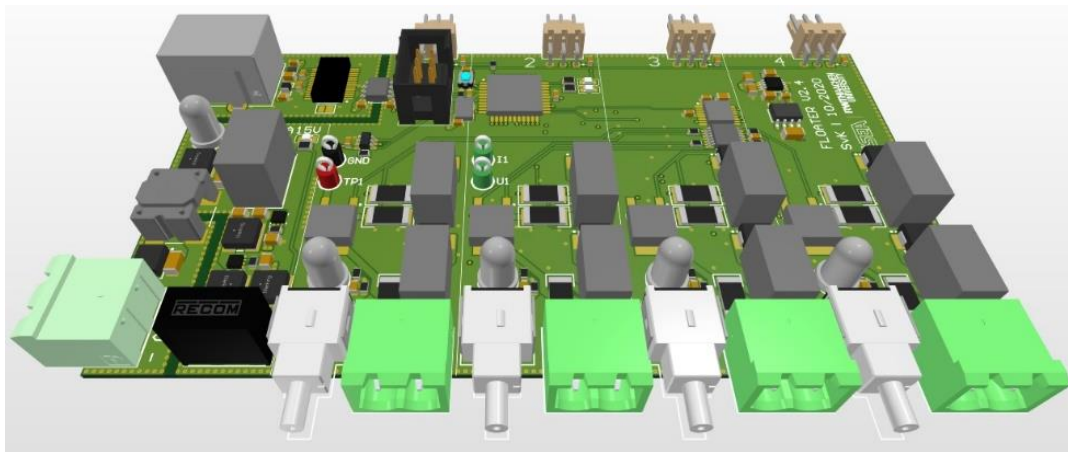

Figure 1-4: 3D model of the Floater test device

1.2   Objectives of the Project

The study had two primary objectives. The first objective was to eliminate the manual efforts required to tune the proportional-integral-derivative (PID) controller gains. This is because engineers had to repeat the tuning process for each battery type tested since the dynamic characteristics of the battery types varied. This procedure was highly time-consuming and labor-intensive. Consequently, the project aimed to design a new controller algorithm that could tune its gains in a manner that corresponds to the battery type being tested. Specifically, an intelligent self-tuning PID controller was intended to replace the previous conventional PID controller.

Minimizing test durations was the second objective of the study. The float current analysis technique may require a considerable amount of time (ranging from several hours to a couple of days) for the self-discharge current to overcome the transient phase and reach a steady-state region. The length of time needed to reach this steady-

state region is dependent on many factors, with the most significant one being the voltage setpoint (and how much the initial battery voltage varies from the manually selected voltage setpoint). Considering the large number of tests that needed to be performed and the time necessary for each test, reducing the duration was of great importance. To address this issue, the new controller algorithm aimed to exclude the manual setpoint designation. Moreover, in some experiments, it may be necessary to specify a particular setpoint voltage. Therefore, this automatic setpoint designation (so-called auto-setpoint feature) was designed to be optional, based on the preference of the operator.

1.3   Phases of the Project

The project planning comprised of several phases to achieve the intended design and outcomes. Figure 1-5 illustrates the main phases of the project. The first phase was focused on developing an intelligent PID controller. Following a series of experimental tests, a self-tuning proportional-integral (PI) controller was deemed more appropriate for the control task. Consequently, the algorithm needed to tune only the proportional and integral terms, while the derivative term could be neglected. The preferred configuration was a combination of a fuzzy logic interface and a PI controller. The fuzzy logic interface utilized the error and its derivative value as inputs. The error was defined as the difference between the setpoint value and the measured voltage of the battery, which corresponds to the conventional PI controller's error definition. The fuzzy logic interface outputs were proportional and integral gain coefficients, which were subsequently fed into the PI controller.

Figure 1-5: Main phases of the project

The next phase of the project was to convert the new algorithm into a code that could be executed on the onboard microcontroller of the test device, i.e., Floater. The programming language used to write the code for the microcontroller was C++. This phase necessitated multiple attempts for debugging and reprogramming to ensure the accurate execution of the algorithm. Additionally, the auto-setpoint feature was integrated into the code. Due to the optionality of this feature, the auto-setpoint was

developed in such a way that if the operator assigns a setpoint value for voltage, the algorithm will adopt it. Alternatively, if the setpoint voltage is equivalent to zero, the auto-setpoint feature will be activated. The final phase of the project involved conducting experimental tests. The experimental tests for each battery were conducted twice under identical ambient conditions and for the same duration. The first set of tests were performed with a traditional PI controller, while the other set was conducted with the new fuzzy logic-based PI controller. This approach was adopted to ensure a more reliable and credible comparison of the results.

1.4   Thesis Outline

The dissertation is structured as follows. After the brief introduction, Chapter 2 describes a summary of the fundamentals and theories in lithium-ion battery technology, ageing processes in batteries, and control systems. In Chapter 3, the methodology of designing the new algorithm, converting the algorithm into the microcontroller code, and conducting the experimental tests are provided. Chapter 4 presents the results of the experimental tests and their comparison with the already in-use conventional controller. Conclusion and future research recommendations are offered in Chapter 5. Figure 1-6 illustrates the thesis outline.
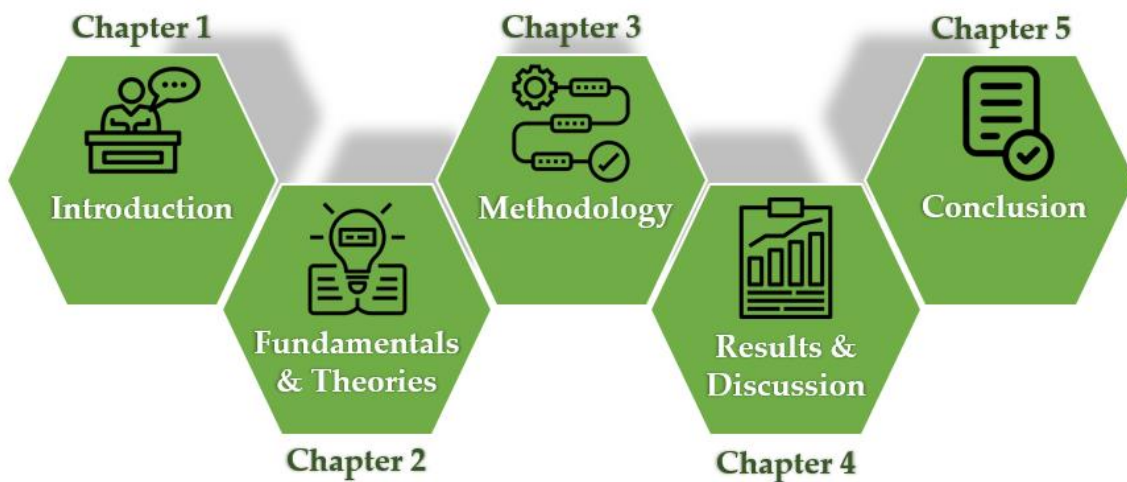

Figure 1-6: Thesis outline

2.   Fundamentals

Climate change along with energy production and storage are one of the most controversial topics in much of the world. With increases in global population and industrialization, electricity production has significantly increased and consequently, reliance on fossil fuels has become more tangible. But this increase in energy demand and production came at a price, increasing emissions of carbon dioxide and other greenhouse gases. As a result, developments and advances are needed in renewable energy technologies and in energy storage technologies, especially those for storing electrical energy to minimize the impact of carbon-based fuels. Renewable energy resources like solar, wind, tidal and geothermal energies are considered auspicious answers to quench the world's thirst for more energy. The renewable energy production facilities are mostly scattered due to the distributed nature of these resources. Moreover, being commonly intermittent sporadic energy resources, advanced energy storage technologies are essential to the storage and transformation of them [8].

There are various means to store energy, such as mechanical, electrical, chemical, and electrochemical energy storage. Pumped hydro-power energy storage (PHES) has dominated the energy storage section for more than a century. More advanced forms namely compressed air energy storage (CAES), flywheel energy storage system (FESS), superconducting magnetic energy storage (SMES), super-capacitors, rechargeable batteries, fuel cells have been developed in the last decades. These technologies could be assessed in terms of energy density, performance, reliability, durability, safety, sustainability etc. Furthermore, their costs in the forms of capital, operating, and maintenance are of much interest [3]. Among these technologies, rechargeable batteries are considered a milestone in the energy storage section as they offer a cost-effective sustainable solution. Over the recent decades, there has been significant advancement in battery technologies, resulting in appreciable usage and huge expansion of application.

As indicated earlier, the subject of this thesis includes improving the controller system of an electronic test device, namely Floater, to conduct the float current

analysis tests as a method of performing calendaric ageing assessment of lithium-ion batteries. The new controller was an intelligent controller integrating a conventional PI controller and a fuzzy logic interface. The development of intelligent controllers has become increasingly relevant in recent years due to their potential to enhance system performance, reduce energy consumption, and increase operational efficiency. The design of an intelligent controller for the Floater device to perform float current analysis tests requires a comprehensive understanding of several fundamental concepts and theories. Specifically, this thesis will introduce and explore the theories and principles of battery technology, battery ageing, PID controllers, and fuzzy logic.

2.1   Overview of Battery Technology

Batteries function as devices that store energy in the form of chemical energy, and upon demand, convert this stored energy into electrical energy. This process takes place via electrochemical reactions that produce a flow of electrons, which commutes between one conductor (i.e., electrode) to another through an external electrical circuit, thereby producing an electric current that can be employed to perform tasks. Simultaneously, charged ions are conveyed through an electrically conducting solution (i.e., electrolyte), which is in contact with the electrodes, to transport reactants towards the interface of the electrode/electrolyte. The electrodes and electrolyte of a battery can be made from a range of materials, and differing compositions of these components can yield a variety of electrochemical reactions and charged ions. Such variances in composition play a pivotal role in determining the energy storage capacity, as well as the operating voltage and overall performance of the battery [8].

The fundamental operational mechanism of an electrochemical battery can be seen in Figure 2-1. A battery cell comprises of two electrodes and at least one electrolyte. During battery discharge, an electrochemical reaction of $R \rightarrow O + n_e e^-$ takes place at the anode/electrolyte interface, resulting in the generation of ions and electrons. While the electrons are conveyed to the cathode through an external electrical circuit connecting the electrodes, the ions migrate to the cathode via the electrolyte. Subsequently, at the cathode/electrolyte interface, the produced electrons and ions engage in a half-reaction (i.e., $O + n_e e^- \rightarrow R$) [8].
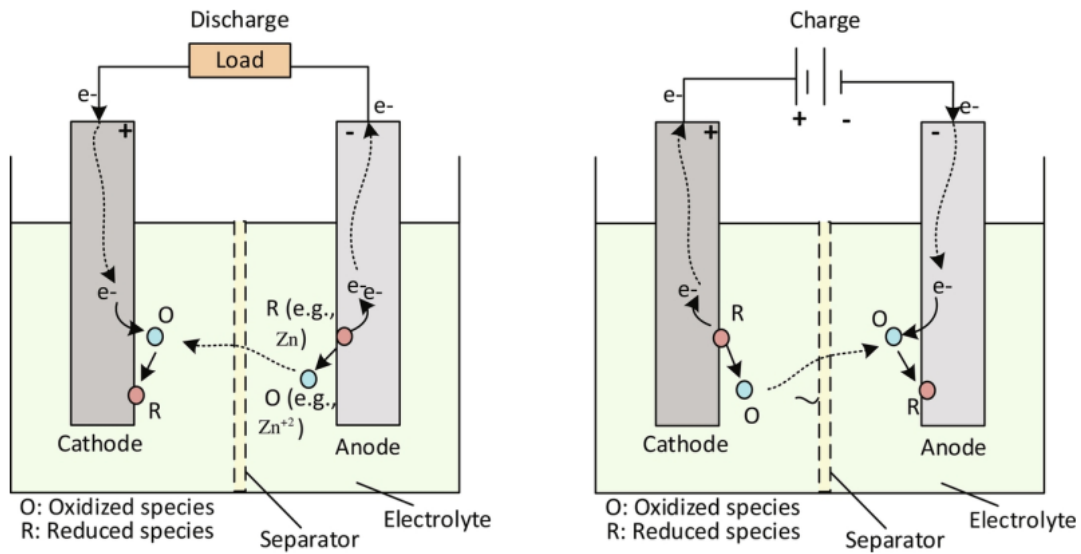
Figure 2-1: Generalized redox operation during discharge / charge in a battery cell [8]

To create an electrochemical cell, two electrodes with different standard reaction potentials can be combined. The electrode with a higher capacity for electron absorption, which occurs at the cathode, exhibits a higher standard potential (in other words, a more positive potential). On the other hand, the electrode with a greater tendency to lose electrons, as occurs at the anode, has a lower standard potential (which means a more negative potential). Therefore, selecting appropriate materials for the anode and cathode involves identifying those with more negative and more positive standard reaction potentials, respectively. Furthermore, materials with lower molecular weights have higher energy densities, and thus are preferable for electrode fabrication. Lithium (Li), magnesium (Mg), and sodium (Na) are the lightest and most easily oxidizable metals, while oxygen (O) and sulfur (S) are the lightest and most easily reducible elements [8].

In order to achieve optimal performance, the cathode of an electrochemical cell should possess desirable characteristics such as high redox potential, which indicates efficient oxidizing ability, high specific capacity that reflects the total amount of electricity generated per gram of cathode material, reversibility, and stability while in contact with the electrolyte. Conversely, the anode should exhibit a low redox potential as an efficient reducing agent, high specific capacity, reversibility, and good conductivity. The cell potential is defined as the potential difference between the cathode and the anode (Equation (2.1)), which determines the voltage level of the cell. The greater the potential difference, the higher the cell potential, and correspondingly, the voltage level [8].

$$E_{cell}^{\circ} = E_{cathode}^{\circ}(\text{reduction potential}) - E_{anode}^{\circ}(\text{oxidation potential}) \tag{2.1}$$

The electrolyte in various types of batteries can exist in many forms, such as liquid, solid, polymer, or composite (hybrid). An ideal electrolyte should possess characteristics being high ionic conductivity, no electrical conductivity, non-reactivity with electrode materials, and a wide range of operating temperatures. The common liquid electrolyte is known for its low viscosity, high energy density, high rate of charge/discharge, relatively low operational temperature, and low flammability. Solid polymeric electrolytes, in particular, have a high degree of flexibility, high energy density, good safety and mechanical properties, and thermal/chemical stability. However, at room temperature, solid polymeric electrolytes often exhibit low ionic conductivities. On the other hand, gel polymeric electrolytes have relatively high ionic conductivities, high flexibility, chemical stability, and multifunctional applications but show poor mechanical strength and interfacial properties. The main advantages of a solid polymeric electrolyte include no electrolyte leakage, nonflammability, nonvolatility, thermal and mechanical stability, ease of fabrication, and high achievable power density and cyclability [8].

The capacity of a battery is defined as the quantity of electric charge that is accumulated during charging, stored during the open circuit period, and subsequently utilized during discharge in a reversible manner. The discharge capacity of a battery can be evaluated by integrating the discharge current from a completely charged state to the voltage threshold, which is commonly referred to as the cutoff voltage (V_{cutoff}), over a corresponding period known as the cutoff time (t_{cutoff}). The discharge capacity (C_d) of the battery can be expressed mathematically as shown in Equation (2.2):

$$C_d = \int_{initial=0}^{t_{cutoff}} I dt = \frac{-n_e F}{M_{electrode}} (m_{electrode}^{initial} - m_{electrode}^{cutoff}) \qquad (2.2)$$

In this equation, $M_{electrode}$ represents the molecular weight of the electrode material (in lithium-ion batteries, that is the molecular weight of Lithium), I refers to the cell current, n_e denotes the number of electrons transferred, and F denotes the Faraday constant. Moreover, the quantities of electrode active materials at the initial (i.e., completely charged battery) and cutoff states are respectively represented by $m_{electrode}^{initial}$ and $m_{electrode}^{cutoff}$ [8].

The category of primary or disposable batteries belongs to batteries in which electron transfer solely occurs from the anode to the cathode during discharge, precluding the possibility of reversible reactions occurring in either electrode. As such, this type of battery is designed to store and deliver energy for a single cycle. The operational lifespan of primary batteries is terminated once the electrodes are depleted, either by releasing all ions into the electrolyte or by attaining full coverage of the electrode

surface with products, thereby hindering any further reactants from reaching the interface and precluding further reaction [8].

Conversely, certain types of batteries allow for the occurrence of reversible reactions within the cell, thereby permitting the possibility of recharging. By appropriate selection of materials for the electrodes, it is feasible for electrons to flow in either direction through external circuits. During charging, the electrochemical reactions that take place at the anode and cathode are the reverse of those that occur during discharge. These secondary batteries are capable of undergoing multiple cycles of charging and discharging before they reach the end of their lifetimes [8].

Various types of batteries exist, each characterized by distinct cell components, such as electrolyte, anode, and cathode. Different types of batteries also exhibit differences in their characteristics, such as operating temperature ranges, fabrication costs, specific energy (i.e., energy content per unit weight of battery), specific power (i.e., loading capability) values, efficiencies, life cycles, and lifetimes. An essential objective in developing battery technology is to enhance these characteristics [8].
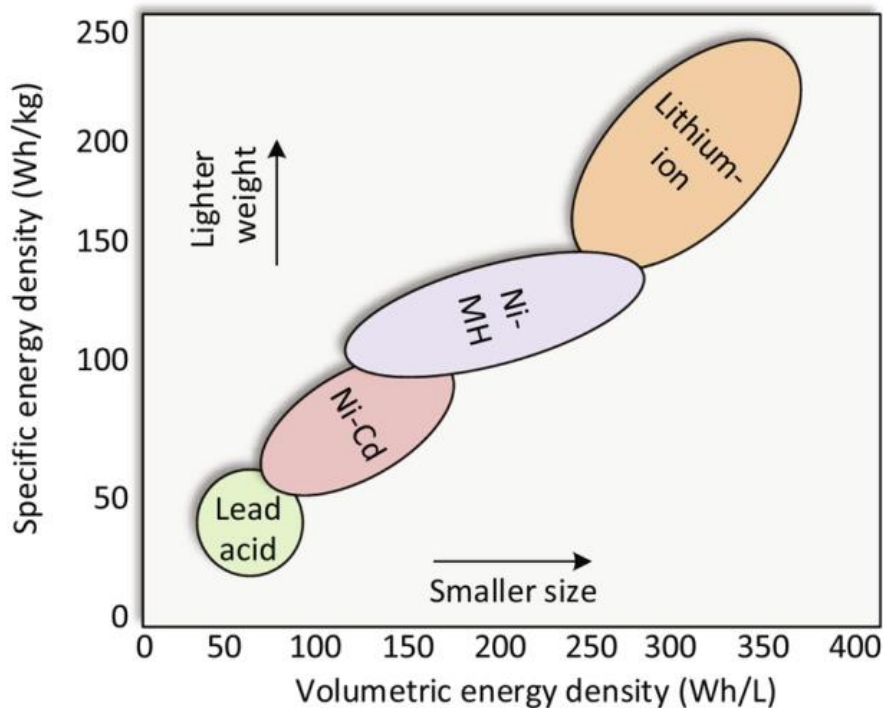
Figure 2-2: Specific energy density and volumetric energy density for lead acid, nickel cadmium, nickel metal hydride, and lithium-ion battery cells [9]

The comparison of specific energy density and volumetric energy density across a range of battery cells is illustrated in Figure 2-2. Notably, lithium-ion batteries exhibit relatively elevated values for both volumetric and specific energy density in contrast

to lead-acid, nickel-cadmium, and nickel-metal hydride batteries, thereby resulting in a smaller sized and decreased weight of lithium-ion batteries for a given capacity. Furthermore, lithium-ion batteries are characterized by advantageous cost profiles, maintenance requirements, and lifetimes [8].

2.2   Lithium-Ion Battery - General Operating Principles

Lithium-ion batteries have some characteristics, such as exceptional specific energy, robustness, and relatively high-power capability, which render them an outstanding choice for a diverse range of portable electronic devices, including but not limited to computers, laptops, cell phones, digital cameras, toys, and power tools. Furthermore, they are widely implemented in the automotive sector, particularly as power packs for electric and hybrid electric vehicles. Owing to their extended lifetimes, high efficiency, and high-power features, lithium-ion batteries are currently employed in stationary power plants and renewable energy-based systems (e.g., solar and wind) as well [8].

In response to the demand for improved battery technologies, the lithium-ion battery (LIB) was developed in Japan by Asahi Kasei Company [10] and subsequently, in 1991, commercialized by Sony Company [11]. A&T Battery Company followed suit by introducing the LIB to the market in 1992. The lithium-ion battery was quickly embraced due to its exceptional performance characteristics, namely its high-energy density, efficient operation, and lack of memory effect observed in conventional nickel-cadmium (Ni-Cd) or nickel-hydride (Ni-MH) batteries. Primarily, LIBs were utilized in portable electronic devices, particularly cellular phones, and notebook computers. However, their application scope shortly expanded to include power tools and battery-assisted electric bicycles. In light of the lithium-ion batteries' impressive attributes, numerous companies began to adapt lithium-ion batteries to hybrid electric vehicles, to substitute the Ni-MH technology [4].

The lithium-ion battery (LIB) boasts a substantially higher energy density when compared to conventional batteries that employ lead and zinc, thanks to lithium's low atomic number and high electrode potential. Nevertheless, the development of novel high-energy lithium-based batteries has proven to be complex and challenging, necessitating the introduction and development of advanced technologies centered around innovative anodes, cathodes, and nonaqueous electrolytes to facilitate the continuous improvement of high-energy lithium battery systems [4].

During the early 1970s, primary batteries featuring a lithium-metal anode and nonaqueous electrolytes like propylene carbonate-lithium perchlorate and lithium negative electrodes were developed. Matsushita introduced a lithium-carbon

monofluoride (Li-CFx) primary cell in 1973, following with Sanyo in 1975 with the commercialization of primary lithium-manganese dioxide primary cells (Li-MnO$_2$), which were employed in applications such as LED fishing floats, cameras, and memory backup devices. Consequently, substantial research was launched to transform lithium primary cells into rechargeable cells featuring high energy density. The various research efforts are documented in Table 2-1 [4].

Lithium-ion battery cells are distinguished by their high energy densities (100–265 Wh/kg on a mass basis and 250–670 Wh/L on a volume basis), prolonged lifecycles, low maintenance costs, and low self-discharge rates (1.5%–2% per month). These batteries are capable of delivering voltages up to 3.6 V, which is three times greater than that of NiMH and Ni-Cd batteries. Despite their numerous advantages, the operation of lithium-ion battery cells at elevated voltages is prone to induce overheating, which in turn may trigger thermal runaway, fire, and combustion. Moreover, the costs associated with lithium-ion battery cells tend to exceed those of other battery types such as Ni-Cd cells [8].

Battery System	Company / Year	Voltage	Wh/kg	Wh/liter
Li/TiS$_2$	Exxon / 1978	2.1	130	280
LiAl/TiS$_2$	Hitachi / 1979	-	-	-
Li/LiAlCl$_4$-SO$_2$/C	Duracell / 1981-85	3.2	63	208
Li/V$_2$O$_5$	Toshiba / 1989	1.5	10	40
Li/NbSe$_3$	Bell Lab / 1983-86	2.0	95	250
LiAl/Polyaniline	Bridgestone / 1987	3.0	-	180
LiAl/Polypyrolle	Kanebo / 1989	3.0	-	180
Li/Al/Polyacene	Kanebo-Seiko / 1991	3.0	-	-
Li/MoS$_2$	MoLi / 1987	1.8	52	140
Li/CDMO(LixMnO$_2$)	Sanyo / 1989	3.0	-	-
Li/Li$_{0.3}$MnO$_2$	Tadiran / 1989	3.0	50	140
Li/VOx	HydroQuebec / 1990	3.2	200	300

Table 2-1: Various developed systems of rechargeable lithium metal batteries [4]

The lithium ion (Li$^+$) travels between the anode and the cathode through an electrolyte and porous separator in the lithium-ion batteries. The working principle of a typical lithium-ion battery is shown in Figure 2-3. Following complete discharge of the lithium-ion battery cell, the Li ions are situated in the cathode. Upon initiating the charging process, these ions de-intercalate from the cathode and traverse the electrolyte towards the anode. As a result, at the culmination of the charging cycle,

the anode becomes the reservoir of lithium atoms, which subsequently migrate back
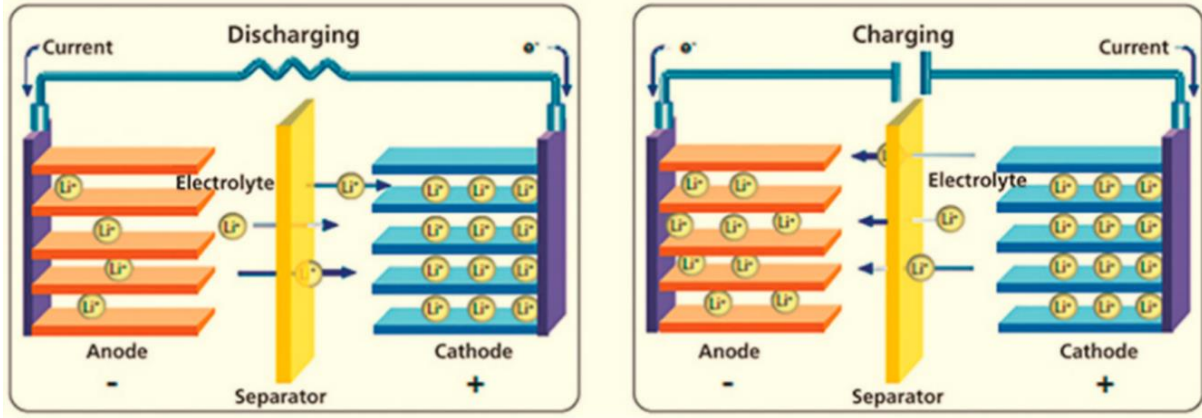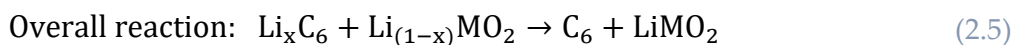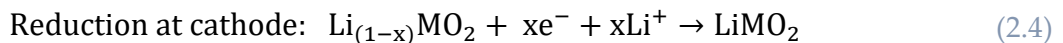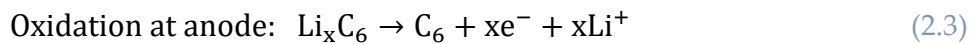to the cathode during the discharge process [8].

Figure 2-3: Movement of Li+ ions balance electrons during charging and discharging
of a Li-ion battery [12]

In lithium-ion battery cells, cathode materials commonly employed include metal
oxides, olivines (e.g., $LiMPO_4$ where metal M = Fe, Mn, Co, Ni), vanadium oxide, and
lithium-manganese spinels (e.g., $LiMn_2O_4$, $LiNi_{0.5}Mn_{1.5}O_4$). Meanwhile, the anode
may consist of porous carbon, lithium titanium oxide, or silicon. The electrolyte
solution typically comprises a mixture of organic solvents containing a dissolved
lithium salt, such as ethylene carbonate ($C_3H_4O_3$), dimethyl carbonate ($C_3H_6O_3$), and
propylene carbonate ($C_4H_6O_3$) [8].

The following equations (Equations (2.3), (2.4), (2.35)) show the general redox
reactions that occur at the anode and cathode during discharging in a lithium-ion
battery employing lithium metal oxide ($Li_{(1-x)}MO_2$) as the cathode and graphite (C_6)
as the anode [8]. A redox reaction is shortened form of "oxidation reduction
reaction". Oxidation is the loss of electrons and reduction is the gain of electrons. In
the redox reaction, both the oxidation and the reduction happen simultaneously
because one reaction is the donor of electrons to the other one [13].

$$\text{Oxidation at anode: } Li_xC_6 \rightarrow C_6 + xe^- + xLi^+ \tag{2.3}$$

$$\text{Reduction at cathode: } Li_{(1-x)}MO_2 + xe^- + xLi^+ \rightarrow LiMO_2 \tag{2.4}$$

$$\text{Overall reaction: } Li_xC_6 + Li_{(1-x)}MO_2 \rightarrow C_6 + LiMO_2 \tag{2.5}$$

During discharging, the lithium undergoes oxidation from Li to Li^+ at the lithium
graphite anode. The produced lithium ions (Li^+) then permeate through the

electrolyte and react with metal oxide at the cathode. The above redox reactions occur in the reverse direction during charging [8].

2.3 Battery Ageing

Battery ageing is a primary constraint associated with battery technologies. This phenomenon is defined as a gradual decline in battery performance over its lifetime, irrespective of usage frequency. Consequently, battery ageing represents a significant disadvantage in practical applications [14]. The ageing process is driven by complex chemical and physical interactions that occur between the electrodes, electrolyte, and separator. Such interactions lead to a decline in power and capacity, known as power and capacity fade, and an increase in internal resistance. The ion exchange process, which is fundamental to battery performance, is hindered by ageing, resulting in decreased battery efficiency [8]. Overall, battery ageing constitutes a crucial factor in determining the optimal lifespan and performance of battery systems.

The decline in battery performance is typically evaluated based on the variations in capacity and the state of health of the battery. However, characterizing the ageing phenomena is a highly intricate task due to the complicated cross-dependence of numerous factors. The ageing process initiates with changes to the chemical composition of the battery's electrolyte. Furthermore, the degradation mechanisms of the positive and negative electrodes exhibit contrasting characteristics. The underlying mechanisms responsible for ageing can be attributed to either chemical or mechanical causes, with the electrodes' composition playing a significant role in determining their prevalence. As a result of ageing, electrode degradation ensues over time, leading to the loss of active material through dissolution into the electrolyte. Thus, the degradation of the electrodes constitutes the primary factor in the ageing of battery systems [8, 14].

2.3.1 Thermal Behavior, SOC, and SOH

The thermal behavior of a battery is reliant on both intrinsic and extrinsic factors, such as intrinsic thermal stability, heterogeneity, and non-uniformity of surface cell temperatures, as well as extrinsic stress factors, including state of charge, current load, and operating temperature. Extrinsic stress factors aggravate degradation processes in battery systems, leading to decreased performance over time. The state of charge (SOC) denotes the ratio of available capacity to the maximum charge storage capacity at a given time. Consequently, a SOC of 100% indicates a fully charged battery, whereas a SOC of 0% represents a fully discharged battery. The SOC can be determined by analyzing the active electrode materials' properties. In a

lithium-ion battery, for instance, a SOC of 100% is achieved when all cyclable lithium ions are transferred to the anode, whereas a SOC of 0% is achieved when all of the ions are transferred back to the cathode. The quality of the electrode structure is a determining factor in the percentage of active materials that can yield cyclable ions [8].

The battery state of health is a metric that compares the current battery capacity to the capacity at the start of its lifespan, thus providing an estimate of its remaining life. For a lithium-ion battery employed in an electric vehicle, the end of life typically corresponds to an 80% nominal capacity at the start of its lifespan. The state of health of a battery is not a physical attribute itself but instead relates to various parameters, including internal resistance, power and capacity fade, and the number of charge-discharge cycles. Capacity fade or loss ensues when a battery's charge storage capacity decreases with repeated use. Similarly, a power fade occurs when the amount of charge delivered at the rated voltage decreases due to increased internal resistance of the battery [8].
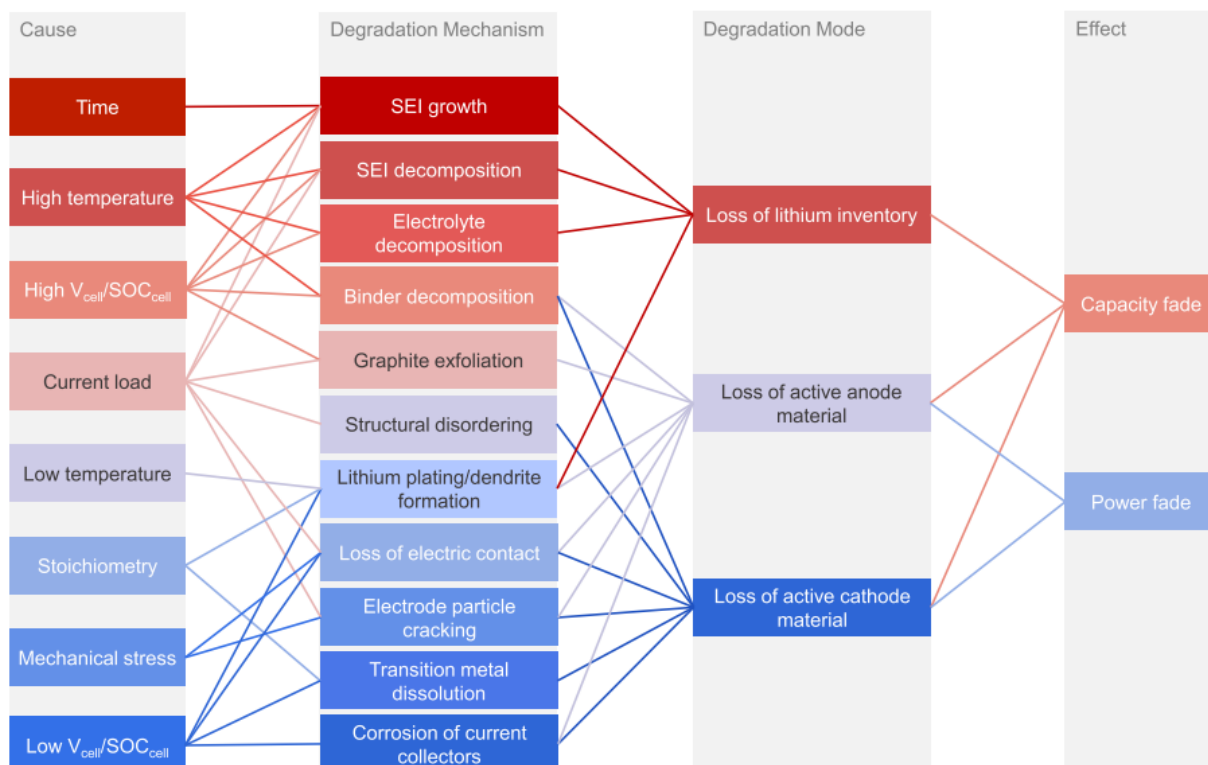

Figure 2-4: Causes and effects of degradation mechanisms and corresponding modes [15]

2.3.2 Lithium-Ion Battery Ageing

The comprehension of lithium-ion batteries is a complex matter, and the processes related to their ageing are even more intricate. The reduction in capacity and power fading do not stem from a single cause but are a result of a variety of processes and their interactions. Additionally, most of these processes are interdependent and occur at similar timescales, making it challenging to investigate ageing mechanisms. Ageing mechanisms that arise in anodes and cathodes differ significantly. The influence of the electrolyte and its ageing (and that of the separator as well) mainly occurs at the electrodes and in conjunction with them [1].

Numerous studies have examined ageing mechanisms in batteries, particularly for lithium-ion cells. For instance, Birkl et al. (2017) [15] investigated the cause and effect of ageing mechanisms in lithium-ion batteries. Figure 2-4 depicts the cause-and-effect analysis of degradation mechanisms in lithium-ion batteries [8].

2.3.3 Consequences of LIB Ageing

The ageing of batteries results in two primary effects, capacity fade and impedance raise, which have distinct origins from chemical causes. The non-linear dependence of these ageing impacts is therefore implied. The degradation of battery performance is caused by various physical-based mechanisms that are dependent on the electrode materials and can be of either mechanical or chemical origin. These mechanisms have several consequences on Lithium-ion cells, including:

- The primary loss of cyclable lithium, which increases the cell imbalance, and is associated with side reactions that can occur at both electrodes, as the SEI grows at the carbon anode due to electrolyte decomposition.
- The secondary loss of electrode active materials, which can be attributed to material dissolution, structural degradation, particle isolation, and electrode delamination.
- The resistance increase of the cell, which results from passive films at the active particle surface and loss of electrical contact within the porous electrode.

In terms of battery performance, both the loss of cyclable and loss of active materials contribute to battery capacity fade. Furthermore, the growth of battery resistance is engendered by the passive films. On vehicle utilization, capacity loss leads to a reduction in autonomy, while the resistance augmentation reduces the maximum power available [14].

2.3.4 Formation of Solid Electrolyte Interface (SEI)

In lithium-ion batteries, the solid electrolyte interface (SEI) can form as a result of the first charging process. During this process, lithium ions are deintercalated from the cathode and migrate to the anode through the electrolyte. The interactions at the electrolyte-electrode interfaces create boundary phases of the SEI, enabling a reversible cycling of the battery. These interfaces are more prominent at the anode side, as illustrated in Figure 2-5 [8].

The SEI is primarily composed of insoluble decomposition products of electrolyte and lithium ions from the cathode, with its composition varying depending on temperature. The SEI acts as a passivation layer on the anode surface, which inhibits further electrolyte decomposition. As the SEI thickness increases, so does the internal resistance during lithium-ion intercalation and de-intercalation, thereby affecting battery performance at different operating temperatures. Therefore, the utilization of battery thermal management systems is crucial in maintaining an appropriate battery temperature range, which is necessary to ensure SEI stability and passivation effectiveness [8].
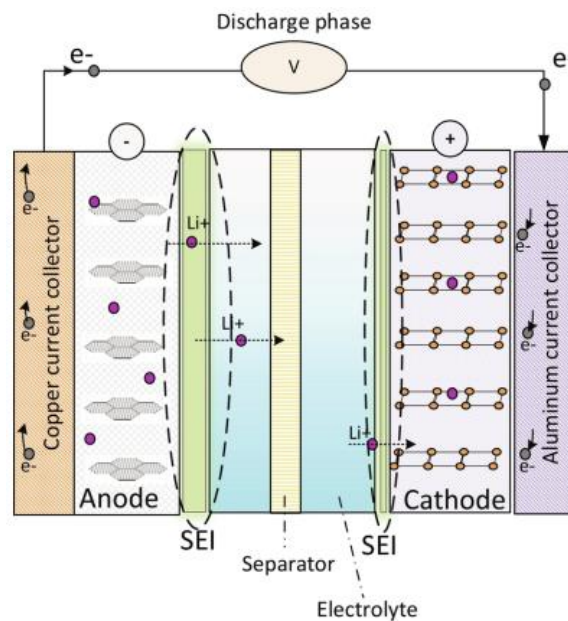

Figure 2-5: Passage of Li$^+$ from the solid electrolyte interface in a LIB [8]

2.3.5 Anode Ageing

The ageing mechanisms in the anode and cathode of lithium-ion batteries exhibit significant differences. Electrolyte influence and ageing occur mainly at the electrodes, in interaction with them, and in the electrolyte and separator [1]. Although research has recently focused on alternative anode materials such as

titanate, silicon, or lithium storage metals and alloys, most negative electrodes still comprise graphite [14]. Consequently, the most extensive understanding of anode ageing is for graphite-based cells [1]. The anode ageing in lithium-ion batteries is caused by degradations resulting from temperature, state of charge (SOC), and overcharge stress factors.

As is well established, the anodes in lithium-ion batteries operate at voltages that exceed the electrochemical stability window of the electrolyte constituents. Therefore, when the electrode is in the charged state (polarized to low potentials), reductive electrolyte decomposition and irreversible consumption of lithium ions occur at the electrode/electrolyte interface. This decomposition results in the development of "protective layers" on the electrode surface, known as the solid electrolyte interface (SEI) [1]. The primary ageing factor for graphite electrodes is the formation and evolution of the SEI over time [14]. At elevated temperatures (above 50°C) and high SOC values (above 80%), the SEI gradually dissolves, and less permeable species such as lithium salts are generated from it [8].

Figure 2-6 illustrates the changes that occur over time at the SEI due to the reactions between the anode and the electrolyte, which are regarded as the major source of ageing in the anode by many researchers [1]. These lithium salts hinder the movement of lithium ions and, consequently, increase the resistance in the anode. Additionally, the diffusion of lithium into the SEI and anode diminishes at relatively low temperatures (below 20°C), resulting in the deposition of lithium on the anode in the form of dendrites. This process, known as lithium plating, is more detrimental to the ageing mechanism in the battery than high-temperature operation [8].
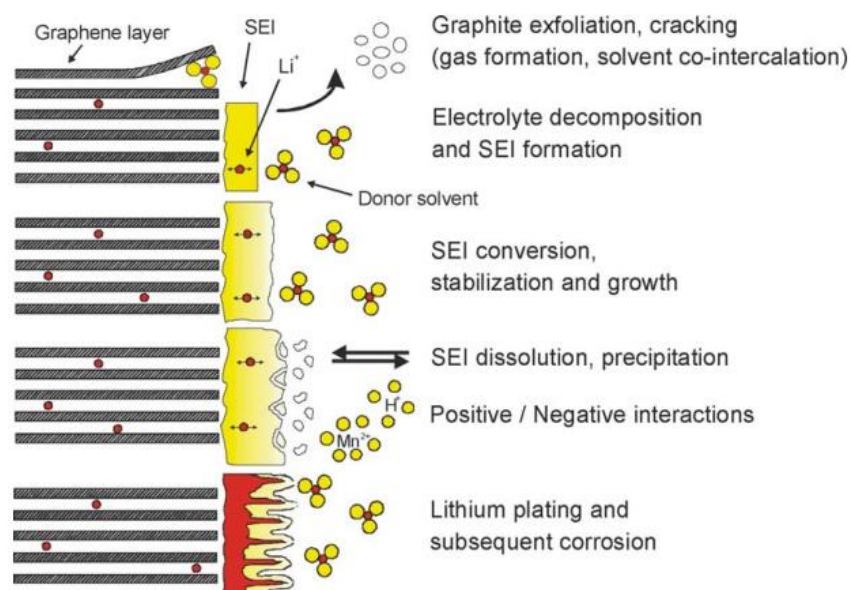

Figure 2-6: Changes at the anode-electrolyte interface [1]

Cause	Effect	Leads to	Reduced by	Enhanced By
Electrolyte Decomposition (continuous side reaction at low rate)	Loss of lithium Impedance rise	Capacity fade Power fade	Stable SEI (additives) Rate decreases with time	High temperatures High SOC (low potential)
Solvent co-intercalation, gas evolution and subsequent cracking formation in particles	Loss of active material (graphite exfoliation) Loss of lithium	Capacity fade	Stable SEI (additives) Carbon pre-treatment	Overcharge
Decrease of accessible surface area due to continuous SEI growth	Impedance rise	Power fade	Stable SEI (additives)	High temperatures High SOC (low potential)
Changes in porosity due to volume changes, SEI formation and growth	Impedance rise Overpotentials	Power fade	External pressure Stable SEI (additives)	High cycling rate High SOC (low potential)
Contact loss of active material particles due to volume changes during cycling	Loss of active material	Capacity fade	External pressure	High cycling rate High DOD
Decomposition of binder	Loss of lithium Loss of mechanical stability	Capacity fade	Proper binder choice	High SOC (low potential) High temperatures
Current collector corrosion	Overpotentials Impedance rise Inhomogeneous distribution of current and potential	Power fade Enhances other ageing mechanisms	Current collector pre-treatment	Overdischarge Low SOC (high potential)
Metallic lithium plating and subsequent electrolyte decomposition by metallic Li	Loss of lithium (Loss of electrolyte)	Capacity fade (Power fade)	Narrow potential window	Low temperatures High cycling rates Poor cell balance Geometric misfits

Table 2-2: Lithium-ion anode ageing (causes, effects, and influences) [1]

The formation of a solid electrolyte interface (SEI) on the anode of lithium-ion batteries typically results in the release of gaseous electrolyte decomposition products. The degree of irreversible charge capacity consumption during SEI formation is influenced by the specific surface area of the graphite and layer formation conditions. On a long-term basis, the SEI infiltrates into the electrode's pores, as well as those of the separator, resulting in a decrease in the electrode's active surface area. This reduction leads to an increase in electrode impedance, which directly correlates with the cell's power loss. The electrode impedance increase is thought to be caused by the SEI's growth and modifications in composition and morphology. In summary, while SEI formation at the anode occurs primarily during the first few charge/discharge cycles, SEI conversion, stabilization, and growth also occurs during subsequent cycling and storage. Table 2-2 presents an overview of the causes and effects of anode ageing [1].

In conclusion, the primary ageing mechanisms of carbon-based anodes can be concisely characterized as follows: The formation and growth of the solid electrolyte interface (SEI) lead to an increase in impedance at the anode, which is directly related to power fade. Typically, SEI formation predominantly occurs at the beginning of cycling, whereas SEI growth is favored by elevated temperatures and proceeds during cycling and storage. In parallel to SEI growth, lithium corrosion within the active carbon results in self-discharge and capacity fade, as mobile lithium is lost. Additionally, the gradual contact loss within the composite anode due to SEI formation and growth contributes to increased impedance in the cell. Lithium metal plating may occur at low temperatures, high rates, and for inhomogeneous current and potential distributions, resulting in accelerated ageing due to the reaction of Li metal with the electrolyte. Notably, the specific components of the cell exert a significant influence on the ageing mechanism, and while the general mechanisms hold true for most lithium-ion systems, they may be expressed differently in each particular system [1].

2.3.6 Cathode Ageing

The cathode undergoes ageing primarily as a result of temperature and state of charge (SOC) effects. Although the solid-electrolyte interphase (SEI) is also formed at the cathode, it is typically thinner than at the anode, resulting in a less pronounced effect of SEI thickness and passivation ability at the cathode [8]. Cathode materials play a crucial role in determining the performance metrics and both cycling and calendar life of lithium-ion cells. The development of novel cathode materials can potentially enhance the performance and energy density capabilities of batteries. Several changes to the cathode can influence the lifetime of a lithium-ion cell [1]:

- ageing of active material.
- degradation or changes of electrode components like conducting agents, binder, corrosion of current collector,
- oxidation of electrolyte components and surface film formation,
- interaction of ageing products with the negative electrode.

These phenomena are interrelated and cannot be examined in isolation. They are highly dependent on the composition of each electrode and are affected by cycling and storage conditions. In general, the decline in charge capacity of the positive active material can be attributed to three fundamental factors:

- structural changes during cycling,
- chemical decomposition/dissolution reaction,
- surface film modification.

As with negative carbon materials, the degradation of positive active materials is influenced by cycling conditions and state of charge. Figure 2-7 and Figure 2-8 provide an illustration of basic ageing mechanisms of cathode materials and a schematic overview of the ageing mechanisms for lithium-ion cathode materials, respectively. It is important to note that these mechanisms are interdependent and highly sensitive to variations in the composition of individual electrodes, as well as to cycling and storage conditions [1].
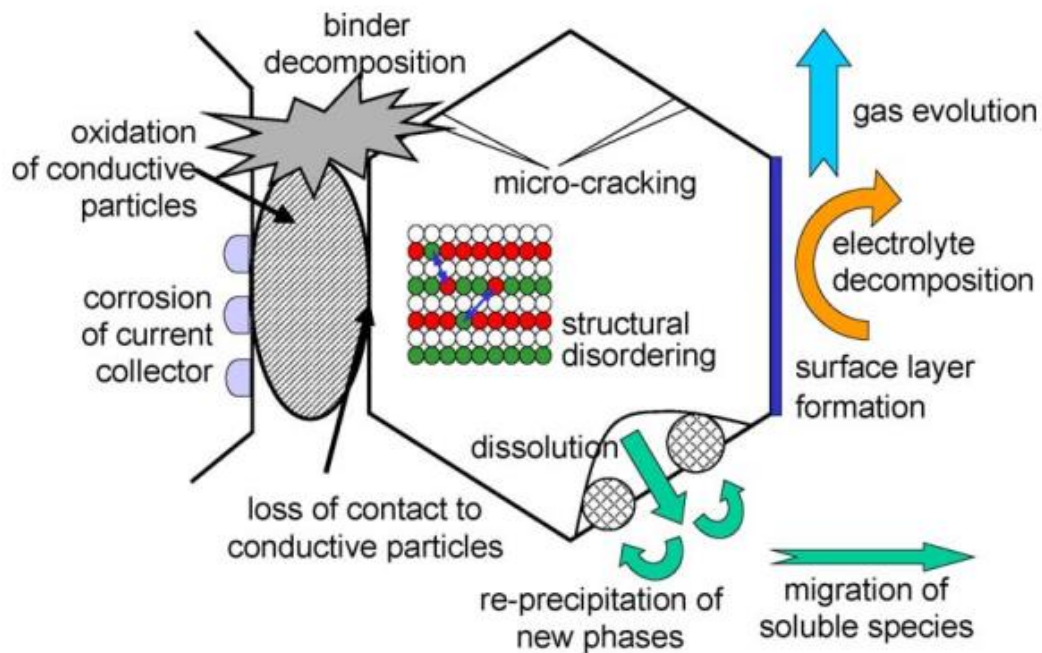
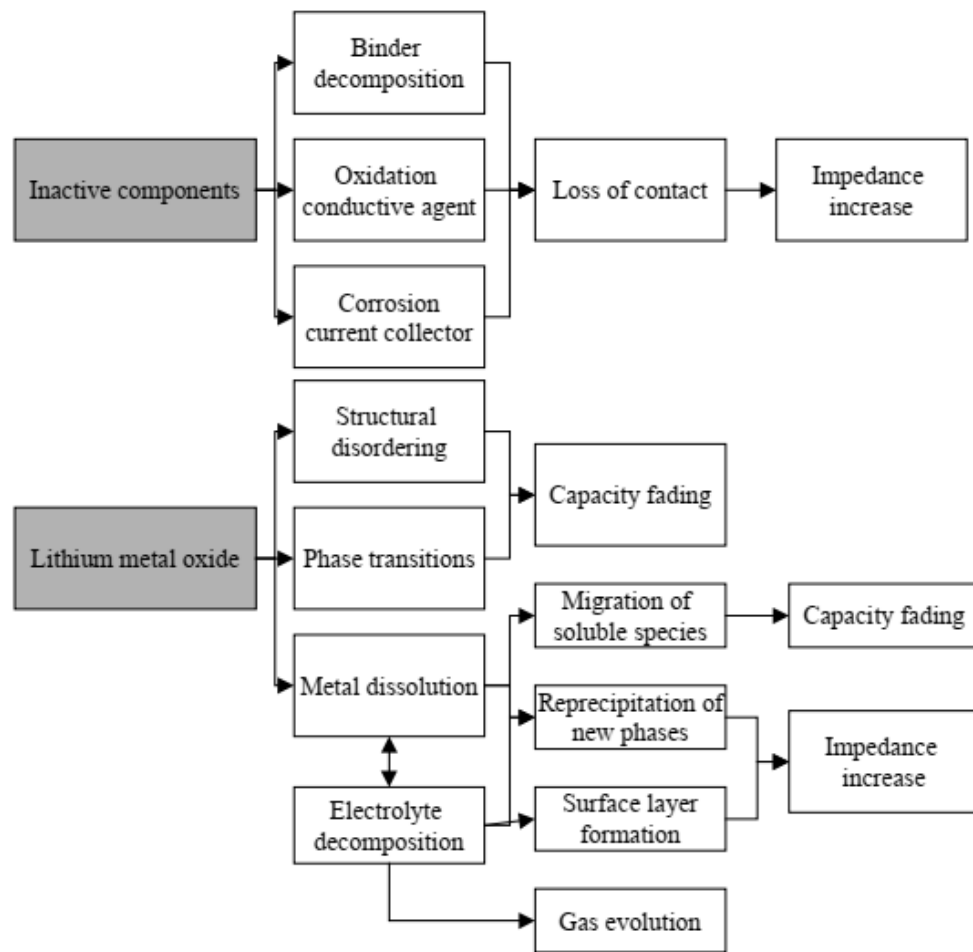Figure 2-7: Overview on basic ageing mechanisms of cathode materials [1]

Figure 2-8: Schematic overview on basic ageing mechanisms of cathode materials [16]

2.3.7 Cyclic Ageing

The ageing process in lithium-ion batteries can occur in two modes, namely cycling and calendar. Cycling ageing is characterized by irreversible losses during charging and discharging cycles. This type of ageing is accelerated by the combined influence of temperature and state of charge (SOC). In addition, the rate of charge/discharge, represented by the C-rate, and the variation of SOC are also important factors that affect the ageing mechanisms during these processes (Santhanagopalan et al., 2014 [17]). Research findings reveal that high values of ΔSOC can lead to a loss of battery power, primarily due to the degradation of the positive electrode and the development of solid electrolyte interphase (SEI) induced by high discharge or charge [8, 14].

Furthermore, the voltage used during charging and discharging can also impact the ageing process. High charging voltage has been observed to increase the degradation

rate in batteries (Kötz et al., 2010 [18]). Discharge voltage, on the other hand, affects battery ageing by increasing the impedance. Additionally, the current peak is also a crucial factor involved in the ageing process. Specifically, a high current peak result in a high level of energy given to or released from the battery [8, 14].

2.3.8 Calendaric Ageing

Ageing in the calendar mode denotes the permanent loss of capacity in a battery when it is in storage or in a rest state, uninfluenced by charge-discharge cycling. It constitutes a crucial factor in numerous lithium-ion battery applications, such as electric vehicles, where the periods of operation are significantly shorter than the periods of inactivity. Additionally, the deterioration attributable to calendar ageing can be the dominant factor in cycle ageing studies, particularly when the depths of the cycles and the current rates are low [19].

During rest, the battery is subject to environmental temperature without any external influence that might accelerate the ageing rate. Storage conditions like temperature and state of charge can either intensify or weaken calendar ageing. In the case of lithium-ion batteries, high temperatures (above 40°C) and low temperatures (below 10°C) lead to a decrease in active ions, which subsequently results in lower ionic interactions and diffusions, leading to capacity fade in the battery. State of charge (SOC) can also be a stress factor for calendar ageing. For identical types of batteries at the same temperature but varying SOC levels, deterioration happens at different rates (Barré et al., 2013 [14]). As SOC levels increase, particularly over 70%, the rate of deterioration increases due to undesirable side reactions that occur at high SOC levels (Palacín, 2018 [20]) [8].

In contrast to cycle ageing, which can cause severe degradation due to mechanical strain in the electrode active materials or lithium plating, the predominant mechanism of calendar ageing is the formation, growth, or reconstruction of passivation layers at the electrode-electrolyte interfaces. These passivation layers consume cyclable lithium resulting from electrolyte decomposition, which involves reduction at the anode and oxidation at the cathode interface. Additionally, the passivation layer growth at the anode, known as the solid electrolyte interphase (SEI), is further catalyzed by dissolved transition-metal ions from the cathode that are reduced again to metals at the anode. Both the evolution of passivation layers and transition-metal dissolution are promoted by a high state of charge (SOC) and temperature [19]. It is important to note that self-discharge rates are highly dependent on storage conditions, which can either accelerate or slow the effects occurring within the battery [14].

In summary, battery calendar ageing is directly influenced by temperature and SOC, as each variable alters the capacity and resistance with a nonlinear effect over time. Moreover, the degradation of capacity and the increase of resistance are not linear over time, indicating a strong interaction of ageing behavior with time [14].

2.4 Float Current Analysis

2.4.1 Battery Self-discharge

Electrochemical capacitors and battery electrodes exhibit high Gibbs energy in their charged states compared to their discharged states, leading to a thermodynamic "driving force" for self-discharge on open-circuit. Self-discharge can occur through mixed cathodic/anodic electrochemical processes or surface-chemical processes. Two procedures can be used to characterize self-discharge: (a) measuring the open circuit decline of electrode potential or state-of-charge over time, and (b) establishing the polarizing currents (float-currents) required to maintain respective potentials constant at various potentials during self-discharge. It is emphasized that characterizing the self-discharge behavior of each electrode of a cell pair individually using a third electrode as a reference is crucial [21].

While self-discharge is always of fundamental interest in the behavior of electrochemical power sources, its practical significance depends on the application of the capacitor device. In load-leveling applications or for bridging short-term power outages, self-discharge may not be practically significant, but for stand-alone or standby applications, where the device must remain online for extended periods before recharging, self-discharge behavior is of major importance for device performance specifications. On open-circuit, self-discharge in batteries or capacitor devices occurs through coupled anodic and cathodic processes, leading to parasitic currents at one or both individual electrodes. Such processes are similar to corrosion of metals on open-circuit, where anodic and cathodic half-cell electrochemical processes occur simultaneously at a single electrode interface at a mixed potential determined jointly by the kinetics of the anodic and cathodic partial processes taking place at a time-dependent common potential [21].

2.4.2 Mechanisms of Self-discharge

In the context of self-discharge phenomena, it is crucial to identify three distinct situations that could affect the experimental design and the interpretation of the results. They are as follows [21]:

a) The first situation happens when self-discharge occurs at electrodes that have been polarized beyond the potentials corresponding to the thermodynamic decomposition potential of the solution. This type of self-discharge proceeds by the continuation of the Faradaic overcharge process.

b) The second situation of self-discharge arises from parasitic processes that involve Faradaic impurity reactions that may be cathodic or anodic, and possibly diffusion-controlled. Battery-type anodes or cathodes may experience such processes, particularly in double-layer-type electrochemical capacitors where impurity parasitic currents are likely to occur.

c) The third scenario, termed as apparent self-discharge, can be observed over relatively short periods following the interruption of polarizing currents at porous-C electrodes due to non-uniformity of charge acceptance amongst pores. Experimental observations and physical simulations of hardware can demonstrate this scenario.

d) In some two-electrode battery configurations, a different origin of self-discharge behavior may arise when products of charging or corrosion at one electrode transfer, by diffusion, to the other electrode, leading to time-dependent depolarization.

e) Lastly, a less complex scenario of self-discharge occurs due to short-circuit leakage currents between adjacent cathodes and anodes in imperfectly sealed bipolar electrode configurations. The kinetics of this scenario are notably distinguishable from those originating from the other situations listed above.

2.4.3 Float Current Analysis Method

In addition to its simplicity and cost-effectiveness, float current analysis has other advantages that make it an attractive option for studying calendaric ageing in lithium-ion batteries. One of these is its ability to reveal subtle differences in ageing mechanisms that may not be easily observable using other methods. For instance, it can distinguish between different modes of degradation such as solid electrolyte interphase (SEI) formation, electrode material degradation, and ageing-induced changes in the active surface area of the electrodes [22]. This ability to differentiate between different degradation mechanisms can help researchers design more effective strategies for improving battery performance and extending their useful life.

Furthermore, float current analysis can also provide information about the effects of different charging protocols on battery ageing. For example, a study by Li et al. [23] found that float current analysis could be used to investigate the effects of different charging voltages and durations on the ageing of lithium-ion batteries. The results showed that higher charging voltages and longer charging durations led to more

severe capacity fading and faster ageing of the batteries. This information can be useful in developing optimal charging protocols that balance the need for rapid charging with the need to minimize battery ageing.

Overall, float current analysis is a powerful tool for studying calendaric ageing in lithium-ion batteries. Its simplicity, cost-effectiveness, and ability to reveal subtle differences in ageing mechanisms and effects of charging protocols make it an attractive option for battery research and development.

2.5 PID Controller

As previously described, the primary aim of this thesis was to devise an intelligent controller that can facilitate the investigation of the calendaric ageing of lithium-ion batteries by employing an electronic test device, named the Floater, to execute float current analysis. The Floater employs a controller to maintain a consistent voltage on the test battery through charging. Initially, the device utilized a conventional proportional-integral-derivative (PID) controller for this purpose, but the novel control algorithm integrates the PID controller with a Fuzzy logic interface. In-depth comprehension of these two control techniques is fundamental for a thorough understanding of the new algorithm as well as the Floater device's functionality. The PID control technique is commonly employed for minimizing the distance between the desired and actual outputs by implementing proportional, integral, and derivative actions. On the other hand, Fuzzy Logic algorithms are suitable for managing intricate and nonlinear systems, thereby enabling the Floater device to adapt to different types of lithium-ion batteries. Therefore, including an overview of these two control techniques in this thesis is vital for demonstrating a complete understanding of the innovative algorithm.

2.5.1 Introduction to PID Control

PID control is a term commonly used to describe three-term control, where the acronym PID represents the initials of the individual components that constitute the standard three-term controller, i.e., the proportional term denoted as 'P', the integral term denoted as 'I', and the derivative term denoted as 'D'. The three-term or PID controllers are extensively utilized in industrial control applications, and even sophisticated control systems may feature a control network in which a PID control module functions as the primary control building block. The three-term PID controller has a long history of utilization and has successfully adapted to the changes in technology from the analog era to the digital computer control system

age. Moreover, it was the first and only controller produced in large quantities to cater to the high-volume market in the process industries [24].

The utilization of the Laplace transform in analyzing the performance of feedback control systems has greatly contributed to its technological success in the engineering community. The theoretical foundation for analyzing the performance of PID control is considerably enhanced by the straightforward representation of an Integrator using the Laplace transform [1/s] and a Differentiator using [s]. The PID controller is conceptually complex, and it can be represented in three different ways. Figure 2-9 displays the various representations of the PID controller. First, there is a symbolic representation (Figure 2-9(a)), in which each of the three terms can be chosen to achieve different control actions. Second, there is a time domain operator form (Figure 2-9(b)), and lastly, there is a Laplace transform version of the PID controller (Figure 2-9(c)). This provides the controller with an s-domain operator interpretation and enables the incorporation of the relationship between the time domain and the frequency domain into the discourse on PID controller performance, as pointed out in reference [24].
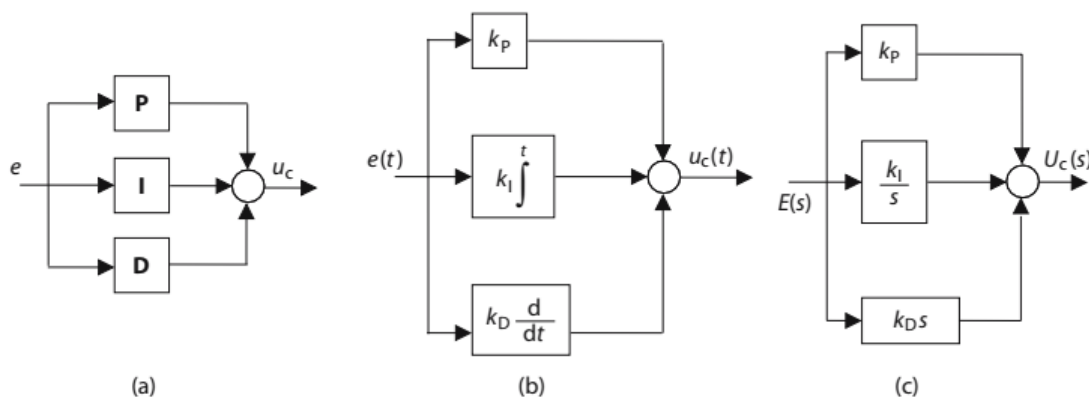
Key :	Controller input (system error) e		PID control signal u_c	
Symbolic forms	e, u_c	Time domain forms	$e(t), u_c(t)$	Laplace domain forms	$E(s), U_c(s)$
Proportional gain	k_P	Integral gain	k_I	Derivative gain	k_D

Figure 2-9: PID controller various representations [24]

2.5.2 PID Controller History

The development of the Proportional-Integral-Derivative (PID) controller spans a historical timeframe of at least 250 years and gaining an understanding of this evolution is essential in comprehending several issues. The technology utilized for implementing controllers has undergone significant changes since its inception. The

initial controllers were mechanical devices such as centrifugal governors which were employed for regulating windmills and steam engines. These devices integrated angular velocity sensing with valve actuation, and the development of integral action was a product of ingenuity [25].

Significant changes transpired with the development of industrial process control, wherein sensing, control, and actuation functions were separated, and dedicated devices for control actions were fabricated. Of interest is the use of pneumatic signal transmission and computing during this period. Notably, a crucial breakthrough occurred with the standardization of pressure levels and tubes used for pressure transmission to 3-15 PSI. This facilitated the integration of sensors, controllers, and actuators from diverse suppliers, and the centralization of controllers in distant control rooms. The implementation of feedback within the controllers, despite the strongly nonlinear nature of components, was an ingenious improvement that enabled linear action [25].

The electronic versions of the PID controller became available in the 1950s, with control actions executed by a straightforward analog computer utilizing operational amplifiers. Another breakthrough transpired with the advent of digital computers for implementing controllers. Initially, centralized systems were predominantly utilized, owing to the high cost of digital computing in smaller systems. However, with the emergence of microprocessors in the 1970s, even simple controllers were implemented using computers. The use of digital computers enables the incorporation of numerous functions, including automatic tuning, adaptation, and diagnostics [25].

2.5.3 PID Controller Terms

The input and output signal configuration for the three-term controller, commonly known as the Proportional-Integral-Derivative (PID) controller, is depicted in Figure 2-10 [24].
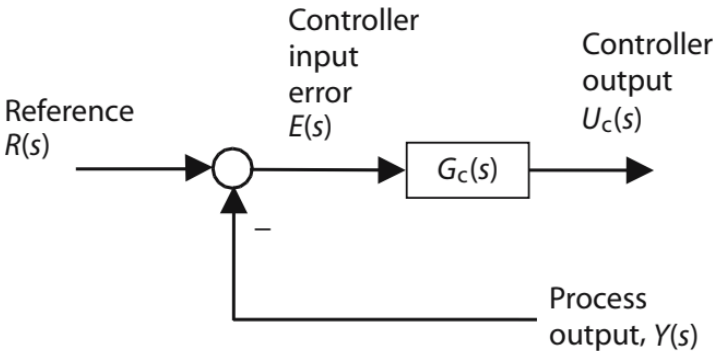
Figure 2-10: PID controller inputs and outputs [24]

2.5.3.1 Proportional Control

In the PID controller, the Proportional (P) term is utilized to effect proportional control, whereby the controller's response is directly proportional to the magnitude of the process error signal e(t) = r(t) - y(t). The corresponding representations of proportional control in the time and Laplace domains are as follows:

$$\text{Time domain: } u_c(t) = k_P\, e(t) \tag{2.6}$$

$$\text{Laplace domain: } U_c(s) = k_P\, E(s) \tag{2.7}$$

The block diagrams for proportional control are depicted in Figure 2-11, where the proportional gain is represented by k_P [24].

Figure 2-11: Block diagrams of the proportional control term [24]

2.5.3.2 Integral Control

The Integral (I) term in the PID controller is utilized for integral control, which corrects for steady deviations from a constant reference signal value. This feature of integral control addresses the limitation of proportional control, as it eliminates the steady-state offset without necessitating an excessive controller gain. The time and Laplace domain representations of integral control are as follows:

$$\text{Time domain: } u_c(t) = k_I \int^{t} e(\tau)d\tau \tag{2.8}$$

$$\text{Laplace domain: } U_c(s) = \left[\frac{k_I}{s}\right] E(s) \tag{2.9}$$

The block diagrams for integral control in the time and Laplace domains are illustrated in Figure 2-12, where the integral controller gain is represented by k_I [24].
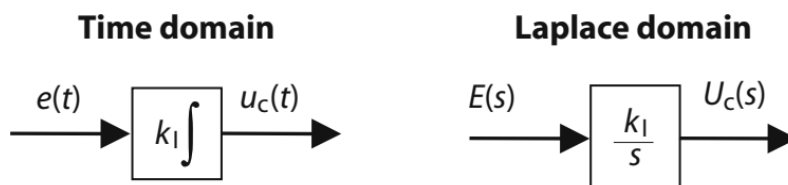
Figure 2-12: Block diagrams of the integral control term [24]

In cases where a controller is capable of utilizing the error signal's rate of change as an input, an element of prediction is introduced into the control action. Derivative control employs the error signal's rate of change and represents the Derivative (D) term in the PID controller. The time and Laplace domain representations for derivative control are as follows:

$$\text{Time domain: } u_c(t) = k_D \frac{de}{dt} \tag{2.10}$$

$$\text{Laplace domain: } U_c(s) = [k_D \, s] \, E(s) \tag{2.11}$$

The gain of derivative control is represented by k_D in the time and Laplace domain representations, which is commonly referred to as pure derivative control. The block diagram representations for pure derivative control are depicted in Figure 2-13 [24].

Time domain   **Laplace domain**

$e(t)$ $\boxed{k_D \dfrac{d}{dt}}$ $u_c(t)$ $E(s)$ $\boxed{k_D s}$ $U_c(s)$
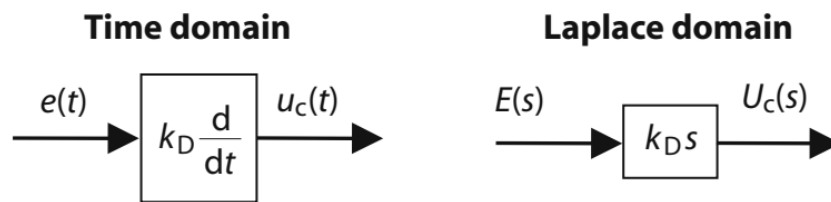
Figure 2-13: Block diagrams of the derivative control term [24]

Incorporating derivative control into a control system requires careful consideration compared to using proportional or integral control. The implementation of a pure derivative control term is often not feasible in practical applications due to the potential amplification of measurement noise. Therefore, a modified form of derivative control may need to be used instead. Nevertheless, derivative control offers useful design characteristics and is an essential component of certain control applications in the real world [24].

2.5.4 Parallel PID Controllers

In order to meet specific performance requirements, the PID controller family is constructed by using various combinations of the proportional, integral, and derivative terms. The formula for the basic parallel PID controller is presented below:

$$U_C(s) = \left[k_P + k_I \frac{1}{s} + k_D s\right] E(s) \tag{2.12}$$

The PID controller family can be attuned to meet specific performance requirements by using various combinations of the proportional, integral, and derivative terms. The most commonly used configuration is the decoupled PID form, which is also known as the parallel configuration. This form is referred to as the textbook PID controller because it does not include any modifications. The PID controller employs three decoupled parallel paths, as illustrated in Figure 2-14, such that a change in any individual coefficient, such as k_P, k_I or k_D, only affects the size of the contribution in the corresponding path. The decoupling of the three terms is a result of the parallel architecture of the PID controller, and a change in any one term does not affect the contributions of the other two terms [24].
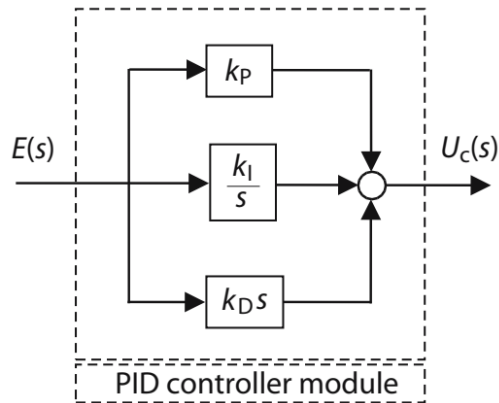
Figure 2-14: Parallel architecture of PID controller [24]

The decoupled branches of the PID controller in the parallel form utilize three straightforward gains: k_P, k_I, and k_D. The parallel architecture of the PID controller can be expressed mathematically in the time domain and Laplace s-domain as follows:

$$\text{Time} - \text{domain formula:} \ \ u_C(t) = k_P e(t) + k_I \int^t e(\tau) d\tau + k_D \frac{de}{dt} \qquad (2.13)$$

$$\text{Transfer function formula:} \ \ U_C(s) = \left[k_P + k_I \frac{1}{s} + k_D s \right] E(s) \qquad (2.14)$$

Within the PID formulas, the proportional gain is denoted by k_P, the integral gain is denoted by k_I, and the derivative gain is denoted by k_D. These gains are used by the controller to act on the time signal of the measured reference error, which is represented as $e(t) = r(t) - y(t)$, or alternatively, in the Laplace domain, $E(s) = R(s) - Y(s)$ [24].

The PID controller is commonly represented in industrial applications using a time constant form for the controller parameters instead of the decoupled form. The time

constant form can be obtained from the parallel form, and the analysis of the time domain formula is presented below. Starting with the parallel time domain formula for the PID controller:

$$u_C(t) = k_P e(t) + k_I \int^t e(\tau) d\tau + k_D \frac{de}{dt} \tag{2.15}$$

The proportional gain k_P can be initially factored out, yielding:

$$u_C(t) = k_P \left(e(t) + \frac{k_I}{k_P} \int^t e(\tau) d\tau + \frac{k_D}{k_P} \frac{de}{dt} \right) \tag{2.16}$$

Define two new time constants, namely:

$$\tau_i = \frac{k_P}{k_I} \quad \text{and} \quad \tau_d = \frac{k_D}{k_P} \tag{2.17}$$

Then:

$$u_C(t) = k_P \left(e(t) + \frac{1}{\tau_i} \int^t e(\tau) d\tau + \tau_d \frac{de}{dt} \right) \tag{2.18}$$

The new form of the PID controller in terms of time constants includes the proportional gain k_P, the integral time constant t_i, and the derivative time constant t_d [24]. A comparable analysis can be applied to the transfer function expressions, which results in:

$$U_C(s) = k_p \left[1 + \frac{1}{\tau_i s} + \tau_D s \right] E(s) \tag{2.19}$$

The aforementioned analysis employs the same definitions for k_P, t_i, and t_d as those presented in the new time domain formula above. Table 2-3 provides the parallel form and industrial time constant forms [24].

	Time domain	Laplace s-domain
Parallel	$u_C(t) = k_P e(t) + k_I \int^t e(\tau) d\tau + k_D \frac{de}{dt}$	$U_C(s) = \left[k_P + k_I \frac{1}{s} + k_D s \right] E(s)$
Time constant	$u_C(t) = k_P \left(e(t) + \frac{k_I}{k_P} \int^t e(\tau) d\tau + \frac{k_D}{k_P} \frac{de}{dt} \right)$	$U_C(s) = k_p \left[1 + \frac{1}{\tau_i s} + \tau_D s \right] E(s)$

Table 2-3: Parallel and time constant forms of PID controller [24]

2.5.5 Series PID Controllers

In the past, some PID controllers were built with pneumatic hardware, for which the series transfer function was a suitable mathematical model. Some manufacturers continued to use this structure in later analog PID devices, leading to its inclusion in some industrial PID controller manuals. However, most modern PID controllers are digital and use parallel form. Despite this, the series PID formulae still persist in some manuals. Figure 2-15 shows a block diagram of the series PID structure, which can be used to derive the overall transfer function $G_{series}(s)$ for this type of PID controller [24].
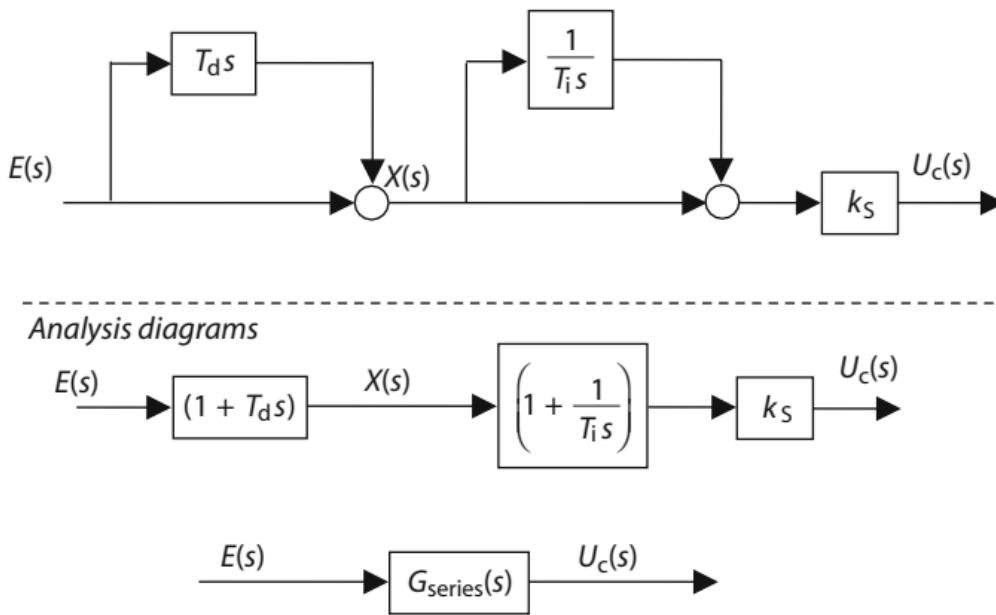
Figure 2-15: Series architecture of PID controller [24]

The fundamental control algorithm for the series PID structure is expressed in terms of a multiplication of transfer functions as follows:

$$U_c(s) = [G_{series}(s)]E(s) = \left[k_S \left(1 + \frac{1}{T_i s} \right) (1 + T_d s) \right] E(s) \tag{2.20}$$

Conversion from the series PID controller to the parallel and time constant PID forms is possible. Using the expanded form for the series PID controller, a rescaling is used to arrive at the usual time constant form:

$$U_c(s) = \left[k_p \left(1 + \frac{1}{\tau_i s} + \tau_d s \right) \right] E(s) \tag{2.21}$$

to give:

$$k_P = k_S \left(\frac{T_i + T_d}{T_i}\right), \quad \tau_i = T_i + T_d \quad \text{and} \quad \tau_d = \left(\frac{T_i T_d}{T_i + T_d}\right) \tag{2.22}$$

Despite the availability of parallel and time constant PID formulae, the series form of the PID controller is still used and referenced by some, as it is considered easier to manually tune by some practitioners [24].

2.5.6 When Can PID Control Be Used?

A controlled system is subject to various requirements, such as a satisfactory response to setpoint changes, the ability to reject load disturbances, and the minimization of control actions due to measurement noise, while maintaining insensitivity to process variations. The design of a control system also takes into consideration factors such as process dynamics, actuator saturation, etc. Despite its simplicity, the PID controller is a commonly used controller in industry, and it is generally observed that it can provide satisfactory control performance for most industrial processes, as long as the required control performance is not overly demanding [25].

2.5.6.1 When is PI control sufficient?

If the performance requirements are modest, all stable processes can be controlled by an integral controller, with additional performance enhancements provided by proportional action. The PI controller is therefore the most commonly used controller. For processes with first-order dynamics, a PI controller can provide any desired performance, disregarding saturations. PI control can also be applied to processes with integral action. Derivative action is often not utilized, with many industrial controllers having only PI action or allowing for the switching off of derivative action. PI control has been shown to be sufficient for all processes with first-order dynamics, such as level controls in single tanks and stirred tank reactors with perfect mixing. This can be confirmed by measuring the step response or frequency response of the process. Additionally, some processes may not require tight control, and in such cases, integral action can provide a zero steady-state offset and adequate transient response through proportional action, even if the process has higher-order dynamics [25].

2.5.6.2 When is derivative action useful?

A PI controller is inadequate for controlling a double integrator process due to the process's inherent 180° phase lag, which is also present in the PI controller. To compensate for this phase lag, derivative action is required. Conversely, a PID

controller can achieve any desired performance for a process with second-order dynamics. However, for processes with dominant second-order dynamics, PID control is adequate, and there are no additional benefits obtained by using a more complex controller. An example where derivative action can improve the response is when the process has time constants with significantly different magnitudes, such as temperature control. Additionally, derivative control can be advantageous in higher-order systems that require tight control, as it provides improved damping, enabling a higher proportional gain to speed up the transient response. When dealing with processes that have essentially monotonic step responses with time delay, derivative action provides only modest performance improvements compared to PI control. However, for lag-dominated processes, significant improvements can be achieved with derivative action. In summary, PID control is sufficient for processes with simple dynamics, and more sophisticated controller structures are necessary for processes with more complex dynamics [25].

2.5.7 PID Design and Tuning

Although the concept of designing and tuning a proportional-integral-derivative (PID) controller appears to be intuitive, it can be a challenging task in practice when attempting to achieve multiple and sometimes conflicting objectives such as short transient response and high stability. Typically, initial designs require multiple adjustments through computer simulations to ensure that the closed-loop system performs as desired, or compromises are made [26].

Proportional-integral-derivative (PID) control is a popular control solution for addressing both transient and steady-state responses in a range of real-world control applications. Despite advances in digital control technology and the availability of alternative control schemes, over 90% of industrial controllers remain based on PID algorithms. This is largely due to the fact that PID controllers are simple, offer clear functionality, are widely applicable, and are easy to use, all of which make them an attractive option for industrial control applications, particularly at lower levels [26].

The "three-term" functionalities of the PID controller can be emphasized as follows:

- The proportional term—providing an overall control action proportional to the error signal through the all-pass gain factor.
- The integral term—reducing steady-state errors through low-frequency compensation by an integrator.
- The derivative term—improving transient response through high-frequency compensation by a differentiator.

Table 2-4 summarizes the individual effects of the proportional, integral, and derivative terms on the performance of the closed-loop system for stable open-loop plants. However, it should be noted that this table only serves as a preliminary guide, as the values of k_P, k_I (or T_I), and k_D (or T_D) are interdependent and need to be tuned for optimum performance. While it is commonly believed in academia that increasing the derivative gain, k_D, will improve stability, practitioners have found that this is not always the case, particularly when there is a transport delay. As a result, many practitioners have chosen to disable or remove the derivative term altogether due to difficulties in tuning [26].

Closed-Loop Response	Rise Time	Overshoot	Settling Time	Steady-State Error	Stability
Increasing K_P	Decrease	Increase	Small Increase	Decrease	Degrade
Increasing K_I	Small Decrease	Increase	Increase	Large Decrease	Degrade
Increasing K_D	Small Decrease	Decrease	Decrease	Minor Change	Improve

Table 2-4: Effects of P, I, and D tuning independently [26]

2.5.8 PID Controller Implementation Issues

In the subject of industrial PID control, pre-packaged controllers are often utilized. Prior to engaging in a tuning exercise, it is essential to comprehend the implementation of the PID controller. This typically involves a meticulous analysis of the User Manual provided by the manufacturer. While manufacturers may have introduced customized features to address specific problems encountered in industrial PID control, some of which may remain confidential, there are common difficulties that arise in the implementation of the PID controller. It is beneficial to review general solutions and terminology even if specific industrial details are unavailable. Table 2-5 presents common process control issues and the appropriate solutions for PID implementation [24].

► Process control problem	► PID control solution
Measurement noise	
• Significant measurement noise on process variable in the feedback loop • Noise amplified by the pure derivative term • Noise signals look like high frequency signals	• Replace the pure derivative term by a bandwidth limited derivative term • This prevents measurement noise amplification
Proportional and derivative kick	
• P- and D-terms used in the forward path • Step references causing rapid changes and spikes in the control signal • Control signals are causing problems or outages with the actuator unit	• Move the proportional and derivative terms into feedback path • This leads to the different forms of PID controllers which are found in industrial applications
Nonlinear effects in industrial processes	
• Saturation characteristics present in actuators • Leads to integral windup and causes excessive overshoot • Excessive process overshoots lead to plant trips as process variables move out of range	• Use anti-windup circuits in the integral term of the PID controller • These circuits are often present and used without the installer being aware of their use
Negative process gain	
• A positive step change produces a wholly negative response • Negative feedback with such a process gives a closed-loop unstable process	• Use the option of a reverse acting PID controller structure

Table 2-5: Process control problems and corresponding PID controller solutions [24]

2.6 Fuzzy Control

Fuzzy control is frequently considered as a type of nonlinear PID control and can be used as an alternative solution for systems that are too complicated to be adequately controlled by a conventional PID. While conventional PID control is widely used and can meet the performance requirements of most setpoint regulation problems with

low cost, the performance improvements provided by fuzzy control are often insufficient to offset the increased complexity in computation and tuning. As a result, fuzzy control is predominantly employed in situations in which the conventional control techniques cannot provide acceptable performance [27].

2.6.1 Introduction to Fuzzy Logic

We must exploit our tolerance for imprecision.

Lotfi Zadeh, 1973

Professor, Systems Engineering, UC Berkeley

In the field of engineering, it is common for texts to overlook the inherent uncertainty in the information, models, and solutions presented in the problems they describe. Achieving high levels of precision often involves a significant investment of time and/or resources. As the complexity of a system increases, the available information to accurately characterize that system becomes more imprecise or inexact. Thus, precision, information, and complexity are closely linked in the problems that engineers attempt to solve. Despite this, Professor Zadeh's quote suggests that in many cases, it is possible to achieve satisfactory results by accepting a certain degree of imprecision [28].

The prevalent method for quantifying uncertainty in scientific models from the late nineteenth to the late twentieth century was probability theory. However, this approach gradually faced challenges, beginning with Max Black's study on vagueness in 1937, and later with the introduction of fuzzy sets by Zadeh in 1965. Zadeh's work had a significant impact on the understanding of uncertainty because it not only questioned probability theory as the exclusive representation of uncertainty, but also challenged the fundamental principles upon which probability theory was built, namely, classical binary logic [28].

During the twentieth century, new paradigms were developed to address uncertainty beyond the random kind, challenging the traditional probability theory and classical Aristotelian logic. Jan Lukasiewicz developed a discrete, multivalued logic in the 1930s. Arthur Dempster introduced a theory of evidence in the 1960s, which included the assessment of ignorance. In 1965, Lotfi Zadeh proposed fuzzy set theory as a continuous-valued logic. In the 1970s, Glenn Shafer extended Dempster's work to form a complete theory of evidence that handles information from multiple sources, while Zadeh introduced possibility theory as a special case of fuzzy sets. In the 1980s, further research showed a strong connection between evidence theory, probability theory, and possibility theory with the use of fuzzy and monotone measures [28].

Lotfi Zadeh proposed that decision making under uncertainty can be based on set membership. His seminal paper of 1965 presented the following statement:

> *The notion of a fuzzy set provides a convenient point of departure for the construction of a conceptual framework which parallels in many respects the framework used in the case of ordinary sets, but is more general than the latter and, potentially, may prove to have a much wider scope of applicability, particularly in the fields of pattern classification and information processing. Essentially, such a framework provides a natural way of dealing with problems in which the source of imprecision is the absence of sharply defined criteria of class membership rather than the presence of random variables* [29].

The concept of set membership plays a pivotal role in defining objects within a universe using sets. Classical sets include objects that fulfill precise membership properties, while fuzzy sets encompass objects that fulfill vague membership properties, meaning that membership of an object in a fuzzy set can be approximate. For instance, the set of heights between 5 to 7 feet is precise (or crisp), whereas the set of heights in the vicinity of 6 feet is imprecise (or fuzzy) [28].

2.6.2 Fuzzy Sets

Zadeh expanded upon the concept of binary membership by introducing the notion of "degrees of membership" which could be represented on the real continuous interval [0,1]. The endpoints of 0 and 1 correspond to no membership and full membership, respectively, similar to the indicator function for crisp sets. However, the infinite values between the endpoints can represent different levels of membership for an element x in a set on the universe. Zadeh referred to these sets on the universe *X* that can accommodate "degrees of membership" as fuzzy sets [28].

When dealing with fuzzy sets, there is no unique membership function due to the imprecise nature of the property being considered. Therefore, the analyst must determine the membership function, denoted as μ_H, for a set *H*, such as the set of heights near 6 feet. Properties that could be considered for the membership function include normality (where $\mu_H(6) = 1$), monotonicity (where *H* closer to 6 yields higher μ_H values), and symmetry. Figure 2-16(b) shows an example of a membership function with these properties, while Figure 2-16(a) illustrates a crisp set with a well-defined membership function. However, fuzzy sets can have an infinite number of membership functions with different properties, such as asymmetry, depending on the requirements of the application. One key difference between crisp and fuzzy sets is that while crisp sets have a unique membership function, fuzzy sets provide more

flexibility because the membership function can be tailored to suit a specific application [28].
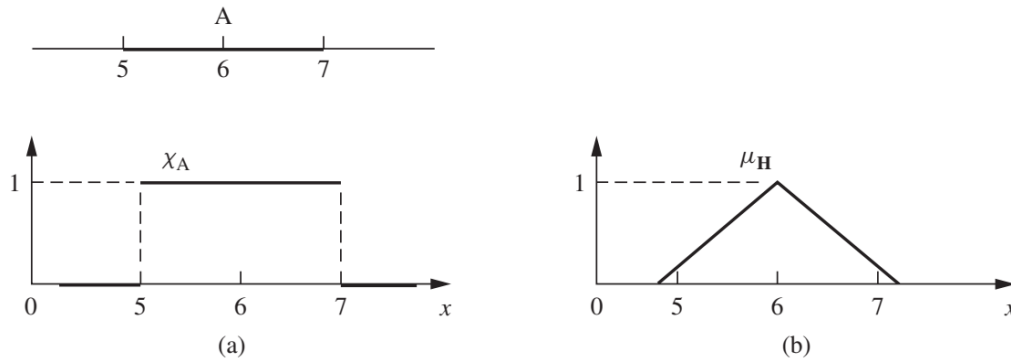
Figure 2-16: Membership functions for (a) a crisp set A and (b) a fuzzy set H [28]

In the context of fuzzy sets, every set is represented as a function that maps a universe of objects, X, onto the unit interval [0,1]. This means that a fuzzy set H is the function μ_H that takes X into [0,1]. Therefore, any function that maps X onto [0,1] can be considered a fuzzy set. The membership function serves as the mathematical expression of the degree of membership of an object in a set. Throughout this thesis, the notation used to denote a fuzzy set is a set symbol with a tilde underscore, such as $\widetilde{A}$, and its functional mapping is expressed as:

$$\mu_{\widetilde{A}}(x) \in [0,1] \tag{2.23}$$

and the symbol $\mu_{\widetilde{A}}(x)$ represents the degree of membership of element x in the fuzzy set $\widetilde{A}$. The membership function $\mu_{\widetilde{A}}(x)$ takes a value between 0 and 1, and measures the degree to which x belongs to $\widetilde{A}$. In other words, $\mu_{\widetilde{A}}(x)$ indicates the degree of compatibility between x and $\widetilde{A}$, or equivalently, $\mu_{\widetilde{A}}(x)$ = degree to which x $\in \widetilde{A}$ [28].

2.6.3 Fuzzy Membership Functions

Fuzzy membership functions may exhibit varying degrees of mathematical complexity. However, given that fuzzy logic is designed to handle imprecision, incorporating complex membership functions is unlikely to improve the accuracy of the output. The subsequent discussion will showcase a range of fuzzy membership functions.

2.6.3.1 Singleton membership function

The Singleton membership function is a type of fuzzy membership function that assigns a membership value of 1 to a particular value of x and assigns a value of 0 to

all other values. This function is represented by the impulse function, as depicted in Figure 2-17. Mathematically it is formulated as follows [30].

$$\mu(x) = \begin{cases} 1, & \text{if } x = c \\ 0, & \text{otherwise} \end{cases} \tag{2.24}$$
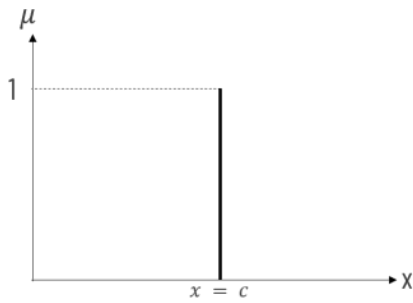
Figure 2-17: Singleton membership function [30]
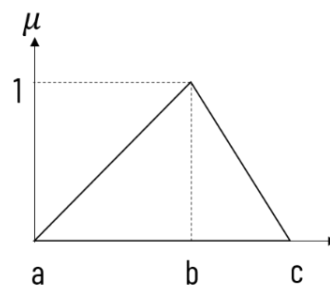
Figure 2-18: Triangular membership function [30]

2.6.3.2 Triangular membership function

The triangular membership function is one of the most commonly used membership functions in fuzzy controller design. This function represents the fuzzification of the input using three parameters: a, b, and c. The parameters a and c represent the bases of the triangle, while b represents its height. The function is graphically represented as shown in Figure 2-18. The single equation for triangular membership function is shown below [30].

$$\mu_{\text{triangle}}(x; a, b, c) = \begin{cases} 0, & x \leq a \\ \dfrac{x-a}{b-a} & a \leq x \leq b \\ \dfrac{c-x}{c-b} & b \leq x \leq c \\ 0, & c \leq x \end{cases} = \max\left(\min\left(\dfrac{x-a}{b-a}, \dfrac{c-x}{c-b}\right), 0\right) \tag{2.25}$$

A triangular-shaped membership function can be transformed into S-shaped and Z-shaped membership functions. The S-shaped membership function has its parameter c outside the definition area of the function, while the Z-shaped membership function has its parameter a outside the definition area. The S-shaped and Z-shaped membership functions are shown in Figure 2-19 and Figure 2-20, respectively [30, 31].
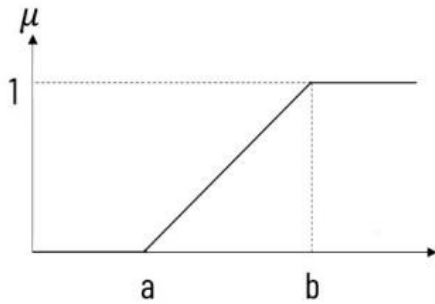
Figure 2-19: S-shaped membership function [30]   Figure 2-20: Z-shaped membership function [30]
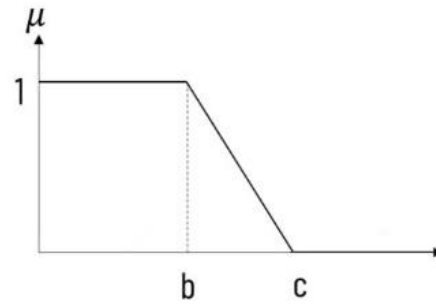
2.6.3.3   Trapezoidal membership function

The trapezoidal membership function, a common fuzzy set function, is characterized by four parameters: a, b, c, and d. The highest membership value that an element can take is represented by the span between b and c. If an element x lies between (a, b) or (c, d), it is assigned a membership value between 0 and 1. Figure 2-21 illustrates the trapezoidal membership function. The single equation for trapezoidal membership function is shown below [30].

$$\mu_{\text{triangle}}(x; a, b, c) = \begin{cases} 0, & x \leq a \\ \dfrac{x-a}{b-a}, & a \leq x \leq b \\ 1, & b \leq x \leq c \\ \dfrac{d-x}{d-c}, & c \leq x \leq d \\ 0, & d \leq x \end{cases} = \max\left(\min\left(\frac{x-a}{b-a}, 1, \frac{d-x}{d-c}\right), 0\right) \qquad (2.26)$$
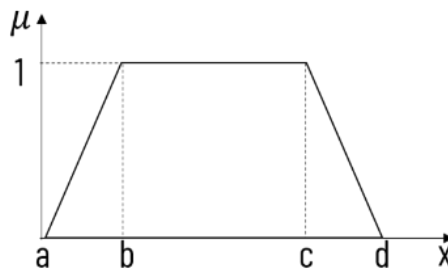
Figure 2-21: Trapezoidal membership function [30]

2.6.3.4   Gaussian membership function

A Gaussian membership function can be defined by two parameters $\{m, \sigma\}$, and it can be represented by the following equation:

$$\mu_{gaussian}(x; m, \sigma) = e^{-\frac{1}{2}\left(\frac{x-m}{\sigma}\right)^2} \tag{2.27}$$

Figure 2-22 shows the Gaussian membership function. The Gaussian membership function is defined by two parameters, namely, the mean (m) and standard deviation (σ), which represent the center and spread of the Gaussian curve, respectively. While this function is a more realistic representation of the data distribution, its mathematical complexity limits its applicability for fuzzification purposes [30].
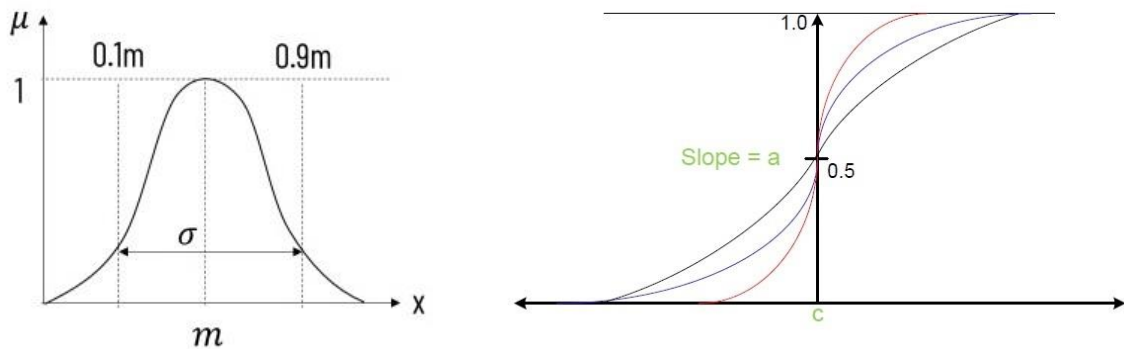
Figure 2-22: Gaussian membership function   Figure 2-23: Sigmoid membership function [30]
[30]

2.6.3.5   Sigmoid Membership function

Sigmoid functions are commonly employed in classification tasks within machine learning, such as logistic regression and neural networks, where they are utilized to compress the input and map it onto the interval [0,1]. The shape of the sigmoid function is determined by two parameters, a and c. The parameter a controls the slope of the function at the point of intersection, where $x = c$. Figure 2-23 shows the graphical representation of the Sigmoid membership function [30]. Mathematically, it is expressed as:

$$\mu_{gaussian}(x; a, c) = \frac{1}{1 + e^{-a(x-c)}} \tag{2.28}$$

2.6.4 Fuzzification of Inputs

Fuzzification refers to the process of converting crisp data into fuzzy data, thereby acknowledging the inherent uncertainty and imprecision present in many real-world

scenarios. This is achieved by recognizing that many of the seemingly crisp and deterministic quantities actually carry considerable uncertainty. If the uncertainty arises due to imprecision, ambiguity, or vagueness, the variable is classified as fuzzy and can be represented using a membership function [28].

In practical scenarios, hardware such as digital voltmeters often generate crisp data. However, if the input process is quantitative or derived from sensor measurements, the crisp numerical inputs can be fuzzified to facilitate their use in a fuzzy inference system. In other words, Fuzzification is a means of encoding knowledge about the real world into a form that can be processed by a computer. It allows us to capture the complexities and uncertainties of real-world problems and represent them in a way that is useful for decision-making. Fuzzification has broad applications in fields such as control systems, pattern recognition, and artificial intelligence, where dealing with imprecise and uncertain data is crucial [28].

2.6.5 Fuzzy Rules

To enable the application of fuzzy logic reasoning, it is necessary to express fuzzy rules using an implication function. This fuzzy implication function serves the same purpose as the truth table of the classical implication in classical logic. The classical implication is represented by the following symbol in classical logic:

$A \rightarrow B$

This symbol is representation of the statement:

If A **then** B

Within the framework of fuzzy logic, these forms of declarations are commonly known as fuzzy if-then statements or fuzzy rules. An implication function in fuzzy logic can be employed to represent a fuzzy rule through a fuzzy relation. A fuzzy rule comprises an if-then statement, in which both the premise and the consequent entail fuzzy propositions. The premise of a fuzzy rule may consist of various propositions combined through logical connectives, namely *and* and *or*. Additionally, a fuzzy proposition may be formulated by means of negation. In order to simplify the analysis, the following rule is considered:

If x_1 is A_1 **then** x_2 is A_2 **then** y is B

Once the membership functions $\mu_{A_1}(x_1)$, $\mu_{A_2}(x_2)$, and $\mu_B(y)$ have been assigned to fuzzy sets A_1, A_2, and B, the resulting fuzzy rule can be expressed through the following fuzzy relation R:

$$R = I(T(A_1, A_2), B) \tag{2.29}$$

The conjunction T, utilizing a generalized T-norm, and the fuzzy implication function I, represent the *and* and $if - then$ connectives, respectively. Accordingly, the fuzzy rule can be portrayed by means of a fuzzy relation. The membership function of the aforementioned example's fuzzy relation R can be expressed as follows:

$$\mu_R(x_1, x_2, y) = I(T(\mu_{A_1}(x_1), \mu_{A_2}(x_2)), \mu_B(y)) \tag{2.30}$$

The implication function I is generally denoted by $I(a, b)$ where $a, b \in [0,1]$ [32].

A set of characteristics must be adhered to by fuzzy rules, namely consistency, continuity, and completeness, to ensure the reliability of the fuzzy rule base. Continuity of a rule base stipulates that rules featuring premises that are "adjacent" must have corresponding consequences that are also "adjacent." Rule premises are regarded as adjacent if they involve identical conditions (fuzzy sets), with the exception of one condition in which the involved fuzzy sets must be contiguous. The continuity of a rule base is of utmost significance when the fuzzy implications utilized to exemplify the fuzzy rules conform to the classical implication [32].

Consistency of a rule base pertains to the coherence of the knowledge embodied by the rule base. A widely recognized instance of an inconsistent rule base is one utilized in the control of a robot, which incorporates two fuzzy rules and the data "obstacle in front":

If obstacle in front **then** go left

If obstacle in front **then** go right

It can be argued that this is an inadequately structured rule base. Nonetheless, such inconsistencies are difficult to avoid in intricate rule bases. Furthermore, the utilization of or connectives in rule premises may contribute to the emergence of such issues [32].

Completeness of a fuzzy rule base can serve as an indicator of the thoroughness of the knowledge encapsulated by the rule base. An incomplete rule base has what is referred to as blank spots, wherein no output actions are specified for specific scenarios in the input space on a semantic level. However, this does not signify that the inference outcome of an incomplete rule base is non-existent, as the fuzzy sets featured in the rule premises play a crucial part in this context [32].
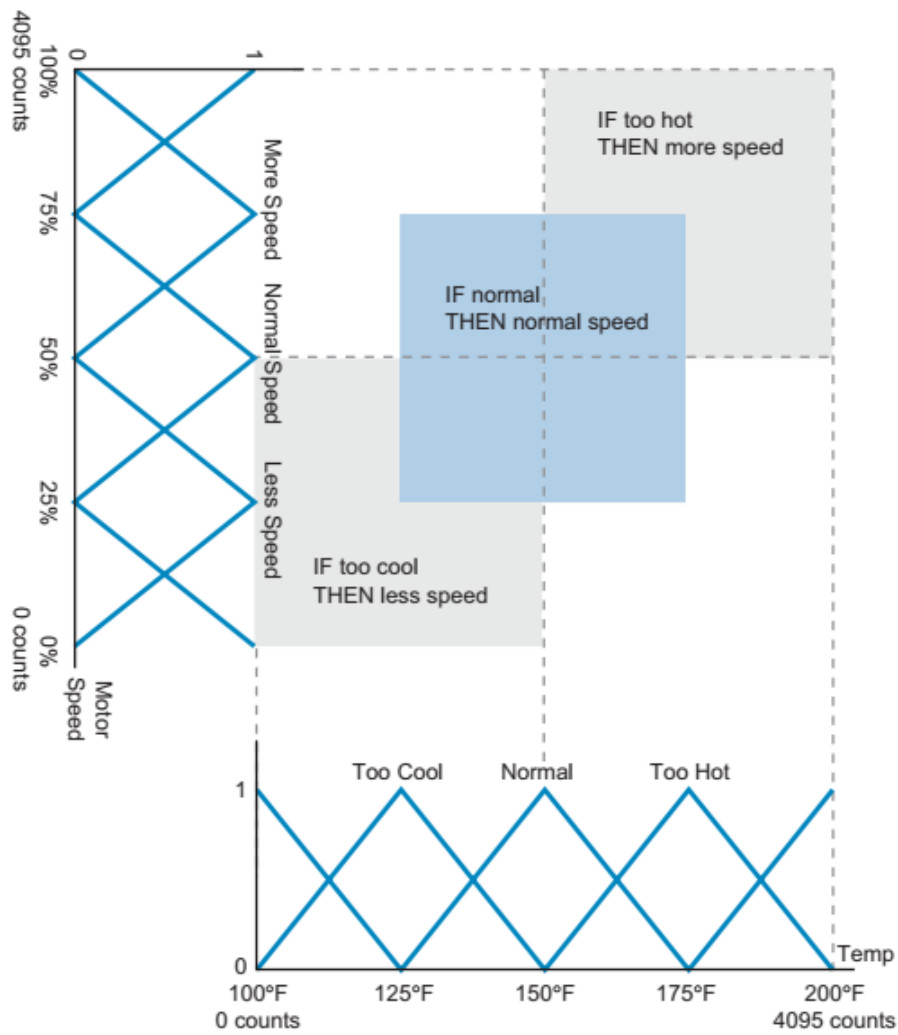
Figure 2-24: Fuzzy logic system chart showing both inputs and outputs grades [33]

2.6.6 Fuzzy Logic Operation

Figure 2-24 portrays a fuzzy logic cooling system diagram with input and output grades depicted. The horizontal axis of the diagram corresponds to the input condition (temperature), while the vertical axis denotes the output (air-conditioner motor speed). The chart is designed in such a way that a single input condition can trigger multiple output conditions. For instance, in case the input temperature is 137.5°F, it belongs to two input curves, signifying that it is 50% too cool and 50% normal. Thus, the input would trigger two output conditions. The "too cool" input condition would prompt a lower speed output, whereas the "normal" input would trigger a typical speed output condition. As the fuzzy logic controller can only have one output, it executes a process referred to as defuzzification (elucidated subsequently) to determine the ultimate output value [33].

2.6.7 Defuzzification of Outputs

In order to obtain a numerical representation of the fuzzy output of a fuzzy controller, the process of defuzzification is required. From a theoretical perspective, the fuzzy output can be a multi-dimensional fuzzy set (fuzzy relation) if the controller has multiple outputs, resulting in a multi-dimensional fuzzy output set for the controller. Numerous methods are available for defuzzification of fuzzy relations such as the Center of Gravity, Mean of Maxima, Center of Sums, and Weighted Average [32].

2.6.7.1 Center of Gravity

The Center of Gravity (COG) is a widely used defuzzification method that is both physically intuitive and mathematically sound. The Center of Gravity method is based on the same principle as that used to determine the center of gravity of a physical object. However, instead of using physical masses, membership values are employed. The mathematical formula for the center-of-gravity defuzzification method is as follows:

$$x^* = \frac{\int \mu_C(x)x\,dx}{\int \mu_C(x)\,dx} \tag{2.31}$$

In discrete mode, the centroid or center of gravity and area of each subregion are computed. Subsequently, the sum of all these sub-areas is utilized to establish the defuzzified value for a discrete fuzzy set. The discrete form can be expressed as:

$$x^* = \frac{\sum_{i=1}^{n} \mu_C(x_i) \cdot x_i}{\sum_{i=1}^{n} \mu_C(x_i)} \tag{2.32}$$

The number of quantizations applied to discretize the membership function $\mu_C(x)$ of the fuzzy output is denoted by n. The defuzzification value for a discrete fuzzy set is determined by computing the area and centroid of each subregion in the discrete mode, followed by summing all these sub-areas. An illustration of the Center of Gravity defuzzification method is presented in Figure 2-25. This information has been sourced from [30, 32].
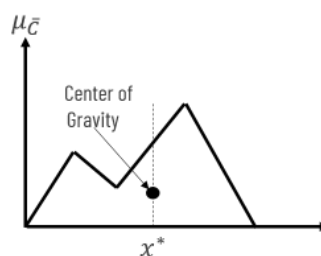
Figure 2-25: Center of Gravity (COG) defuzzification method [30]

2.6.7.2 Mean of Maxima

Another fundamental defuzzification method is the Mean of Maxima (MOM) method. This method is based on the position of maximum membership of an element within a fuzzy set to obtain the crisp output. The Mean of Maxima method can be defined as follows:

$$x^* = \frac{\sum_{x_i \in M}(x_i)}{|M|} \tag{2.33}$$

where, $M = \{x_i \mid \mu_c(x_i) = h(C)\}$, or M denotes the set of points with the highest membership value in the Mean of Maxima (MOM) defuzzification method. An example of the MOM method is illustrated in Figure 2-26 [30].
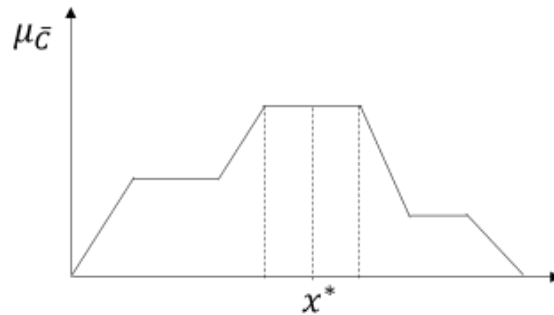
Figure 2-26: Mean of Maxima (MOM) defuzzification method [30]

2.6.7.3 Center of Sums

The Center of Sums (COS) method is a commonly used defuzzification method, where the overlapping region is given multiple counts, unlike the Center of Gravity (COG) method that counts it only once. However, both methods follow the same fundamental approach for computing a crisp value. The defuzzified value using the Center of Sums (COS) method is defined as:

$$x^* = \frac{\sum_{i=1}^{n} A_i \cdot x_i}{\sum_{i=1}^{n} A_i} \tag{2.34}$$

Here, A_i denotes the area of each region bounded by the corresponding fuzzy set, while the geometric center of that area is represented by x_i. The calculation procedure of the COS defuzzification method is illustrated in Figure 2-27, which demonstrates the computation of the crisp value based on the area of overlapping regions and their geometric centers [30].
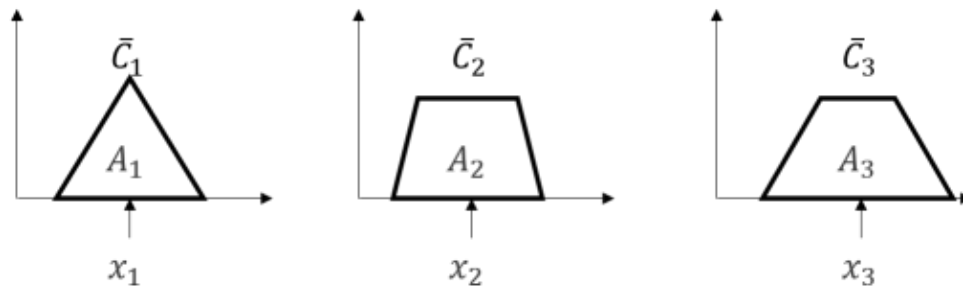
Figure 2-27: Center of Sums (COS) defuzzification method [30]

2.6.7.4 Weighted Average

The Weighted Average method is a commonly used and straightforward defuzzification technique that is applicable to fuzzy sets with symmetrical output membership functions. This method yields results that are quite similar to the Center of Gravity (COG) method and requires less computational power. The maximum membership value is utilized to weigh each membership function. The resulting crisp value is defined as follows:

$$x^* = \frac{\sum_{i=1}^{n} \mu_{C_i}(x_i) \cdot x_i}{\sum_{i=1}^{n} \mu_{C_i}(x_i)} \tag{2.35}$$

The procedure yields results that are very similar to those obtained using the COA method. Figure 2-28 illustrates the calculation process of the Weighted Average defuzzification method [30].
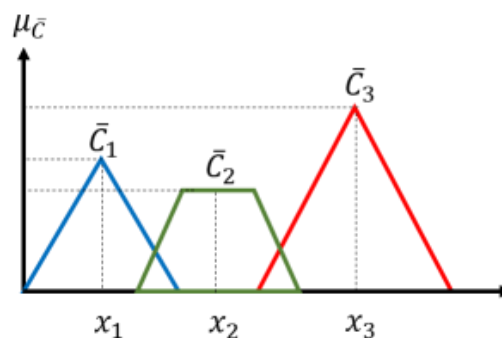
Figure 2-28: Weighted Average defuzzification method [30]

2.6.8 Why Fuzzy + PI Controller

The PI controller is widely used in control systems due to its simplicity and ability to provide satisfactory performance across a wide range of operations. However, a major drawback of this conventional controller is the difficulty in selecting appropriate PI gains, as fixed gains may not yield the required control performance

when system parameters or operating conditions vary. Thus, an online tuning process is necessary to ensure that the controller can handle all variations in the system. Several AI-based techniques have been proposed to tune the gains of PI controllers, including the self-tuning fuzzy logic technique for online adaptive tuning of the PI controller. This technique allows for online tuning of the controller gains with changes in system conditions, and its advantage lies in being a model-free strategy that uses human experience to generate the tuning law. The controller consists of both a fuzzy controller and a PI controller, and based on the error and error rate of the control system and fuzzy control rules, the fuzzy controller can adaptively adjust the two parameters of the PI controller to accommodate any variations in system parameters and/or operating conditions [34].

3. Methodology

In this chapter, the methodology used in the design and implementation of an intelligent fuzzy PI controller for float current analysis tests on lithium-ion battery cells is presented. The design process included the development of a fuzzy logic control algorithm to exclude the manual gains tuning process and also to enhance the performance of the conventional PI controller. The experimental setup for the float current analysis tests is also discussed, which involved the Floater test equipment, lithium-ion battery cell, and Raspberry-Pi module as a data acquisition system to log the measurements of the battery's charging current and voltage. The experimental tests were conducted on two different lithium-ion battery cell types to evaluate the controller's performance.
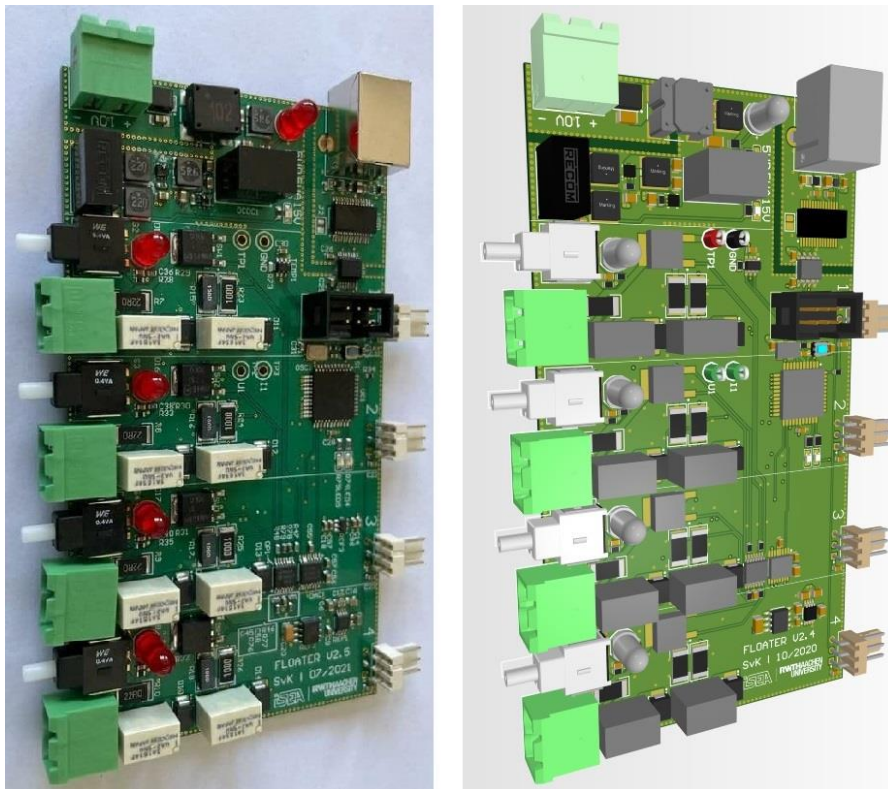
Figure 3-1: Manufactured and 3D model of Floater test device

3.1   Floater Test Device

The Floater device operates on the principle that the deviation of the battery cell voltage from the target battery cell voltage (so-called controller setpoint voltage) should be minimized. To achieve this objective, the embedded control system regulates the charging current in a manner that minimizes the voltage difference. The device is designed to operate at an operating voltage of 10 V_{DC} and up to four battery cells can simultaneously connect to the Floater. The maximum charging current capacity of the device is 250 mA per battery cell. Figure 3-1 shows the Floater test device.

The main components of the Floater device include a couple of instrumental and operational amplifiers, and a low-power CMOS (Complementary Metal Oxide Semiconductor) microcontroller model, Atmel picoPower® ATmega324P [35]. This microcontroller is an 8-bit Reduced Instruction Set Computer (RISC) microcontroller [36]. RISC systems facilitate the use of the microprocessor's instructions by operating system and application programmers to develop code with a smaller instruction set [37].
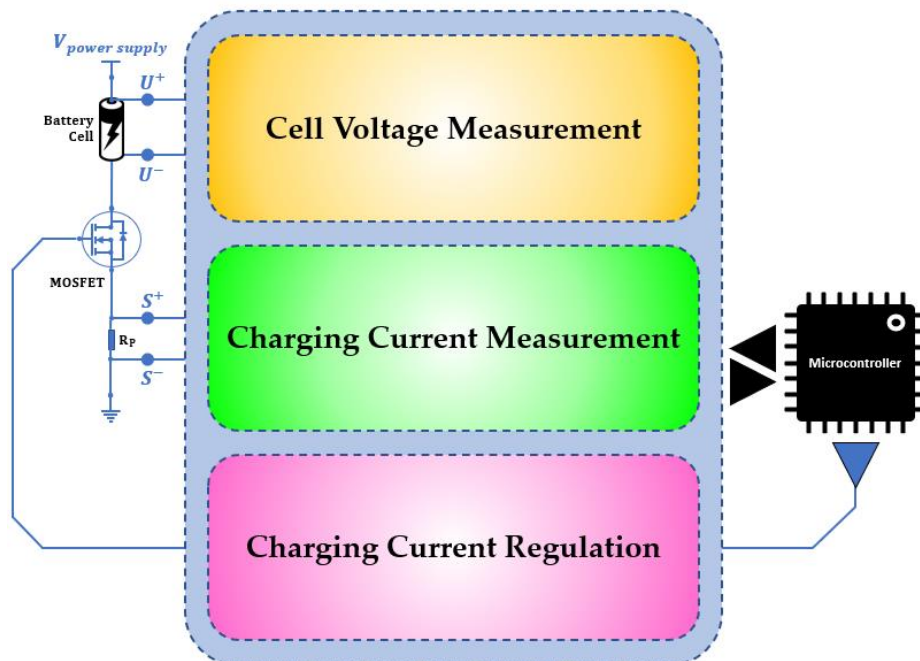
Figure 3-2: Block diagram of the Floater electronic test device

The ATmega family of microcontrollers, including the ATmega324P model, are relatively simple to configure, without the need for several layers of hardware abstraction. This feature makes the ATmega324P microcontroller suitable for certain

classes of applications, such as controllers dedicated to performing specific control tasks. However, the processing capability of this microcontroller must be carefully considered for the desired application, as it lacks performance compared to higher bit microcontrollers [36]. In summary, the Floater device is simple to configure but requires careful consideration of the processing capability for the specific application.

The block diagram of the Floater test device is depicted in Figure 3-2. The device consists of three essential operational circuits which were designed to accomplish the following tasks: firstly, to measure the voltage of the battery cell; secondly, to gauge the charging current; and finally, to regulate the charging current. The subsequent sections elaborate on the operational principles of these three areas of the Floater device.

3.1.1 Battery Cell Voltage Measurement

The battery cell voltage measurement circuit block diagram is presented in Figure 3-3. The U^+ and U^- terminals of the battery are initially passed through RC filters before being connected to an Instrumentation Amplifier ("$IN.Amp$" in the figure). The instrumentation amplifier amplifies the difference between the inverting and non-inverting inputs while rejecting any signal common to both inputs, resulting in no common-mode component being present at the instrumentation amplifier's output.
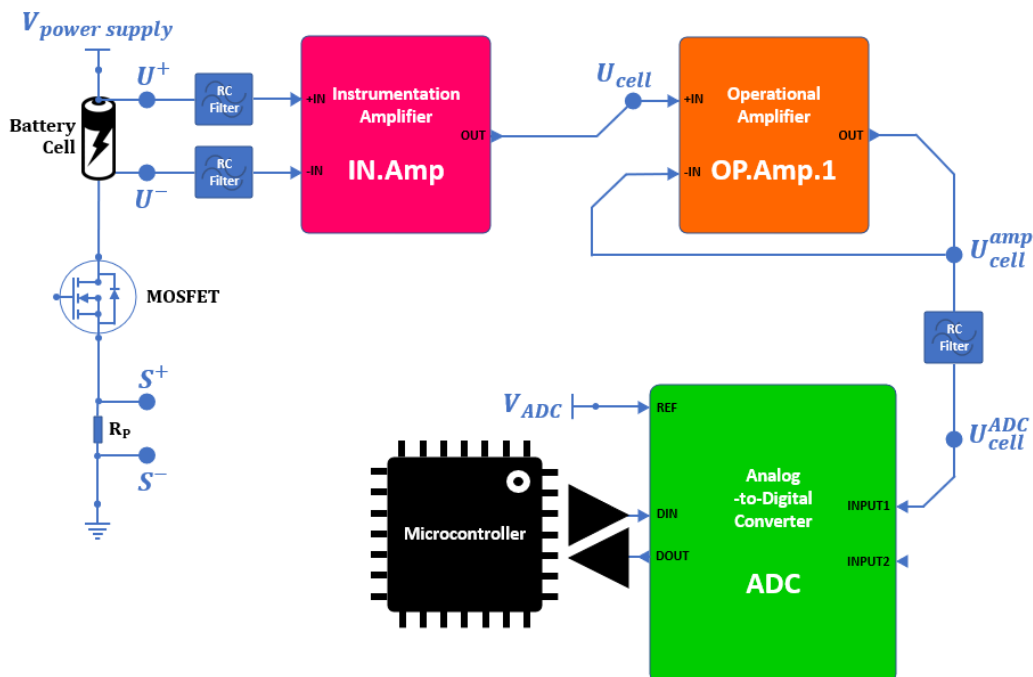
Figure 3-3: Block diagram of the cell voltage measurement circuit

The amplified output signal (U_{cell}) of the instrumentation amplifier is connected to the first input of an Operational Amplifier ("OP. Amp. 1" in the figure), with the feedback loop connected to the other input using the output signal (U_{cell}^{amp}). The output signal of the operational amplifier passes through an RC filter before being connected to an Analog-to-Digital Converter ("ADC" in the figure) as an input (U_{cell}^{ADC}). The analog-to-digital converter digitalizes the signal, and the resulting output is sent to the microcontroller. The figure demonstrates how the cell voltage value is converted into a digitized value that is transmitted to the microcontroller.

3.1.2 Battery Charging Current Measurement

The circuit block diagram presented in Figure 3-4 depicts the circuitry of the Floater device aimed at measuring the charging current. The two terminals (S^+ and S^-) of the precision resistor (R_P) are connected to the inputs of a High Precision Instrumentation Amplifier ("HP. IN. Amp" in the figure) after passing through RC filters. The output signal (U_{charg}^{ADC}) then passes through another RC filter before entering the Analog-to-Digital Converter (ADC) as an input. The digital output of the ADC is then transmitted to the microcontroller for further processing. The diagram illustrates the process of measuring the charging current and converting it into a digitized value.
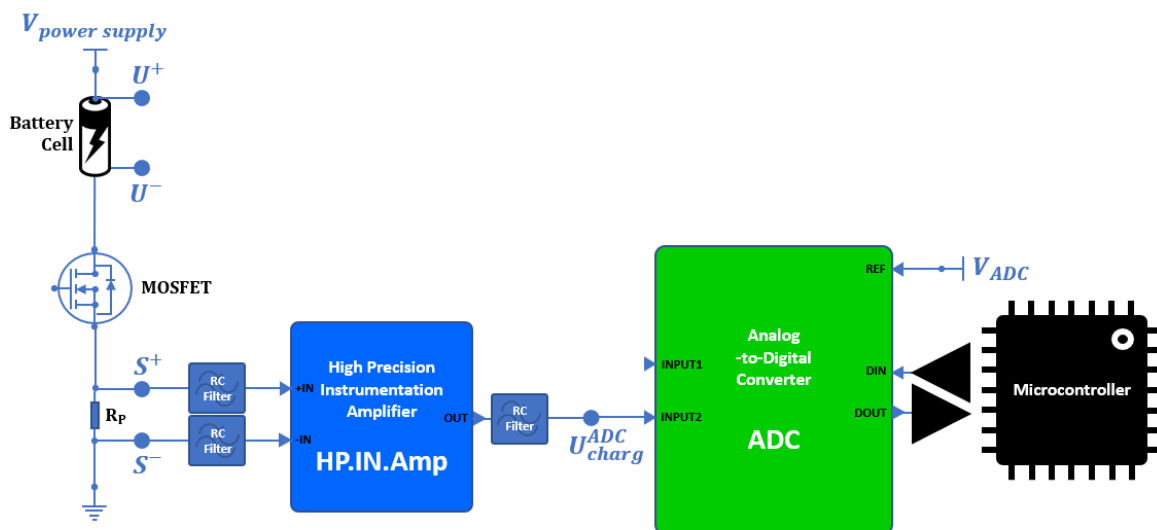
Figure 3-4: Block diagram of the charging current measurement circuit

3.1.3 Charging Current Regulation

Figure 3-5 shows the simple circuit block diagram for the regulation of the charging current. The microcontroller calculates and transmits the output signal of the

Fuzzy+PI controller ($I_{digitized}^{DAC}$) to a DAC in order to regulate the charging current. the analog output signal (I_{analog}^{DAC}) serves as one of the inputs for another Operational Amplifier ("OP. Amp. 2" in the figure). The other input signal of the DAC corresponds to the voltage on the input side of the precision resistor (S^+). The output signal of the operational amplifier (U_{gate}) is connected to the MOSFET Transistor. The operational amplifier controls U_{gate} such that the value of the S^+ signal value becomes equivalent to the the I_{analog}^{DAC} signal value. The figure illustrates the process by which the charging current is regulated and transmitted to the MOSFET transistor.
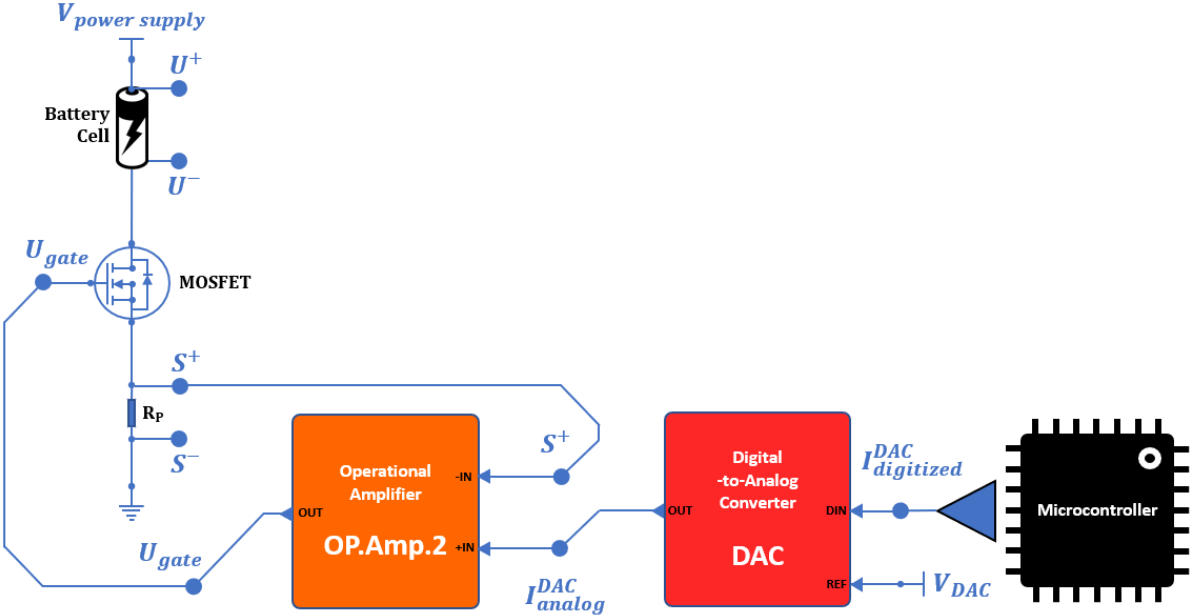
Figure 3-5: Block diagram of the charging current regulation circuit

In Figure 3-6, the overall block diagram of the Floater test device's circuitry is presented. The aforementioned three circuits measure the voltage and charging current and transmit this information to the microcontroller. Subsequently, the Fuzzy+PI controller calculates the regulatory digital signal based on voltage measurements as the input, which is fed to the circuitry. The circuitry then provides the corresponding input to the transistor to regulate the charging current as required.

With a clear understanding of the operational processes of the Floater test device, including its ability to measure cell voltage and charging current, and to regulate the latter, attention must now be turned to the design of the Fuzzy+PI controller as its objective is to ensure that the battery cell voltage is maintained at the desired level.
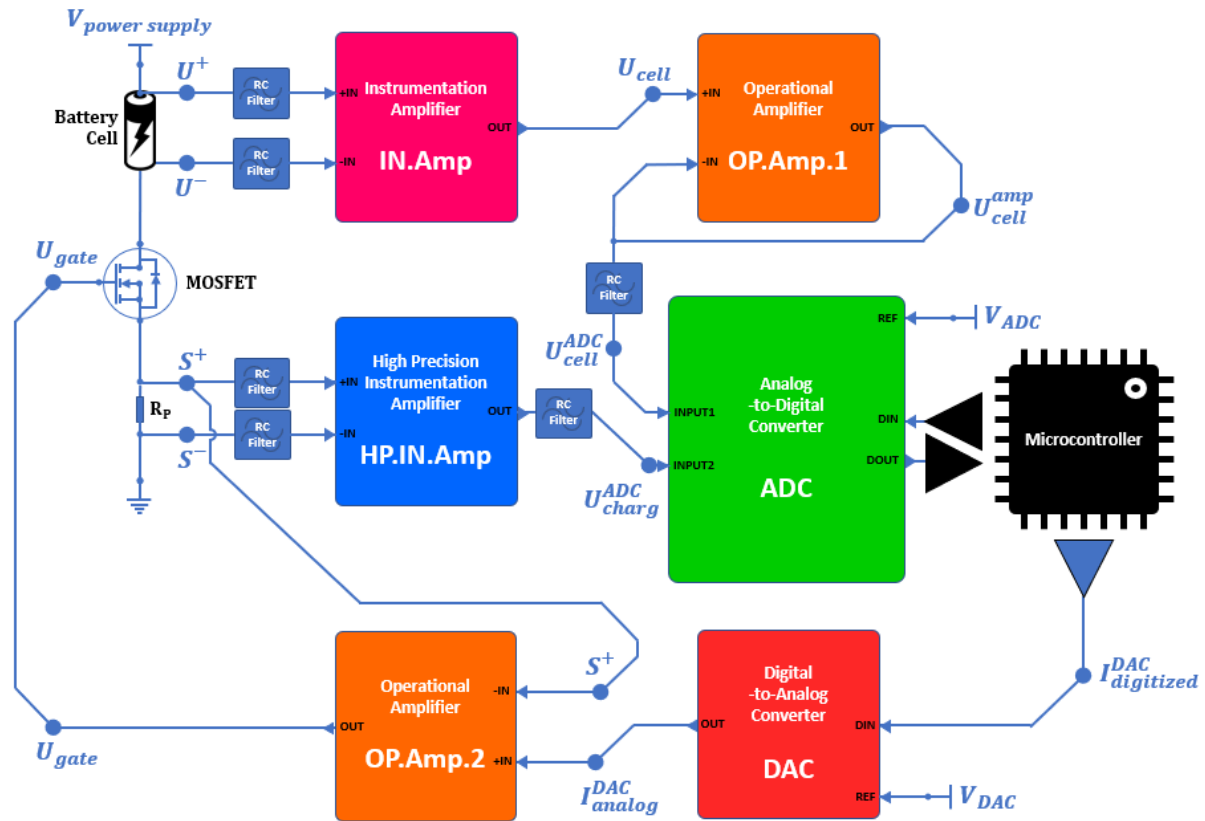
Figure 3-6: Circuitry block diagram of the Floater electronic test device

3.2   Fuzzy+PI Controller Design

Having clarified the operational principles of the Floater device, the subsequent step is to explain the process by which the regulating signal is generated by the controller to be transmitted into the Floater. In designing a control system for a particular application, choosing the appropriate control strategy is critical in achieving desired performance. The Proportional-Integral (PI) controller is a widely used control strategy due to its simplicity and effectiveness in regulating system dynamics. The PI controller is a type of feedback controller that uses both the proportional and integral gains to control the system's output. The proportional gain is responsible for producing a response proportional to the error, while the integral gain eliminates the steady-state error. As previously indicated, the Floater test device was initially equipped with a conventional PI controller, whereby the setpoint was manually assigned. The schematic of the previous configuration of the controller is depicted in Figure 3-7.
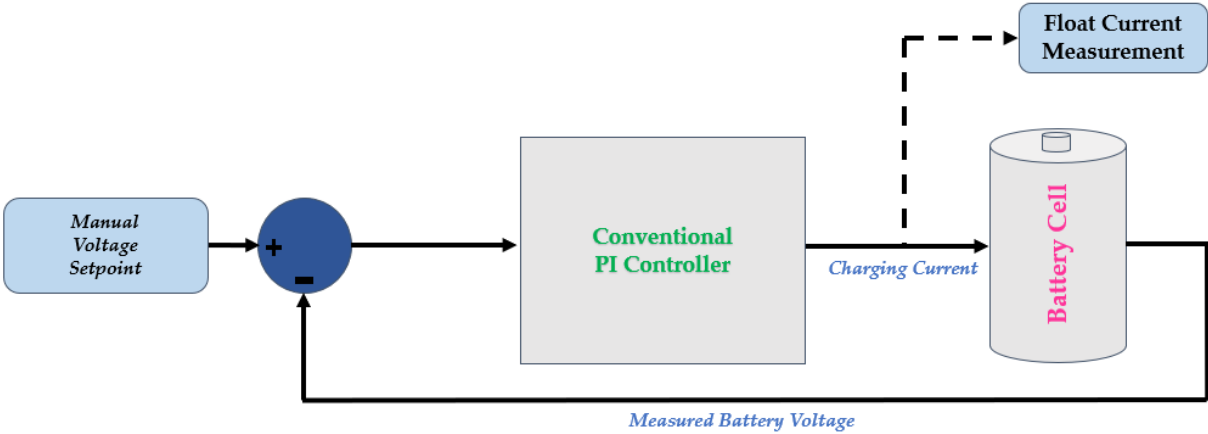
Figure 3-7: Floater's previous controller configuration: PI controller

In the initial experimental trial tests, the choice of a PI controller without a Derivative (D) term was made based on the simplicity of the control strategy and its potential effectiveness in regulating the system's output. The D term provides a control action proportional to the rate of change of the error, which can help to improve the system's response time. However, the D term can also introduce noise amplification and instability if not properly tuned. Thus, the decision to neglect the D term was based on the initial experimental trial tests as it turned out that PI controller works properly, and the D-term was not only unnecessary but also could be problematic for the controller design process and tuning the gains. Conventional PID control strategies, including the PI controller, can be difficult to tune and optimize for nonlinear systems. To address this, an intelligent self-tuning fuzzy + PI controller was utilized. As explained earlier, the fuzzy controller is a type of control strategy that uses linguistic rules and membership functions to produce a control output. The Fuzzy+PI controller combines the advantages of the fuzzy controller's adaptive control with the PI controller's efficient performance.

Additionally, the Fuzzy+PI controller does not require a model of the system under control. This is particularly advantageous for systems where obtaining a dynamic model is difficult or computationally expensive, such as in this case where the microcontroller should be handled considerably not to be imposed by high computational loads. The intelligent self-tuning capability of the Fuzzy+PI controller allows it to adjust itself in real-time based on the current state of the system. Thus, the use of a Fuzzy+PI controller in this application is justified by its ability to address the complexity of the system and the difficulty in obtaining a dynamic model. Briefly, the Fuzzy+PI controller seemed a fitting control system choice as it is not a model-based adaptive controller as well as it can be configured in a manner to avoid

too heavy computational load on the microcontroller. The schematic of the new controller configuration is illustrated in Figure 3-8.
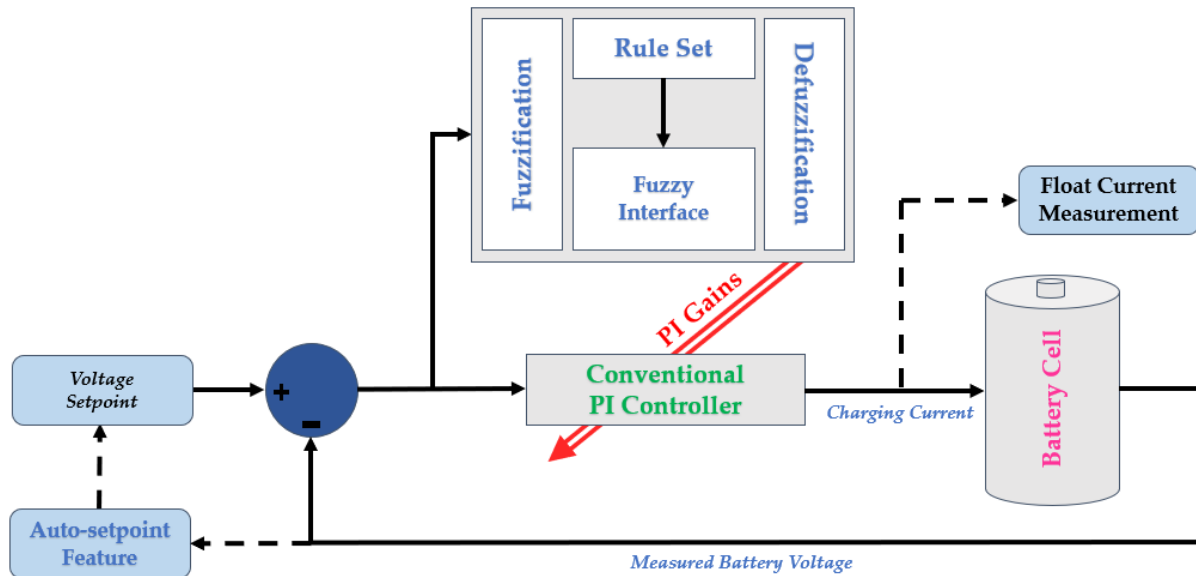
Figure 3-8: Floater's new controller configuration: Fuzzy+PI controller

In the following sections, the design procedure of a fuzzy algorithm for the Fuzzy+PI controller will be explained. The fuzzy controller in this configuration takes the error and the error change as inputs and outputs the K_P and K_I gains. The first step in designing a fuzzy algorithm for the controller was to choose the membership functions for the inputs and the outputs. The membership function describes the degree of membership of a value to a certain linguistic variable. In the case of the error and the error change, typical membership functions could be triangular, S-shaped, Z-shaped or trapezoidal, where the shape and the range of the function are determined by the characteristics of the input. Similarly, for the outputs of K_P and K_I, the membership functions could be in similar forms of triangular, S-shaped, etc.

Once the membership functions had been defined, the next step was to define the rule set. The rule set consists of a set of "if-then" statements that define the relationship between the inputs, i.e., the error and the error change, and the outputs, i.e., K_P and K_I gains of the PI controller. These rules are typically written in a linguistic format. The rule set was determined through expert knowledge as well as trial and error. Finally, the defuzzification method was chosen. Defuzzification is the process of converting the fuzzy output of the controller into a crisp value that can be used to adjust the system, in this case, the charging current. One simple and computationally efficient defuzzification method is the weighted average method, which was chosen based on the requirement to keep the computational load as low

as possible. This method provided a simple and intuitive way of determining the final output of the fuzzy controller.

Understanding the specific characteristics of the Floater is therefore essential for developing a successful controlling strategy, and any limitations or requirements of the device should be considered during the design process. An important characteristic of the Floater is that it can only operate in charging mode, and this mode is dictated by the Floater's system design. As such, it is critical to understand this specific limitation of the device to develop an effective controlling strategy. This involved selecting appropriate membership functions for the input/output signals and defining the rule set carefully to ensure that the device operates rigidly and satisfactorily.

3.2.1 Inputs/Outputs Membership Functions

In designing fuzzy controllers, selecting an appropriate membership function for the input and output variables is a crucial step that directly affects the performance of the system. Several types of membership functions are available, ranging from simple triangular and trapezoidal shapes to more complex functions such as Gaussian and Sigmoid functions. In this thesis, it was decided to use only trapezoidal and triangular membership functions (along with its variations, i.e., S-shaped and Z-shaped membership functions). This decision was based on the fact that these types of functions require less calculations and computational load than more complex functions, making them more computationally efficient. In addition, these simple functions can be easily understood and interpreted by system operators, which is important in developing effective and practical control strategies. While more complex functions may offer some advantages in certain applications, the simplicity and efficiency of trapezoidal and triangular membership functions make them a reasonable choice for this specific fuzzy control system.

The development of a successful fuzzy control system often involves a process of trial and error, in which different membership functions and parameters are tested and evaluated to determine their effectiveness. In this thesis, after many iterations of testing, a set of membership functions and thresholds were selected for the error and error change inputs, as well as for the K_P and K_I outputs. The following three tables are presented to document the membership functions used for the inputs and the outputs. These tables provide clear and concise information on the membership function types and their corresponding thresholds. Table 3-1 outlines the specific membership functions chosen for the input error, Table 3-2 for the input error change, and Table 3-3 for both outputs K_P and K_I gains (sharing similar membership functions).

MFs	Abbreviation for	MF Type	Parameters
NB	*Negative Big*	Z-shaped	$a = -0.001$ $b = -0.0001$
NS	*Negative Small*	Triangular	$a = -0.001$ $b = -0.0001$ $c = 0$
ZO	*Zero*	Triangular	$a = -0.0001$ $b = 0$ $c = 0.0001$
PS	*Positive Small*	Triangular	$a = 0$ $b = 0.0001$ $c = 0.001$
PB	*Positive Big*	S-shaped	$a = 0.0001$ $b = 0.001$

Table 3-1: Membership functions specifications of the error (1st input)
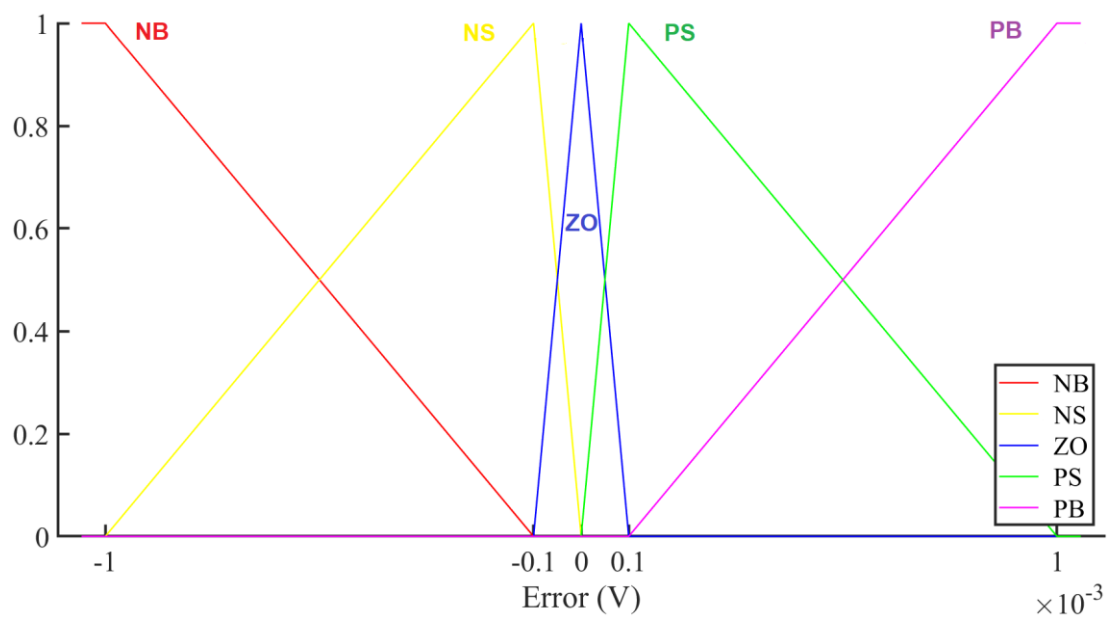
Figure 3-9: Membership functions of the error (1st input)

MFs	Abbreviation for	MF Type	Parameters
N	*Negative*	Z-shaped	$a = -0.0011$ $b = -0.0009$
Z	*Zero*	Trapezoidal	$a = -0.0011$ $b = -0.0009$ $c = 0.0009$ $d = 0.0011$
P	*Positive*	S-shaped	$a = 0.0009$ $b = 0.0011$

Table 3-2: Membership functions specifications of the error change (2nd input)
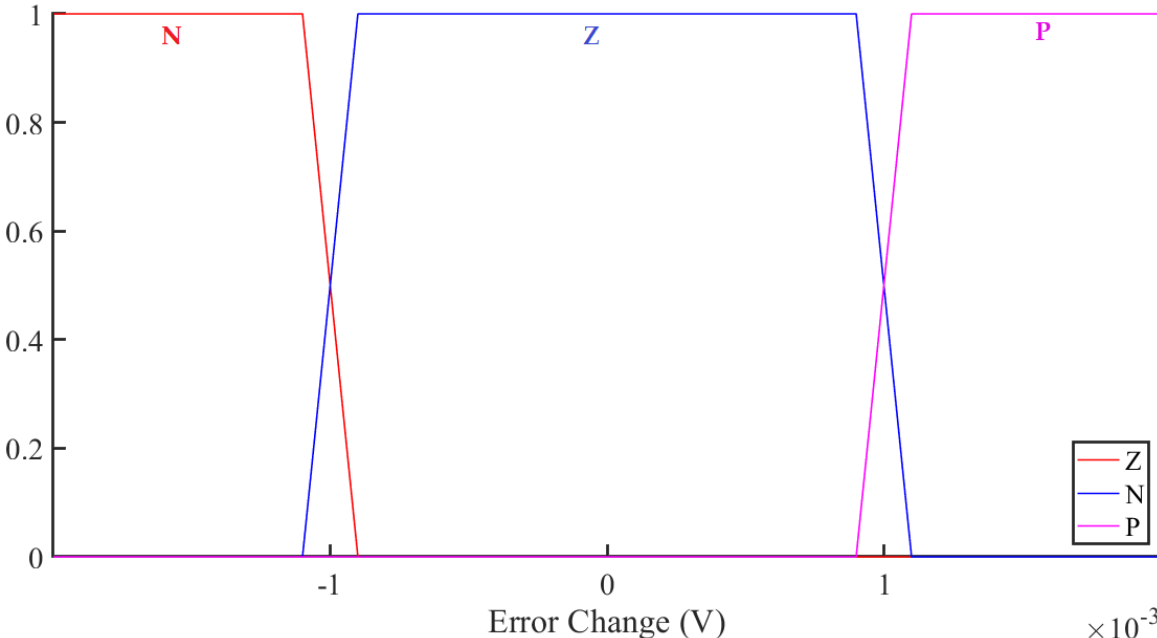
Figure 3-10: Membership functions of the error change (2nd input)

MFs	Abbreviation for	MF Type	Parameters
Z	*Zero*	Z-shaped	$a = 0$ $b = 0.3$
S	*Small*	Triangular	$a = 0$ $b = 0.3$ $c = 0.5$
M	*Medium*	Triangular	$a = 0.3$ $b = 0.5$ $c = 0.7$
L	*Large*	Triangular	$a = 0.5$ $b = 0.7$ $c = 1$
B	*Big*	S-shaped	$a = 0.7$ $b = 1$

Table 3-3: Membership functions specifications of K_P and K_I gains (outputs)
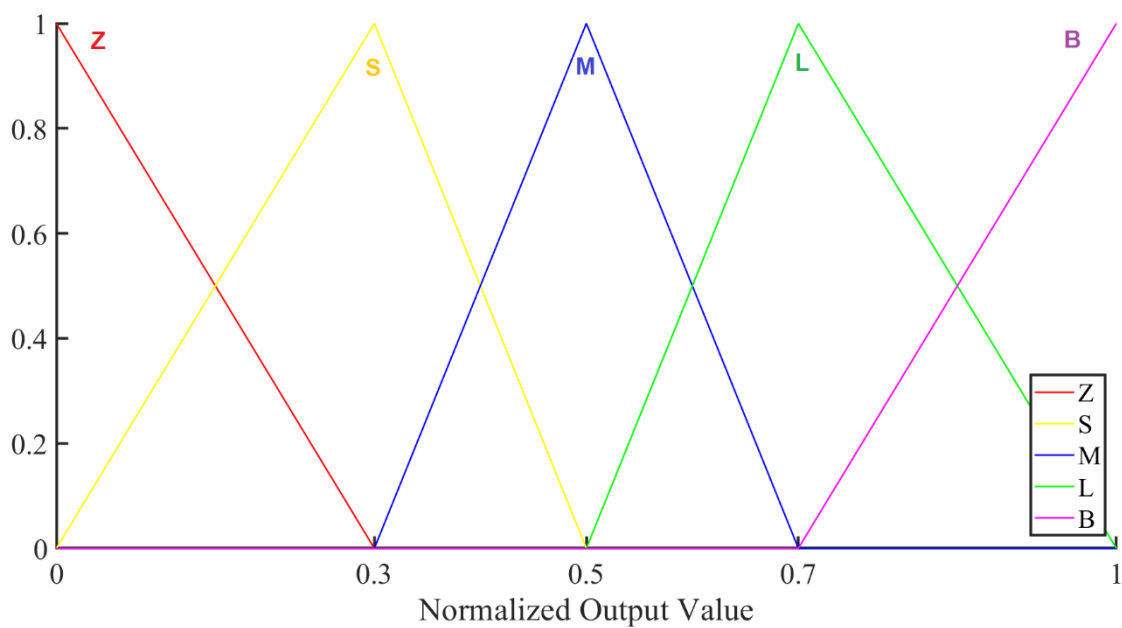
Figure 3-11: Membership functions of K_P and K_I gains (outputs)

The specific membership functions and thresholds introduced in the tables are shown in Figure 3-9 for the error as the first input, Figure 3-10 for the error change as the second input, and Figure 3-11 for the K_P and K_I gains as the outputs. These functions were chosen based on their ability to accurately represent the system behavior and respond to changes in input signals, while minimizing computational load and avoiding unnecessary complexity. The final selection of membership functions and thresholds reflects a balance between computational efficiency and system performance, and is the result of numerous testing iterations and evaluation process.

It is important to note that the K_P and K_I gains generated by the fuzzy control system are normalized values within the range of [0,1]. This means that a denormalization step is necessary to convert these normalized gains into their corresponding physical values. To achieve this, two threshold values are introduced for each output to define the minimum and maximum values of K_P and K_I gains, which are used to scale the normalized gains to their appropriate physical values. Specifically, two parameters are set for each output variable, representing the maximum values for K_P and K_I, and a low boundary values expressed as a percentage of their respective maximums. This process ensures that the gains generated by the fuzzy control system are within the acceptable range for the physical system being controlled. The use of normalized gains and the subsequent denormalization step is a common practice in fuzzy control systems, and is an important consideration when designing and implementing such systems.

3.2.2 Rule Set

The other critical aspect of designing a fuzzy control system is defining the rule set that governs the system's behavior. The rule set defines how the system maps inputs to outputs and represents the knowledge base that underlies the fuzzy control system. In the present study, since the system has two outputs, namely K_P and K_I gains, a fuzzy rule set in the form of two different charts were developed (one for each output). Each chart was structured as a 5 by 3 linguistic matrix, with 15 elements in total for each chart, reflecting the five membership functions of the first input, the error, and the three membership functions of the second input, the error change. Defining the rule set in this manner aimed to capture the complexity of the system's behavior while keeping the rule set manageable and easy to understand.

The resulting fuzzy logic rule set for the electronic test equipment is presented in Table 3-4 and Table 3-5, which depict the membership functions and corresponding output values for the K_P and K_I gains, respectively. The tables provide a clear and concise representation of the rule set, making it easy to interpret and reproduce. By

presenting the rule set in this structured manner, a comprehensive and transparent overview of the control system's behavior is provided.

K_P		Error				
		NB	*NS*	*ZO*	*PS*	*PB*
Error Change	*N*	Z	S	S	M	L
	Z	Z	S	S	M	L
	P	Z	S	S	M	B

Table 3-4: The rule set chart for K_P output

K_I		Error				
		NB	*NS*	*ZO*	*PS*	*PB*
Error Change	*N*	Z	Z	S	S	M
	Z	Z	S	S	M	L
	P	S	S	M	L	B

Table 3-5: The rule chart set for K_I output

Figure 3-12 displays the fuzzy control surface for the K_P output, depicting its variation in response to changes in the input variables based on the rule set for the respective output. Similarly, Figure 3-13 presents the corresponding 3D graph for the K_I output, providing an additional perspective on the system's behavior. These graphs provide a visual representation of the control system's response to different

input combinations, aiding in the understanding and optimization of the system's behavior.
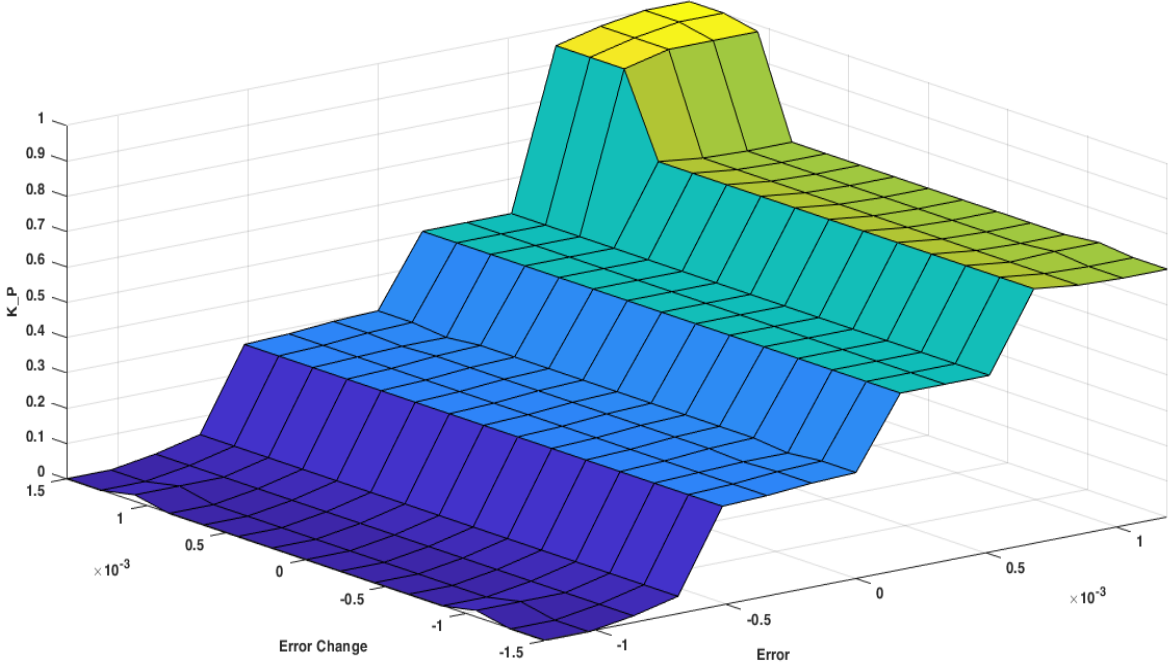
Figure 3-12: Fuzzy control surface for K_P output
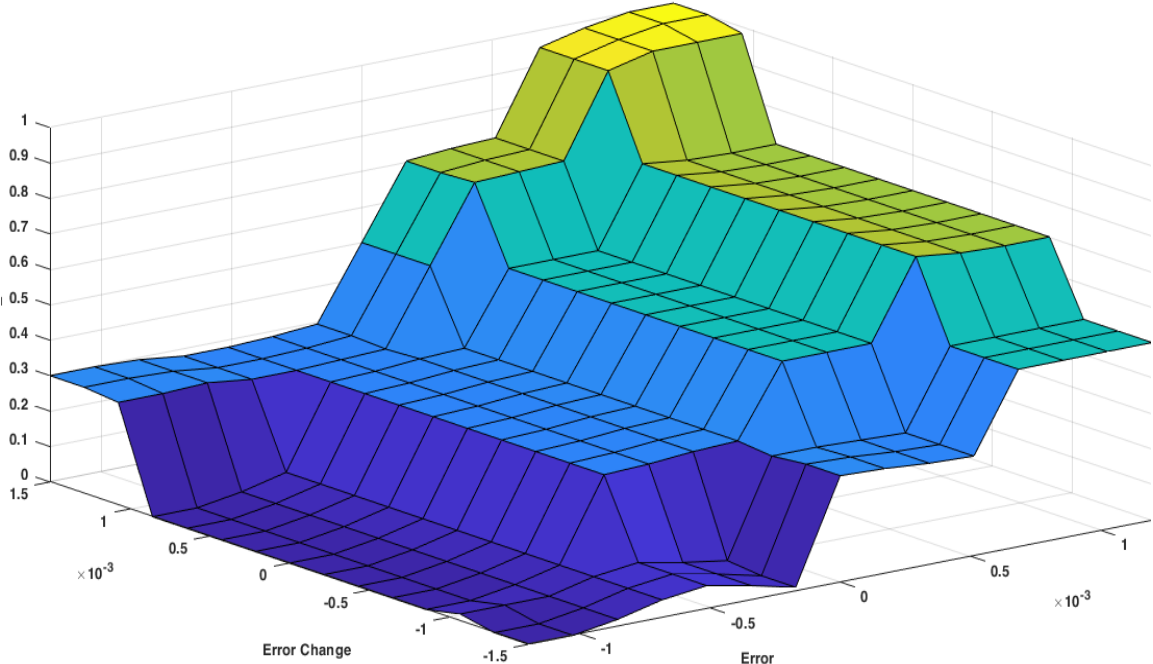
Figure 3-13: Fuzzy control surface for K_I output
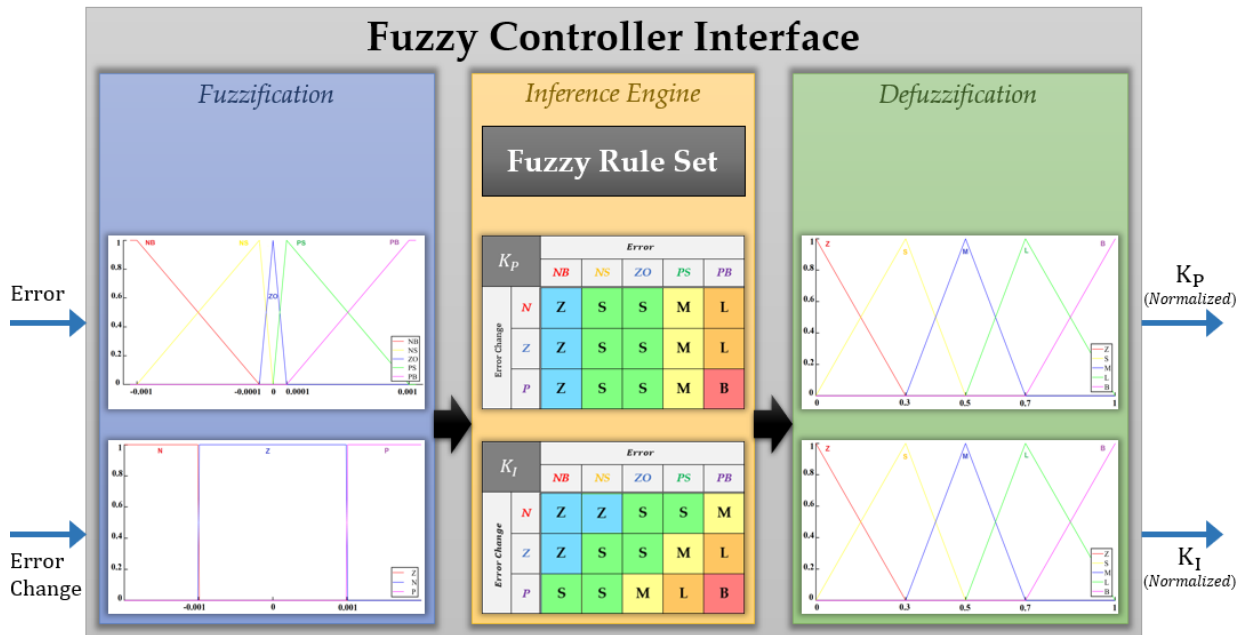
Figure 3-14: Structure of fuzzy controller

Figure 3-14 shows the structure of the fuzzy controller with details, such as inputs, outputs, their respective membership functions, rule sets, etc. Following the design and development of the fuzzy logic controller, the next crucial step was to convert the algorithm into executable code for the microcontroller using the C++ programming language. This process involved translating the algorithm's rules and membership functions into code, defining the inputs and outputs, performing defuzzification, incorporating denormalization, etc.

Once the code was written, it was tested and debugged before being uploaded onto the Floater device using a Raspberry-Pi 3 computer module. This step was essential to ensure that the fuzzy controller was properly integrated into the Floater's electronic systems, and that the code was capable of accurately controlling the system in real-time. With the code implemented, the final stage of the project involved experimental testing of the fuzzy control system's performance to evaluate the controller's ability to maintain stable and accurate control of the system.

3.3   Experimental Tests

The experimental tests for the float current analysis were conducted using the Floater device. The setup for the experiment consisted of the Floater device, one or more battery cells, a power supply module, a Raspberry-Pi 3 computer module, and a desktop computer. Figure 3-15 shows the initial experimental setup where the trial

tests were being conducted in the ambient temperature (i.e., there was no control over the temperature). The main experimental tests were performed in the laboratory where the battery cell(s) contained inside an oven to run the tests under specified ambient temperature.
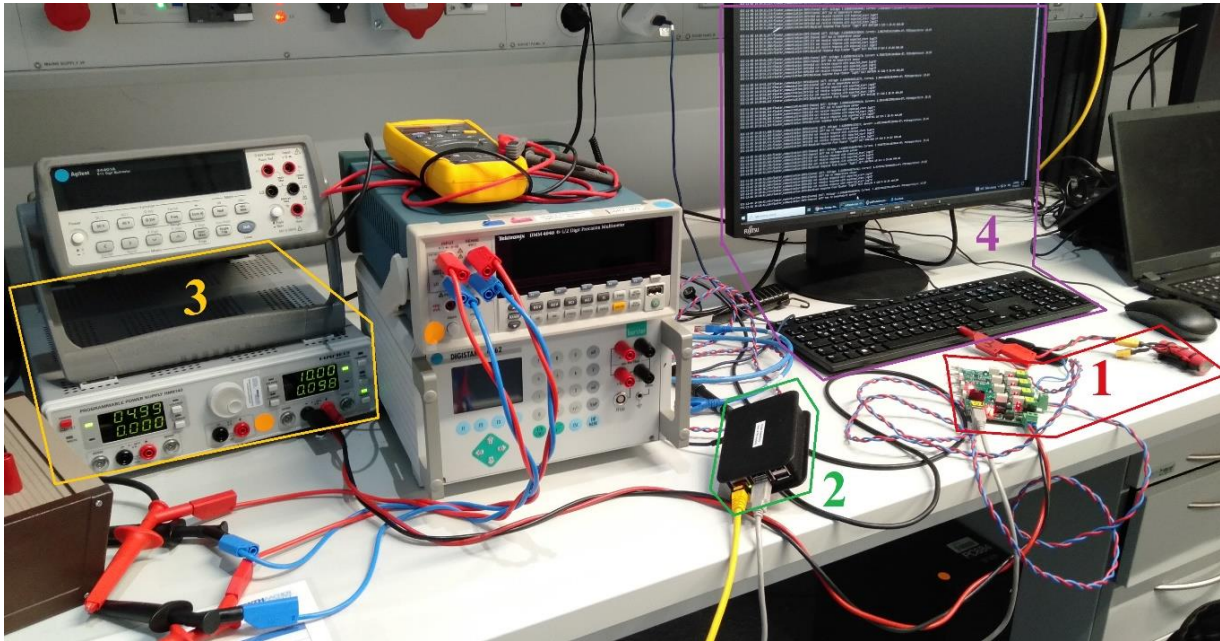
Figure 3-15: Experimental test setup comprising: (1) Floater and battery cell, (2) Raspberry-Pi 3 computer module, (3) power supply, and (4) desktop computer

Before starting the experimental tests, adjustments were made to the preset parameters, such as the operating mode of each of the four battery slots, the maximum range of K_P and K_I, and the setpoint voltage. The setpoint voltage could be set to zero for activating the auto-setpoint feature or a non-zero value for appointing a manual setpoint. Once the parameters were set, the battery cell was connected to the Floater, and the test was started.

During the experimental tests, the performance of the fuzzy controller algorithm was evaluated. The results of the test were logged, including the charging current (which is called the float current in the steady-state region) and the battery voltage. The recorded data was logged in CSV file format to be subsequently analyzed to determine the effectiveness of the fuzzy controller algorithm in regulating the charging current while keeping the cell voltage constant. Figure 3-16 shows the Floater connections to the Raspberry-Pi 3, the power supply, and the battery cell.
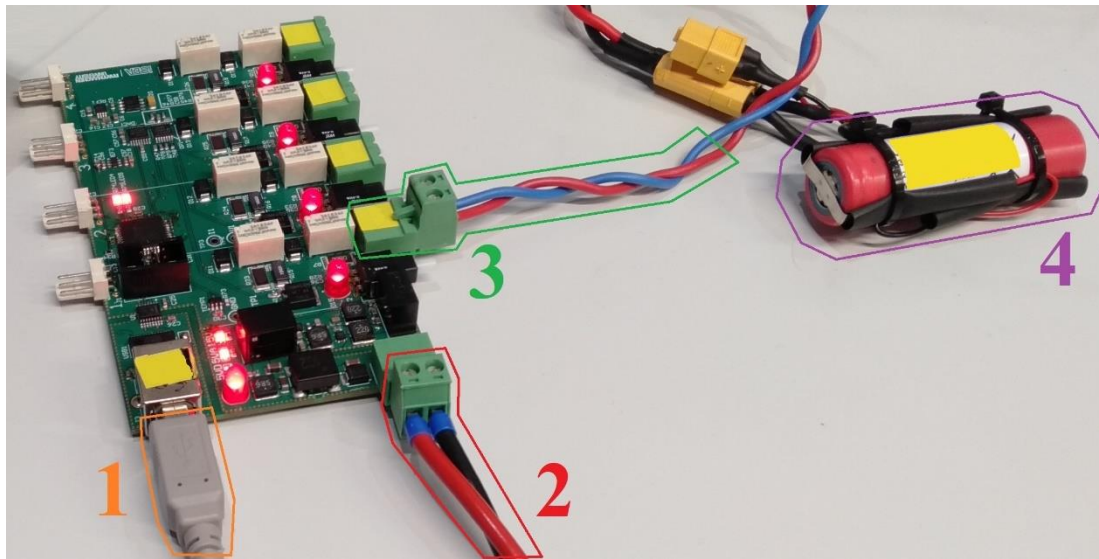
Figure 3-16: Floater's connections to: (1) Raspberry-Pi 3, (2) power supply, and (3) battery cell, and (4) the cylindrical lithium-ion battery cell itself

4. Results and Discussion

In the previous chapter, the steps taken to complete the project and carry out the experimental tests have been outlined. In this chapter, the results obtained from these tests will be presented. The evaluation of the results will be conducted in two areas. The first area is the performance of the Fuzzy+PI controller, which will be compared with the results of the conventional PI controller. The second area is the impact of the auto-setpoint feature on the duration of the experimental tests. The results obtained from the tests conducted using the auto-setpoint feature will be compared with those obtained from the tests conducted with the manual setpoint setting. The results of this analysis will provide insights into the effectiveness of the Fuzzy+PI controller and the auto-setpoint feature in improving the performance and reducing the testing time for the Floater device.

4.1 Fuzzy+PI controller vs. Conventional PI controller

In this section, the test results of the newly developed self-tuning Fuzzy+PI controller will be compared to those obtained from the previously used conventional PI controller. The voltage readings and the corresponding charging currents obtained from both controllers will be analyzed and compared in terms of their standard deviations. Additionally, the time required for manual tuning of the conventional PI controller will be discussed, and the benefits of eliminating this time-consuming step through the use of the self-tuning controller will be highlighted. The aim of this comparison is to evaluate the effectiveness of the new self-tuning controller in achieving more accurate and reliable results while reducing the overall testing time and effort.

In order to compare the performance of the conventional PI controller with manual setpoint assigning and the new Fuzzy+PI controller with the auto-setpoint feature, four experimental tests were conducted on two different types of battery cells. The first two tests were performed using the conventional PI controller with manual

tuning, where the setpoint was appointed manually by measuring the initial voltages of the battery cells. The setpoint values were chosen to be very close to the measured voltages, with initial errors ranging from 2 to 3 mV. The other two tests were conducted using the Fuzzy+PI controller with the auto-setpoint feature on the same battery cells. All four tests were carried out in a thermal oven to maintain a constant temperature of 25°C throughout the duration of the tests, which were run for 24 hours.

The purpose of conducting these tests was to compare the voltage readings and charging currents of the two types of controllers in terms of standard deviations. Additionally, the time required for manual tuning of the conventional PI controller and the elimination of this time-consuming step through the self-tuning feature of the Fuzzy+PI controller will also be discussed. Comparing the results of these four tests aimed to provide insights into the performance of the two controllers and the impact of the new auto-setpoint feature on the test results.

As previously mentioned, experimental tests were conducted on two distinct types of lithium-ion battery cells. The test parameters for all four experimental tests are presented in Table 4-1.

#	Test Type	Setpoint Setting Mode	Temp.	Initial Voltage	Setpoint Voltage	Initial Error
1	**Conventional PI with LIB type A**	*Manual*	25°C	3.66100 V	3.664 V	**3000 μV**
2	**Conventional PI with LIB type B**	*Manual*	25°C	3.64300 V	3.645 V	**2000 μV**
3	**Fuzzy+PI with LIB type A**	*Auto-setpoint feature*	25°C	3.66518 V	3.6652 V	**20 μV**
4	**Fuzzy+PI with LIB type B**	*Auto-setpoint feature*	25°C	3.64658 V	3.6466 V	**20 μV**

Table 4-1: Test parameters for the experimental tests

The subsequent figures present the data recordings on the charging current, voltages, and corresponding error values (where error is defined as the difference between the setpoint voltage and the measured voltage.)
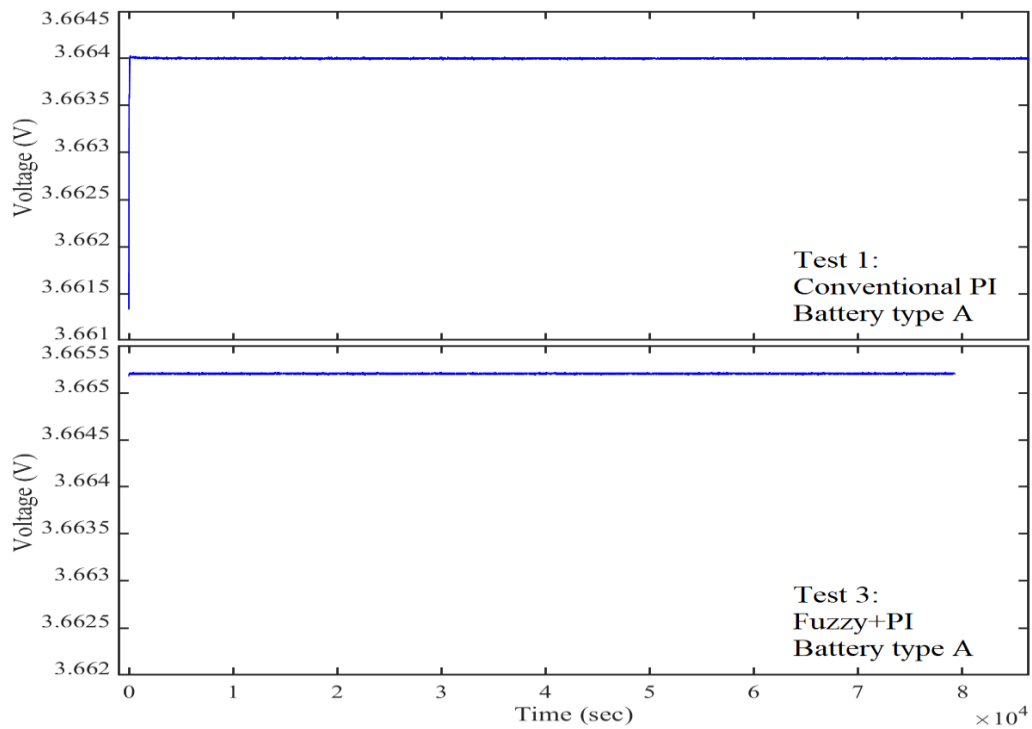
Figure 4-1: Voltage readings for Test 1 (PI / LIB:A) and Test 3 (Fuzzy+PI / LIB:A)
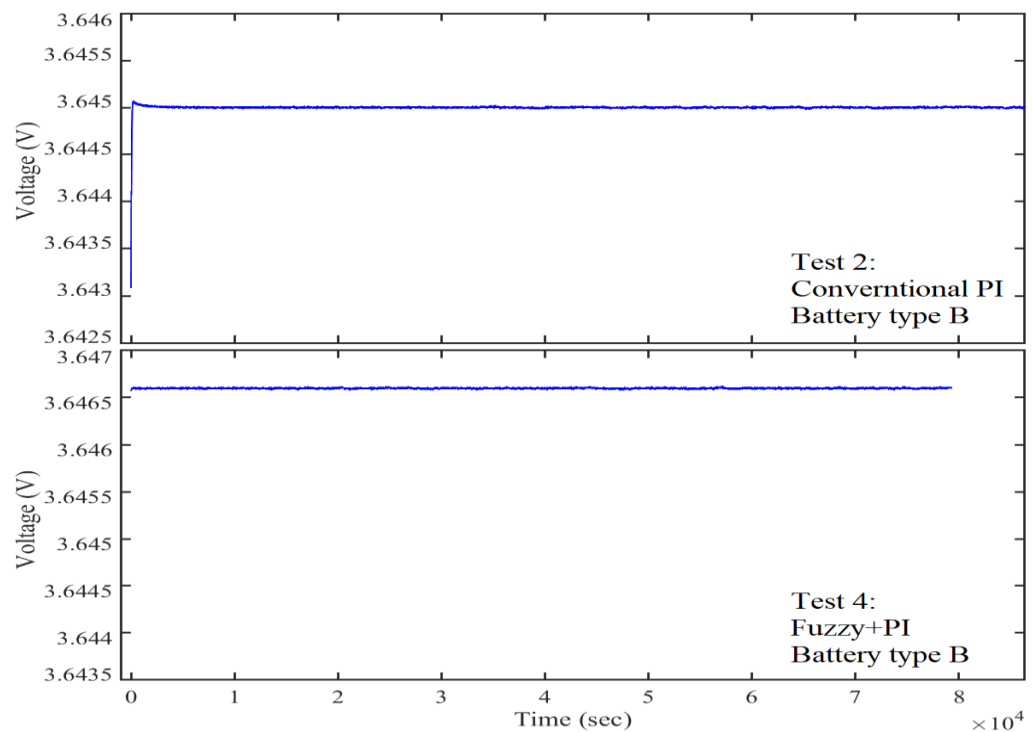
Figure 4-2: Voltage readings for Test 2 (PI / LIB:B) and Test 4 (Fuzzy+PI / LIB:B)
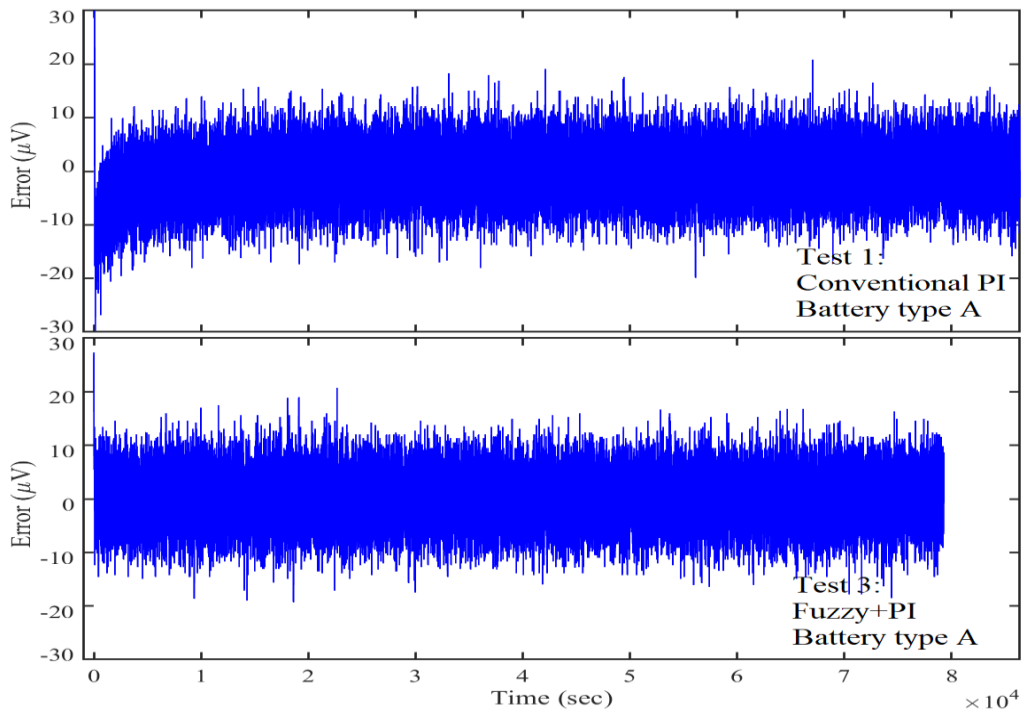
Figure 4-3: Error values for Test 1 (PI / LIB:A) and Test 3 (Fuzzy+PI / LIB:A)
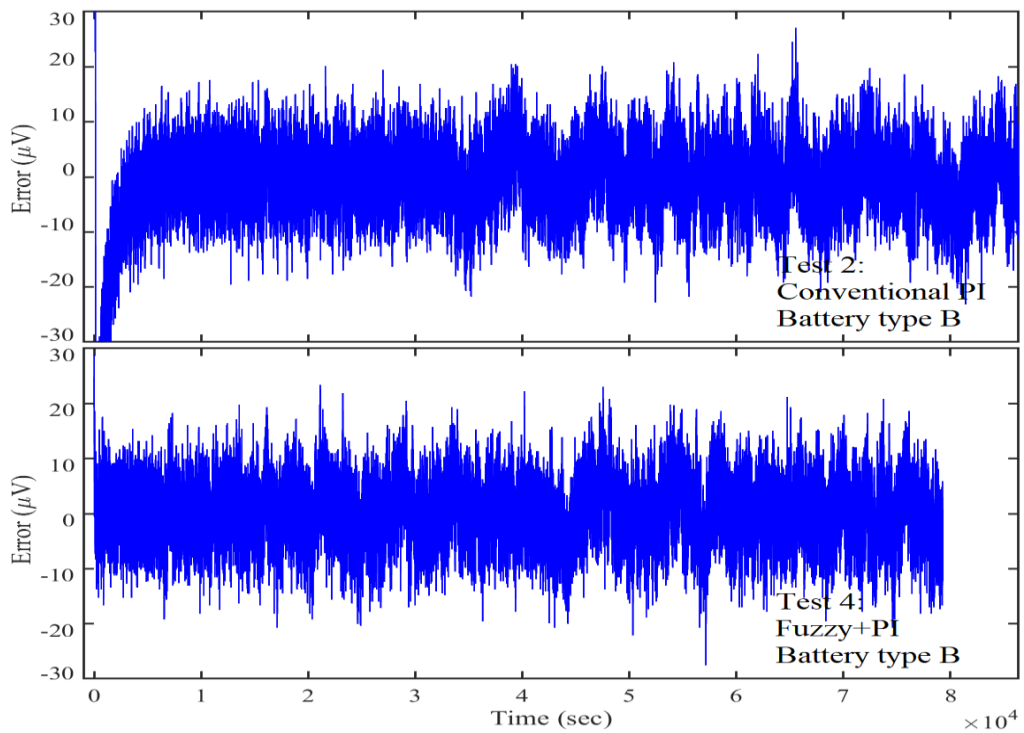
Figure 4-4: Error values for Test 2 (PI / LIB:B) and Test 4 (Fuzzy+PI / LIB:B)
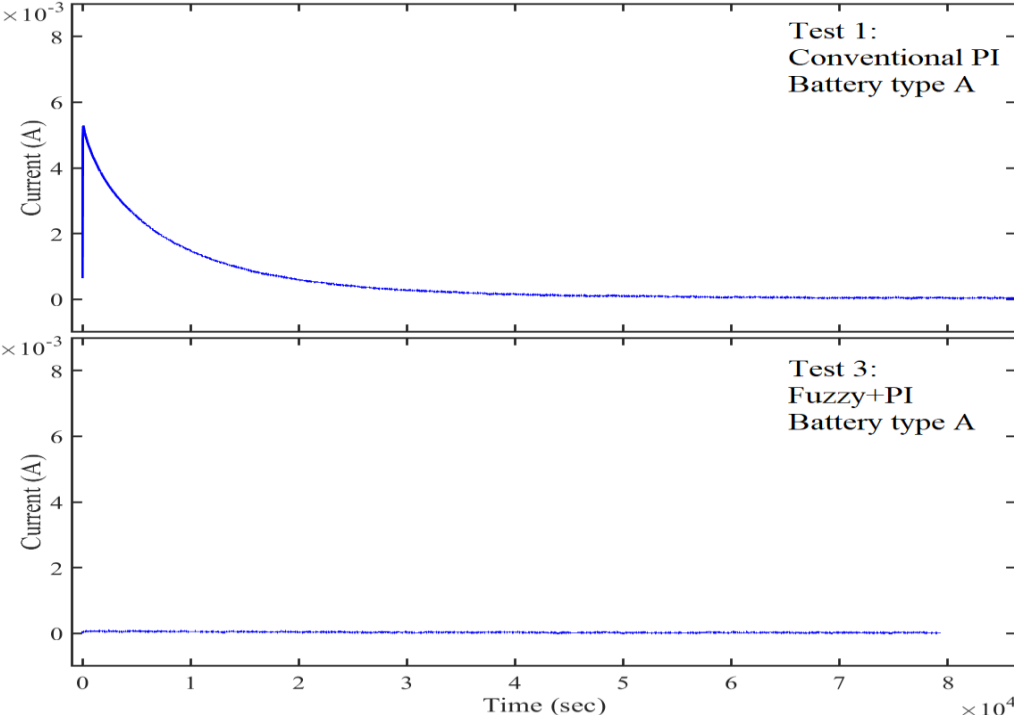
Figure 4-5: Current readings for Test 1 (PI / LIB:A) and Test 3 (Fuzzy+PI / LIB:A)
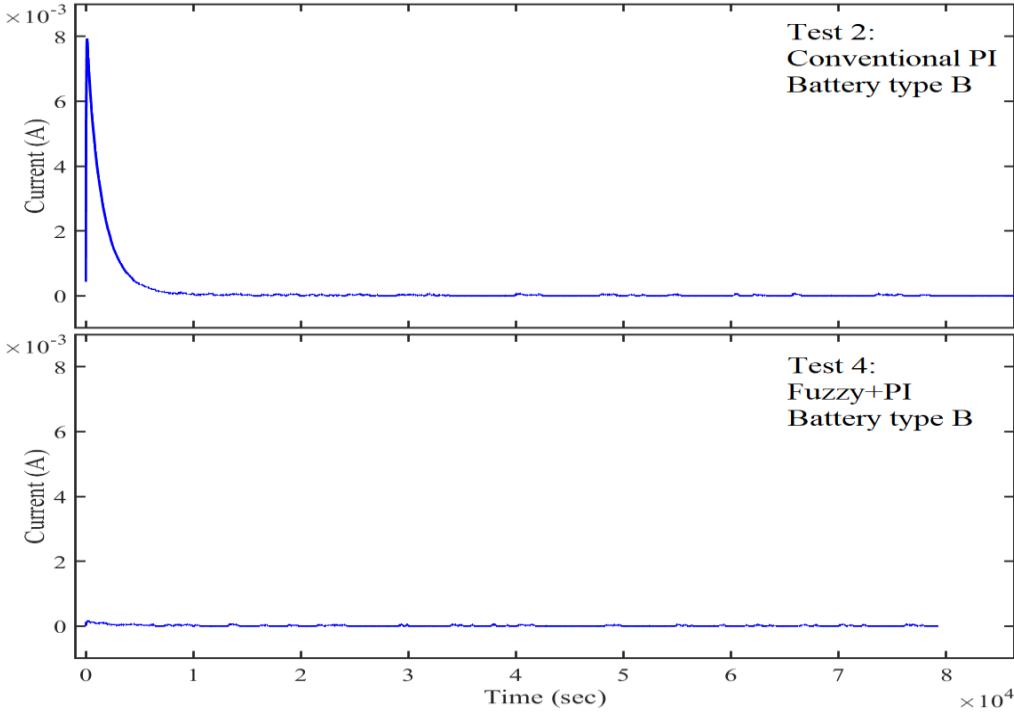
Figure 4-6: Current readings for Test 2 (PI / LIB:B) and Test 4 (Fuzzy+PI / LIB:B)

One striking observation is the impact of manually appointed setpoints on the charging current. While the initial errors in the range 2 to 3 mV may seem very small, in the upper plots of Figure 4-5 and Figure 4-6 (Test 1 and Test 3), the charging current initially increases to high values then decreases to overcome the transient phase. In contrast, in the lower plots of Figure 4-5 and Figure 4-6 (Test 2 and Test 4), the charging currents are almost within the steady-state region because of the auto-setpoint feature, which maintains a smaller initial error of 20 µV. The impact of the auto-setpoint feature will be elaborated on further in the subsequent section.

To compare the performance of the two controllers, the standard deviation in the readings was used as a metric. For voltage readings, the comparison was straightforward by neglecting the first few hours to eliminate the effect of higher initial errors for the conventional PI controller with manual setpoint. However, a direct comparison between the charging current readings was not fair due to decreasing trends in tests 1 and 3. To address this issue, a low-pass filter was applied to the charging current readings to obtain their mean curve, which was then subtracted from the charging current readings to phase out the effect of the decreasing trend (similar to applying a high-pass filter). By doing so, a more fair and authentic comparison was possible, and then the standard deviations were compared. The following figures illustrate the procedure of eliminating the impact of decreasing trends in the charging current readings.
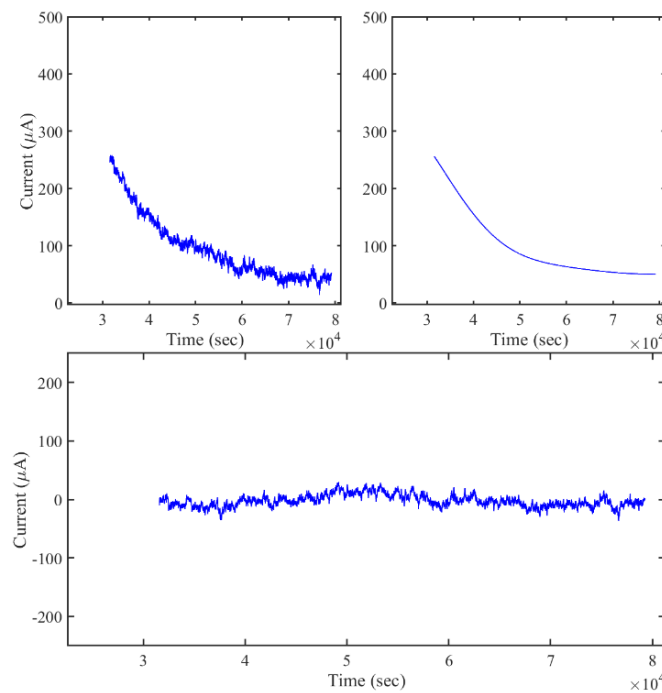
Figure 4-7: Eliminating the impact of decreasing trend for Test 1 (PI / LIB:A)
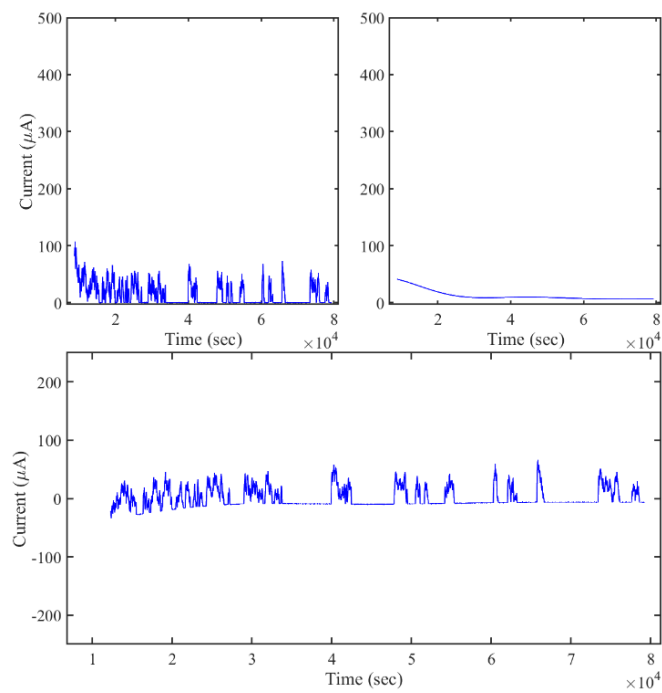
Figure 4-8: Eliminating the impact of decreasing trend for Test 2 (PI / LIB:B)
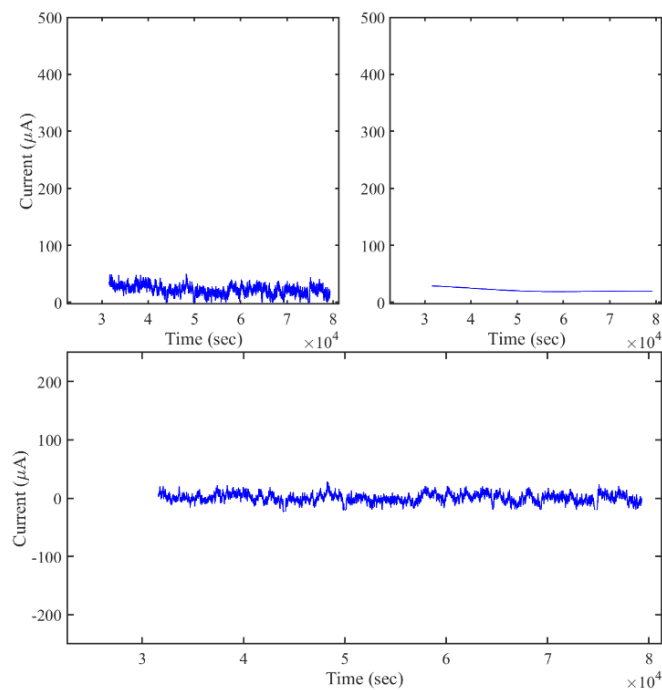
Figure 4-9: Eliminating the impact of decreasing trend for Test 3 (Fuzzy+PI / LIB:A)
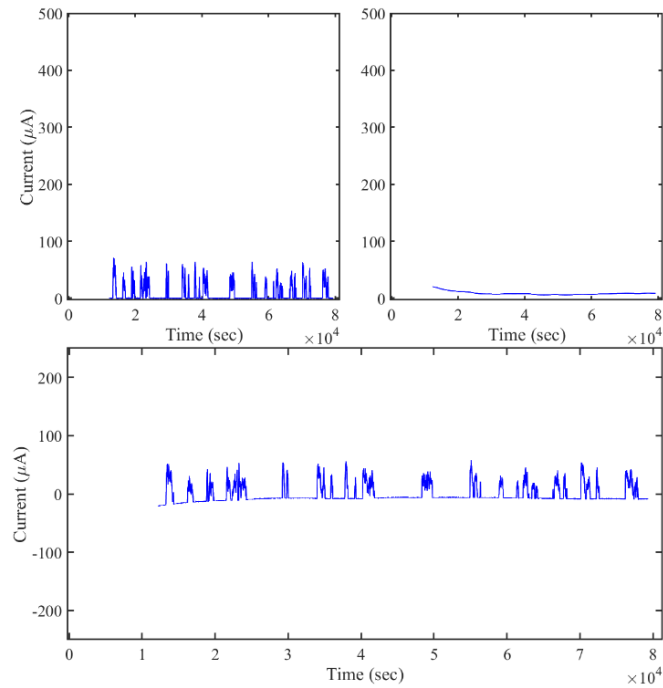
Figure 4-10: Eliminating the impact of decreasing trend for Test 4 (Fuzzy+PI / LIB:B)

#	Test Type	Voltage Std.	Variation	Error Min/Max	Maximum Error Range	Variation
1	Conventional PI Battery type A	4.5601 μV	**almost zero** *(-0.19%)*	-19.89 / 20.86 μV	40.75 μV	**-13.40%**
3	Fuzzy+PI Battery type A	4.5516 μV		-18.57 / 16.72 μV	35.29 μV	
Data in the first approx. 9 hours is neglected in which the current was in transient phase						
2	Conventional PI Battery type B	5.6124 μV	**almost zero** *(+0.29%)*	-23.18 / 27.03 μV	50.21 μV	**almost zero** *(+1.45%)*
4	Fuzzy+PI Battery type B	5.6287 μV		-27.59 / 23.35 μV	50.94 μV	
Data in the first approx. 4 hours is neglected in which the current was in transient phase						

Table 4-2: Performance comparisons for voltage and corresponding error readings of controllers for two types of batteries under testing in terms of standard deviation

#	Test Type	Current Std.	Variation
1	Conventional PI Battery type A	10.2889 µA	**-25.18%**
3	Fuzzy+PI Battery type A	7.6981 µA	
Data in the first approx. 9 hours is neglected in which the current was in transient phase			
2	Conventional PI Battery type B	15.5213 µA	**-10.83%**
4	Fuzzy+PI Battery type B	13.8406 µA	
Data in the first approx. 4 hours is neglected in which the current was in transient phase			

Table 4-3: Performance comparisons for charging current readings of controllers for two types of batteries under testing in terms of standard deviation

Table 4-2 and Table 4-3 compare the performance of conventional PI and Fuzzy+PI controllers in regulating the charging currents of lithium-ion batteries. The comparisons were conducted based on the battery cell type, as shown in both tables. The results in Table 4-2 indicate that the voltage control performance of both controllers was almost identical, with a difference of approximately 1% in the standard deviations of the voltage readings and the maximum range of error fluctuations, except for tests conducted on battery type A, where the maximum range of fluctuation was found to have improved by 13.4%.

In contrast, the analysis of Table 4-3 indicates a significant difference in the standard deviations of the charging current readings between the two controllers. Specifically, the Fuzzy+PI controller outperformed the conventional PI controller in regulating charging current for battery types A and B, improving the standard deviation by 25.18% and 10.83%, respectively. The results are especially relevant as fluctuations in charging current readings are essential to measure accurately in the experimental tests. Thus, the improvement in charging current regulation by the Fuzzy+PI controller is of considerable importance, as it helps reduce the fluctuations in the readings, leading not only to more precise results in float current analysis, but also to

reduce test time durations in order to gain the same amount of required adequate data stream.

Another notable advantage of the new Fuzzy+PI controller over the conventional PI controller is the elimination of the manual effort required to tune the controller gains for each battery cell being tested. Tuning the controller gains manually is a time-consuming process and can be highly tedious, as it often involves a trial-and-error approach. Typically, the tuning process for a battery cell requires at least three trials, each lasting between 4 to 8 hours. The laborious and time-intensive nature of this process becomes more pronounced when planning to test a high number of battery cell types. However, the new Fuzzy+PI controller eliminates the need for such a tuning step, resulting in significant savings in time, effort, and costs. This feature significantly streamlines the process of testing multiple battery cell types, which is highly critical in the context of float current analysis.

4.2   Auto-Setpoint Feature

This section aims to analyze the impact of the auto-setpoint feature and its advantages in the float current analysis tests on lithium-ion battery cells. The importance of setting an accurate initial error, even at the scale of a few millivolts, cannot be overemphasized, as it has a significant impact on the duration of the test. The longer the test, the higher the cost, time, and effort required to obtain useful data on the charging current, or the so-called float current in the steady-state phase. Manual voltage measurement using a multimeter to define the voltage setpoint on each battery cell is a tedious procedure and the tests can take a large amount of time to overcome the transient phase and reach the steady-state region, given the typical measurement range of a multimeter on voltage reading in the scale of microvolts.

Therefore, the capability of the Floater to self-define the voltage setpoint can bring about enormous cost, time, and effort savings. The auto-setpoint feature eliminates the need for manual effort to assign the voltage setpoint on each battery cell, which makes the testing process much longer. This feature enables the Floater to set the voltage setpoint automatically, which can lead to a far smaller initial error (in the range of microvolt instead of millivolt). As shown in the lower plots of Figure 4-5 and Figure 4-6 (Test 2 and Test 4), the charging currents could reach the steady-state region much sooner, even in a couple of minutes. Consequently, the auto-setpoint feature can greatly reduce the duration of the test, and more useful data can be obtained in a shorter time period, resulting in a considerable cost, time, and effort savings.

By examining Figure 4-5 and Figure 4-6, the general pattern of charging current behavior can be seen. To assess the effect of the auto-setpoint feature compared to the manual setpoint mode, the duration required for the charging current to decrease below certain values could be considered as the criterion. Table 4-4 displays these time periods for when the charging current for the first time drops below 1000 µA, 500 µA, 100 µA, and 50 µA for all four tests.

#	Test Type	Initial Error	Required time for current to once drop below			
			1000 µA	500 µA	100 µA	50 µA
1	Conventional PI Battery type A	*3000 µV*	3h : 55m	6h : 12m	12h : 32m	**16h : 14m**
3	Fuzzy+PI Battery type A	*20 µV*	0 sec	0 sec	0 sec	**0 sec**
2	Conventional PI Battery type B	*2000 µV*	0h : 54m	1h : 14m	2h : 0m	**2h : 40m**
4	Fuzzy+PI Battery type B	*20 µV*	0 sec	0 sec	0 sec	**0 sec**

Table 4-4: Comparison of time periods for charging currents to drop below certain values for the tests with the conventional PI vs. Fuzzy+PI controllers

The impact of the auto-setpoint feature is evident from the table, which demonstrates that the Fuzzy+PI controller immediately drops below the specified current values for all criteria, owing to the very low initial error values. In contrast, the experiments conducted with the conventional PI controller show that despite the initial errors being infinitesimal in the range of 2 to 3 mV, it takes several hours for charging currents to decrease below the specified criteria. Table 4-5 presents results of other experimental tests that employed the conventional PI controller to decrease the charging current below certain values.

#	Test Type	Initial Error	Required time for current to once drop below			
			1000 µA	500 µA	100 µA	50 µA
5	Conventional PI controller	*1.4 mV*	0h : 17m	0h : 27m	7h : 30m	27h : 56m
6	Conventional PI controller	*5.5 mV*	0h : 34m	0h : 45m	10h : 35m	65h : 42m
7	Conventional PI controller	*190 mV*	16h : 06m	22h : 48m	52h : 48m	70h : 51m
8	Conventional PI controller	*200 mV*	16h : 26m	23h : 42m	54h : 16m	71h : 39m

Table 4-5: Time periods for charging currents to drop below certain values for some experimental float current analysis tests

4.3   Summary

To provide a summary, the introduction of the new Fuzzy+PI controller resulted in several significant enhancements to the system. These enhancements can be described in three main categories as follows:

I.   The new Fuzzy+PI controller offered a significant improvement to the system through the elimination of the tedious, time-consuming tuning process required for each battery cell type. This feature can save up to several days that would have been spent performing trial-and-error tests.

II.   The new Fuzzy+PI controller provides enhanced performance by reducing fluctuations in charging current values without compromising voltage control. This feature not only saves time but also increases accuracy in acquiring useful data for the float current analysis.

III. The auto-setpoint feature of the new controller has been designed to reduce test durations by allowing the battery cell to pass through the transient phase in a matter of seconds. This feature is optional, as it will only activate if the voltage setpoint is at its default value of zero, and will remain inactive if the operator assigns a specific setpoint.

5. Conclusion and Future Development

In conclusion, this thesis aimed to improve the accuracy and practicality of float current analysis testing tool (i.e., Floater) on lithium-ion battery cells by developing a self-tuning Fuzzy+PI controller. The performance of this new controller was compared to that of the previously used conventional PI controller voltage and charging currents readings in terms of time savings and readings fluctuations. Four experimental tests were conducted, two using the conventional PI controller with manual assigning of setpoints and two using the new Fuzzy+PI controller with the auto-setpoint feature, on two different types of battery cells. The results were compared in terms of standard deviations, needed test durations, and the time required for manual tuning of the conventional PI controller was also discussed.

The comparison of the two controllers revealed that the auto-setpoint feature of the Fuzzy+PI controller had a significant impact on the time required to collect a sufficient stream of data on charging current readings. The Fuzzy+PI controller outperformed the conventional PI controller in regulating charging current for both battery types A and B, improving the standard deviation by 25.18% and 10.83%, respectively. Additionally, the Fuzzy+PI controller showed a similar level of voltage control performance to the conventional PI controller, with a difference of approximately 1% in the standard deviations of the voltage readings and the maximum range of error fluctuations. In other words, the improved regulating charging current was achieved without compromising the voltage control performance, even some improved behavior was detected.

Another notable advantage of the Fuzzy+PI controller is the elimination of the manual effort required to tune the controller gains for each battery cell being tested. The tuning procedure may require several trial-and-errors, which costs a significant amount of time to accomplish. This feature of the new controller reduces the overall testing time, cost, and effort associated with manual tuning. The time savings were on the order of tens of hours for each lithium-ion battery cell type.

In conclusion, the results of this study demonstrate the effectiveness of the newly developed self-tuning Fuzzy+PI controller in achieving more accurate results without

jeopardizing the voltage control performance while reducing the overall testing time and effort. The results also highlight the potential of the Fuzzy+PI controller in reducing fluctuations in the readings. Overall, this study contributes to the development of a more advanced and efficient testing tool for the float current analysis of lithium-ion batteries.

In order to put forth a proposition for future research and development, it is suggested that the Fuzzy+PI controller could benefit from the utilization of artificial intelligence or machine learning techniques. This would aid in enhancing the technical proficiency required to design the fuzzy logic interface by facilitating the development of refined membership functions for both the inputs and outputs, as well as defining more accurate rule sets.

Simulations are also likely to be a valuable tool in achieving this objective. Simulations allow for the testing and validation of different approaches in a controlled environment, which can help to identify potential issues and refine the design of the Fuzzy+PI controller. However, it is worth noting that the use of machine learning methods and advanced battery ageing models can come at a computational cost. Therefore, it is important to carefully consider the trade-offs between computational complexity and performance when designing the Fuzzy+PI controller.

Bibliography

[1]   J. Vetter *et al.*, "Ageing mechanisms in lithium-ion batteries," *J Power Sources*, vol. 147, no. 1–2, pp. 269–281, Sep. 2005, doi: 10.1016/J.JPOWSOUR.2005.01.006.

[2]   M. Theiler, C. Endisch, and M. Lewerenz, "Float Current Analysis for Fast Calendar Aging Assessment of 18650 Li(NiCoAl)O2/Graphite Cells," *Batteries 2021, Vol. 7, Page 22*, vol. 7, no. 2, p. 22, Apr. 2021, doi: 10.3390/BATTERIES7020022.

[3]   A. Maheshwari, "Modelling, Aging and Optimal Operation of Lithium-ion Batteries," Politecnico di Torino, 2018.

[4]   M. Yoshio, R. J. Brodd, and A. Kozawa, "Lithium-ion batteries: Science and technologies," *Lithium-Ion Batteries: Science and Technologies*, pp. 1–452, 2009, doi: 10.1007/978-0-387-34445-4/COVER.

[5]   "Anthroposophie Forum - Bibliothek: Alessandro Volta." https://www.anthroposophie.net/bibliothek/nawi/physik/volta/bib_volta.htm (accessed Apr. 06, 2023).

[6]   "Tempio Voltiano - Wikipedia." https://en.wikipedia.org/wiki/Tempio_Voltiano (accessed Apr. 06, 2023).

[7]   "RWTH AACHEN UNIVERSITY Institute for Power Electronics and Electrical Drives - English." https://www.isea.rwth-aachen.de/go/id/ojnv/?lidx=1 (accessed Apr. 06, 2023).

[8]   M. A. Rosen and A. Farsi, "Battery Technology: From Fundamentals to Thermal Behavior and Management," *Battery Technology: From Fundamentals to Thermal Behavior and Management*, pp. 1–280, Jan. 2023, doi: 10.1016/C2022-0-00504-3.

[9]   J. M. Tarascon and M. Armand, "Issues and challenges facing rechargeable lithium batteries," *Nature 2001 414:6861*, vol. 414, no. 6861, pp. 359–367, Nov. 2001, doi: 10.1038/35104644.

[10]   "US4668595A - Secondary battery - Google Patents." https://patents.google.com/patent/US4668595A/en (accessed Apr. 06, 2023).

[11]   A. Kozawa *et al.*, "Progress in batteries and solar cells. Volume 1 (Book) |
        OSTI.GOV," *United States*, 1990. https://www.osti.gov/biblio/6424836 (accessed
        Apr. 06, 2023).

[12]   D. Wieboldt, M. Hahn, and I. Ruff, "Techniques for Raman Analysis of
        Lithium-Ion Batteries," *Lithium Ion Batteries - New Developments*, vol. 30, no. 6,
        2015,   Accessed: Apr.   06,   2023.   [Online].   Available:
        https://www.spectroscopyonline.com/view/techniques-raman-analysis-
        lithium-ion-batteries

[13]   "Concepts   in   Biochemistry   -   Redox   Reactions."
        https://www.wiley.com/college/boyer/0470003790/reviews/redox/redox.htm
        (accessed Apr. 06, 2023).

[14]   A. Barré, B. Deguilhem, S. Grolleau, M. Gérard, F. Suard, and D. Riu, "A
        review on lithium-ion battery ageing mechanisms and estimations for
        automotive applications," *J Power Sources*, vol. 241, pp. 680–689, Nov. 2013, doi:
        10.1016/J.JPOWSOUR.2013.05.040.

[15]   C. R. Birkl, M. R. Roberts, E. McTurk, P. G. Bruce, and D. A. Howey,
        "Degradation diagnostics for lithium ion cells," *J Power Sources*, vol. 341, pp.
        373–386, Feb. 2017, doi: 10.1016/J.JPOWSOUR.2016.12.011.

[16]   M. Wohlfahrt-Mehrens, C. Vogler, and J. Garche, "Aging mechanisms of
        lithium cathode materials," *J Power Sources*, vol. 127, no. 1–2, pp. 58–64, Mar.
        2004, doi: 10.1016/J.JPOWSOUR.2003.09.034.

[17]   S. Santhanagopalan, G.-H. Kim, M. Keyers, A. A. Pesaran, K. Smith, and J.
        Neubauer, "Design and analysis of large lithium-Ion battery systems," p. 241,
        2015.

[18]   R. Kötz, P. W. Ruch, and D. Cericola, "Aging and failure mode of
        electrochemical double layer capacitors during accelerated constant load tests,"
        J Power Sources, vol. 195, no. 3, pp. 923–928, Feb. 2010, doi:
        10.1016/J.JPOWSOUR.2009.08.045.

[19]   P. Keil *et al.*, "Calendar Aging of Lithium-Ion Batteries," *J Electrochem Soc*, vol.
        163, no. 9, p. A1872, Jul. 2016, doi: 10.1149/2.0411609JES.

[20]   M. R. Palacín, "Understanding ageing in Li-ion batteries: a chemical issue,"
        Chem Soc Rev, vol. 47, no. 13, pp. 4924–4933, Jul. 2018, doi:
        10.1039/C7CS00889A.

[21]   J. Niu, B. E. Conway, and W. G. Pell, "Comparative studies of self-discharge by
        potential decay and float-current measurements at C double-layer capacitor

and battery electrodes," *J Power Sources*, vol. 135, no. 1–2, pp. 332–343, Sep. 2004, doi: 10.1016/J.JPOWSOUR.2004.03.068.

[22] M. Lewerenz *et al.*, "New method evaluating currents keeping the voltage constant for fast and highly resolved measurement of Arrhenius relation and capacity fade," *J Power Sources*, vol. 353, pp. 144–151, Jun. 2017, doi: 10.1016/J.JPOWSOUR.2017.03.136.

[23] S. Nagaya *et al.*, "The state of the art of the development of SMES for bridging instantaneous voltage dips in Japan," *Cryogenics (Guildf)*, vol. 52, no. 12, pp. 708–712, Dec. 2012, doi: 10.1016/J.CRYOGENICS.2012.04.014.

[24] M. A. Johnson *et al.*, "PID control: New identification and design methods," *PID Control: New Identification and Design Methods*, pp. 1–543, 2005, doi: 10.1007/1-84628-148-2/COVER.

[25] K. J. Åström and T. Hägglund, "Advanced PID Control," *ISA - The Instrumentation, Systems, and Automation Society*, 2006. https://www.isa.org/products/advanced-pid-control (accessed Apr. 06, 2023).

[26] K. H. Ang, G. Chong, and Y. Li, "PID control system analysis, design, and technology," *IEEE Transactions on Control Systems Technology*, vol. 13, no. 4, pp. 559–576, Jul. 2005, doi: 10.1109/TCST.2005.847331.

[27] D. S. Hooda and R. Vivek, "Fuzzy Logic Models and Fuzzy Control: An Introduction," *Alpha Science International Ltd.*, 2017. https://www.researchgate.net/publication/362325701_Fuzzy_Logic_Models_and_Fuzzy_Control_An_Introduction (accessed Apr. 06, 2023).

[28] T. J. Ross, *Fuzzy Logic with Engineering Applications: Third Edition*. John Wiley and Sons, 2010. doi: 10.1002/9781119994374.

[29] L. A. Zadeh, "Fuzzy sets," *Information and Control*, vol. 8, no. 3, pp. 338–353, Jun. 1965, doi: 10.1016/S0019-9958(65)90241-X.

[30] "Fuzzy Logic - CodeCrucks." https://codecrucks.com/what-is-crisp-set/ (accessed Apr. 06, 2023).

[31] M. Jevšček, "Competencies assessment using fuzzy logic," vol. 5, no. 2, pp. 187–202, 2016.

[32] R. Jager, "Fuzzy Logic in Control." 1995. Accessed: Apr. 06, 2023. [Online]. Available: http://resolver.tudelft.nl/uuid:418ca337-3518-4a0c-ba87-6117d114cf94

[33] L. A. Bryann and E. A. Bryann, "Programmable Controllers Theory and Implementation Second Edition," 1988, Accessed: Apr. 06, 2023. [Online]. Available: www.industrialtext.com

[34] B. Ferdi, C. Benachaiba, S. Dib, and R. Dehini, "Adaptive PI Control of Dynamic Voltage Restorer Using Fuzzy Logic," 2010. [Online]. Available: www.hypersciences.org

[35] " 8-bit AVR Microcontrollers ATmega324P/V - Datasheet Summary." http://ww1.microchip.com/downloads/en/devicedoc/atmel-42743-atmega324p_summary.pdf

[36] "ATmega versus STM32: Which Microcontroller is Best for Your Application." https://predictabledesigns.com/atmega-versus-stm32-which-microcontroller-is-best-for-your-application/ (accessed Apr. 06, 2023).

[37] "What Is RISC (Reduced Instruction Set Computer)? | Definition from TechTarget." https://www.techtarget.com/whatis/definition/RISC-reduced-instruction-set-computer (accessed Apr. 06, 2023).

List of Figures

List of Tables